Nanoscale Structural Characterization of Oxide and Semiconductor Heterostructures

By

Joonkyu Park

A dissertation submitted in partial fulfillment of

the requirements for the degree of

Doctor of Philosophy

(Materials Science)

at the

UNIVERSITY OF WISCONSIN-MADISON

2018

Date of final oral examination: 09/20/2018

The dissertation is approved by the following members of the Final Oral Committee:

Paul Evans, Professor, Materials Science and Engineering

Chang-Beom Eom, Professor, Materials Science and Engineering

Mark Eriksson, Professor, Physics

Jason Kawasaki, Assistant Professor, Materials Science and Engineering

Jiamian Hu, Assistant Professor, Materials Science and Engineering

Abstract

According to a recent report from International Technology Roadmap for Semiconductors (ITRS), semiconductor industry based on silicon Complementary metal–oxide–semiconductor (CMOS) technology is facing challenges in terms of making the device faster with higher density and lower power consumption. To overcome the challenges, various methodologies are attempted using different state variables instead of electric charges, for example, polarization, phase states, and electron spin information. Different materials can also be chosen instead of silicon, for example, carbon, complex metal oxides in 1D or 2D nanostructure formations. A different concept of operating devices is also another option, for example, single electron transistors, spintronics, and quantum electronics.

A tremendous number of stages during microfabrication manufacturing for integrated circuits consist of a series of deposition and etching processes. During these processes, unknown problems can arise from the design of their structural geometry. For example, unwanted strain distribution from the electrode patterns can change the electric properties of underlying materials regarding the decrease in charge carrier mobility or increase in leakage current in dielectrics, which all occur in nanoscale. So, it is important to understand the effects of structural phenomena on the electronic properties of materials using nanoscale characterization.

The first work shows the changes in electronic property in Si quantum dot devices fabricated on Si/SiGe heterostructure is discussed. The electrode deposition process on the heterostructure surface is necessary for the device operation, but the electrodes also induce external nanoscale strain fields. These strain fields are transferred to the substrate materials via electrode edges and change electronic band structure. The magnitudes of the strain and their impact on changing the band structure are studied. In the second project, the alignment of ferroelectric

polarization nanodomains in PbTiO$_3$/SrTiO$_3$ (PTO/STO) superlattice heterostructures is discussed. The PTO/STO nanostructure was created using a focused-ion beam technique. The domain alignment was observed using the x-ray nanodiffraction. A thermodynamic theoretical approach calculates the free energy density of the system to understand the origin of domain alignment. In the final project, the origin of photoinduced domain transformation in PTO/STO superlattices is discussed. Charged carriers are excited by the above-bandgap optical illumination, and transported by the internal electric fields arising from depolarization fields. These photoexcited charge carriers eventually screen the depolarization fields, and the initial striped nanodomain patterns transform to a uniform polarization state. After the end of illumination, the striped nanodomains patterns recover for a period of seconds at room temperature. The transformation time depends on the optical intensity, and the recovery time depends on the temperature. A charge trapping model with a theoretical calculation reveals that the charge trapping is a dominant process for the domain transformation, and the de-trapping process is for the recovery. Simulated domain intensity changes are in good agreements with the X-ray diffraction data.

Acknowledgments

I would like to thank my advisor Paul Evans for guiding me to be a good scientist/engineer. It was lucky that I met him since I could learn an appropriate mindset to find solutions for scientific questions and challenges. It was also very thankful that he encouraged me to choose the better paths when I had a difficult time.

I enriched my research over the past years with all the group members. Firstly, thanks to Qingteng Zhang who inspired me with research topics. From him, I learned a lot about the synchrotron- and research-related physics through many meaningful discussions and brainstorming. Also, thanks to Kyle McElhinny, Jack Tilka, and Pice Chen who had led the group in all aspects from the basic lab management to the experimental guide even before I joined the group. Their existence was necessary for me to successfully overcome the challenges I had faced during my first few years of the journey. I would also like to thank other group members, Youngjun Ahn, Yajin Chen, Samuel Marks, Arunee Lakkham, Anatasios Pateras, and Hyeonjun Lee whom I spent most of my time with.

I would like to thank other collaborators, Mohammed Humed Yusuf and Matthew Dawber who provided me the scientific insights along with the great samples. Thanks to John Mangeri and Serge Nakhmanson for many discussions about the theoretical approaches to solve the problems. Also, thanks to Haidan Wen, Yi Zhu, and Martin Holt who helped me carry out the experiments in station 7 ID-C and 26 ID at the Advanced Photon Source at the Argonne National Laboratory.

Lastly, I would like to thank my parents and brother for supporting me until now. Also, thanks to my wife, Yumi Ko who waited for a long time encouraging me in many ways. Furthermore, for the next round of life, I hope I can be a good father to my daughter, Yena Park.

Table of Contents

List of Figures

Figure 1-1: X-ray nanodiffraction geometry of an Si/SiGe heterostructure, on which a Pd electrode has been deposited. The 10 keV X-ray beam is focused using Fresnel zone plate focusing optics and a 2 dimensional CCD detector is used to detect the diffracted x-ray intensity. The Bragg reflection can shift on the detector resulting from electrode-stress-induced lattice tilt along the *Tilt* and *Δ2θ* directions.

Figure 1-2: (a) Schematic of the x-ray diffraction geometry for studies of Si/SiGe heterostructures showing both cases of with (dotted) and without (solid) lattice tilt. k_i and k' are the wavevectors of the incident and diffracted X-rays at Bragg angle $θ$. Q is the corresponding reciprocal space vector without lattice tilt. When the lattice plane is tilted with tilt angle $χ$, diffracted X-ray beam is shifted by an angle $α$, and the corresponding wavevectors become $k'(χ)$ and $Q(χ)$. (b) Schematic showing diffracted X-rays both with and without lattice tilt. Three additional vectors a, b and c are defined to estimate the shift of diffracted X-ray using the trigonometrical function.

Figure 2-1: SEM image of a Si QD device showing the regions of interest in which x-ray nanodiffraction was used to probe the structural distortion. The regions of interest for the x-ray nanodiffraction are outlined with the two boxes. The dashed box indicates a region where a single linear gate electrode is deposited, and the solid box shows where many gate electrodes are closely deposited to make the electrostatically defined QD region.

Figure 2-2: Cross section of the Si/SiGe heterostructure and Pd gate electrode. The SQW is deformed with electrode-stress-induced radius of curvature R due the transferred stress from the electrode. The strain difference between bottom and top layer of SQW is defined as t/R.

Figure 2-3: Simulated $θ$-$2θ$ coupled scan of the sSQW and the top SiGe. The position of the Bragg peaks from the top SiGe and the sSQW along q_z are at 4.58 Å^{-1} and 4.69 Å^{-1}, respectively. Narrow and broad oscillating fringe components are from the thicknesses of the top SiGe and sSQW layers, which are 91 nm and 10 nm, respectively.

Figure 2-4: Map of the Pd M-edge fluorescence intensity in the quantum device region using x-ray nanobeam fluorescence microscopy. The fluorescence intensity becomes bright when the x-ray nanobeam illuminates the middle of each electrode, showing that nine Pd gate electrodes are deposited.

Figure 2-5: (a) Detector image of a diffraction pattern of the sSQW. Because the detector can capture two-dimensional reciprocal space information, the thickness fringe along the *Δ2θ*-direction is also visible. The thickness fringe arising from the 91-nm thick SiGe layer is superimposed on the sSQW Bragg peak, and the shadow of the center stop is also visible in the middle of the diffraction pattern. (b) Stack of the *Tilt*-direction intensity line profiles. The x-ray nanobeam was laterally displaced across the electrode at fifty locations. The diffraction patterns are summed along *Δ2θ*-direction to calculate the centroid along the Tilt direction. The summed diffraction patterns are stacked up on each other. The green curve exhibits change in centroid.

Figure 2-6: Comparison between experimental diffraction pattern and simulation, and between the diffraction patterns acquired (a) far from the electrode and (c) at the tilted region. (b) Simulated diffraction pattern using the method of Ref [26] and conditions corresponding to (a).

Figure 2-7: (a) Intensity line profiles of diffraction patterns integrated along the *Tilt*-direction of the detector, acquired in regions far from the tilted region (blue) and at the tilted region (orange). (b) Fourier transform intensities of the two intensity line profiles and the models shown in (a) as a function of spatial frequency, Δq_z. The Fourier transform intensity at $\Delta q_z = 0.007$ arises from the thickness fringe of the top SiGe layer, and the results of the Fourier transform of the model agree, as shown in the dotted curves.

Figure 2-8: Map of the Pd M-edge fluorescence intensity in the region of a single linear Pd electrode using x-ray nanobeam microscopy. The intensity becomes bright when the x-ray beam illuminates the middle of the electrode. (b) Fourier transform intensity at a fringe spacing of $\Delta q_z = 0.007$ Å-1, exhibiting the disappearance of the SiGe layer interference fringes in the tilted region.

Figure 2-9: Fourier transform intensity at fringe spacing of $\Delta q_z = 0.007$ Å^{-1} for the areas shown in Figure 2 4. The black box indicates the QD region where many electrodes are closely deposited, and the Fourier transform intensity of this region is shown in (b).

Figure 2-3: Stack of the Tilt-direction intensity line profiles for the comparison between two methods to track the shift of the diffraction pattern. The centroid information (green) already introduced in Figure 2- (b) is compared with the phase information (blue) extracted from the Fourier transform of the diffraction patterns.

Figure 2-4: Si/SiGe heterostructure showing lattice displacements along the x-axis (u), which is a function of the two radial distances r_1 and r_2 measured in the *x-z* plane.

Figure 2-5: 3D map of lattice tilt angles calculated from the first derivative of u in terms of the depth z. The magnitude of lattice tilts under electrode is depth dependent, and it becomes 0.03° approximately 100 nm below the surface at which sSQW is located (outlined with a black box).

Figure 2-6: (a) Cross-sectional diagram of X-ray diffraction geometry explaining an issue regarding offset of electrode positions between Figures. 2-8 (a) and 2-8 (b). The red dot is a particular surface location at which the incident x-ray k_i, illuminates sSQW buried immediately beneath the electrode. k_i', is another incident x-ray at which fluorescence signal from electrode is initially generated. (b) Plan view of experimental X-ray diffraction geometry. The direction of incident X-ray and the electrode direction different by an angle δ provides $\Delta x = 108$ nm when considering the approximate value of the angle δ of 45°.

Figure 2-7: Illustration of a Cartesian coordinate *Tilt-Δ2θ* plane. *P(Tilt, Δ2θ)* is a position of diffraction pattern on detector. *P(α⊥, α∥)* is a new position on α⊥-α∥ plane converted by a rotation matrix. The α⊥ and α∥ are directions perpendicular and parallel to electrode length direction, respectively. The shift in the diffraction pattern on the detector is determined by computing the shift of centroid of the diffraction patterns on the *Tilt-Δ2θ* plane and then reconsidered on the α⊥-α∥ plane by the rotation matrix.

Figure 2-8: Map of the sSQW lattice tilt angles in a single electrode area indicated by the dotted box in Figure 2 1. Lattice tilt angles are measured by computing shifts in diffraction patterns from sSQW, for which the maximum magnitude becomes 0.03° under the electrode. The sign of lattice tilt changes at the middle of the electrode, which might arise from lattice deformations by elastically transferred electrode stress.

three panels and last panel was obtained at room temperature and 400 K. Optical intensities were 46 mW cm^{-2}, 58 mW cm^{-2}, and 145 mW cm^{-2}. The shaded region represents 25 s of optical illumination.

List of Equations

Chapter 1: Introduction

1.1 Heterostructures

Semiconductor heterostructure, a sandwiched-multilayer of different semiconductors, can improve the device performance through bandgap engineering [1] and strain engineering [2]. In the same context, the formation of 2-dimensional electron gases (2DEGs) [3], ferroelectric superlattices, [4] and stacking 2D material layers in so-called van der Waals heterostructures [5,6] have also become exciting research topics in terms of the discovery and investigation of new physical phenomena. For example, the advent of these heterostructures opens a new era in which the quantum computer is anticipated as the fundamental building block of future devices for the faster computing speeds in key problems.

H. Kroemer and Z. Alferov proposed the concept of a double heterostructure in the early 1960s and were awarded the Nobel prize in Physics in 2000 for their contributions to double-heterostructure-based devices [7]. One of the most significant developments to fabricate the high crystalline heterostructure is the evolution of epitaxial growth techniques such as molecular beam epitaxy (MBE) and metal organic chemical vapor deposition (MOCVD) developed in the 1970s, and MBE was mainly designed to fabricate III-V semiconductor heterostructures in 1975 by A. Cho at Bell Laboratory [8,9]. The realization of low dimensional semiconductor devices using the concept of the heterostructure has also been a relevant research field for quantum electronics, in which their electronic properties are significantly different from the same bulk material [10]. Notably, quantum wells (QWs) restrict the motion of charge carriers within limited dimensions. This confinement effect was demonstrated in optical absorption spectra in the 1970s [10,11]. QWs have been widely used as fundamental building blocks of the quantum electronics, and can require

the patterning of surface structures such as thin metal electrode patterns for their operation. These surface structures, however, can unintentionally alter the electronic properties of the QWs by inducing additional stresses. A more detailed description and experimental study of this effect is provided in Chapter 2.

1.2 Superlattices

Further progress of in the design and fabrication of heterostructures started with experiments on electron transport in superlattices by L. Esaki and R. Tsu [4]. Superlattices have structural periodicity created by the repetition of layers of the same composition of materials. The superlattice period is larger than the lattice constant of the crystal (e.g. tens to hundreds of lattice constants) and leads to an additional periodic potential. The early idea of superlattices is based on the epitaxial growth of the lattice-matched semiconductor materials.

The idea of a superlattice system was not limited to the III-V semiconductor heterostructures and has recently been employed in ferroelectric systems. Ferroelectric superlattices consisting of several unit cells of ferroelectric and dielectric alternating layers also exhibit distinct electronic properties arising from their periodicities [12]. For example, the $PbTiO_3$/$SrTiO_3$ (PTO/STO) superlattice permit exotic ferroelectric polarization domain configurations [13,14]. Superlattices have been studied using many theoretical [15,16] and experimental [14,17] approaches to reveal their new electronic properties. New approaches to understanding and controlling the properties of ferroelectric superlattices based on creating superlattice nanostructures and illuminating the superlattices using above-bandgap light are discussed in Chapters 3 and 5.

1.3   Other engineering techniques

In addition to creating heterostructures, there are many other ways to engineer the electronic properties. For example, in GaAs strain can raise the valence band, change the bandgap, and create more favorable operating conditions for light-emitting diodes [2]. Superlattice growth with lattice-mismatched semiconductor materials inducing strains was demonstrated by E. Blakeslee and J. Matthews. A strained-layer superlattice can be grown with a very low defect concentration because the lattice mismatch between very thin layers is accommodated entirely by strain when the mismatch is less than about 7% [18]. In this case, the misfit defects are rarely generated at the interfaces.

As briefly mentioned above the electronic properties of these thin film heterostructure can be changed by depositing surface structures such as electrodes or by external stimuli such as electric fields or optical illumination. These strategies have a variety of effects on the electronic properties, some of which are only beginning to be understood. The bandgap of Si QWs, for example, is sensitive to atomic arrangement, which is in turn altered by nanoscale strain from the electrode patterns on the surfaces [19], as described in Chapter 2. Randomly organized ferroelectric polarization domains in PTO/STO superlattices are aligned due to subtle nanoscale elastic effects when forming nanostructures [20], as described in Chapter 3. In the same superlattice system, carrier dynamics, after the above-bandgap optical illumination induce domain transformations, as discussed in Chapter 5.

These changes in electronic properties occur at the nanoscale, which makes it difficult to measure them and to interpret their impact. Consequently, nanoscale characterization is necessary. X-ray diffraction is a powerful non-destructive technique for the study of nanoscale structural changes, and provides insight that can be used to deduce electronic information. This technique

recently has become a more powerful tool through the development of x-ray nanofocusing techniques [21]. X-ray nanodiffraction provides a way for scientists and engineers to understand nanoscale materials characteristics.

1.4 X-ray nanodiffraction

The x-ray diffraction techniques discussed in the remaining chapters of this thesis are based on focusing an X-ray beam to a sizes tens to hundreds of nanometers using Fresnel zone plate optics [21]. A zone plate is a pattern of concentric rings consisting of a material whose refractive index is slightly less than unity for X-rays. Thus, the phase velocity of the x-rays in these rings is faster than outside, and after passing through the zone plate, the X-ray beams are focused at one focal point determined by the width and the spacing of the rings.

The x-ray nanodiffraction studies were conducted using the photon energies from 9 to 11 keV facilities at the Advanced Photon Source (APS) of Argonne National Laboratory. Figure 1-1 shows the x-ray nanodiffraction geometry at the Hard X-ray Nanoprobe beamline of the APS, which is mainly discussed in the characterization of Si/SiGe heterostructures described in Chapter 2. A similar approach was employed for the studies described in the other chapters. In the experiments at this beamline, x-ray diffraction patterns were acquired using a two-dimensional charge-coupled-device (CCD) detector. The detector consisted of a 1024 × 1024 array of square pixels with an edge length of 13 µm. Two orthogonal directions on the detector are defined, termed *Tilt* and *Δ2θ*, with orientations as shown in Figure 1-1.
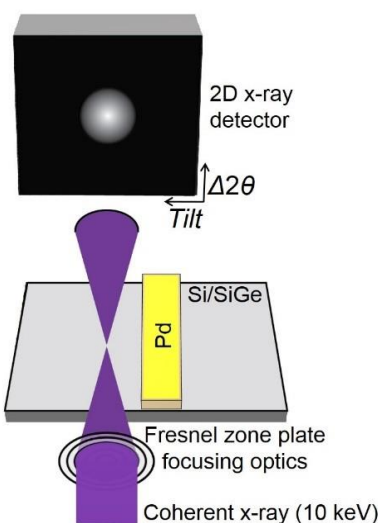
Figure 1-1: X-ray nanodiffraction geometry of an Si/SiGe heterostructure, on which a Pd electrode has been deposited. The 10 keV X-ray beam is focused using Fresnel zone plate focusing optics and a 2 dimensional CCD detector is used to detect the diffracted x-ray intensity. The Bragg reflection can shift on the detector resulting from electrode-stress-induced lattice tilt along the Tilt and Δ2θ directions.

A key issue discussed in Chapter 2 is the tilt of lattice planes resulting from strain effects, which is probed by the X-ray nanodiffraction. Because of these lattice tilts, the diffraction patterns on the detector plane shift according to the tilt directions, and thus, the shift of the diffraction pattern is easily converted to the lattice tilt angle using the relationship between them [22,23]. Figure 1-2(a) shows a diagram of the x-ray diffraction geometry showing wavevectors and angles associated with lattice tilts. The gray rectangular box indicates the orientation of the lattice planes, with the effect of tilts indicated by the dotted rectangular box. Incident and diffracted x-rays are depicted in purple and reciprocal space wavevectors are in red. The solid and dotted lines describe the untitled and tilted lattice planes, respectively. When an incident x-ray beam with wavevector k_i, propagating on the x-z plane, meets the Bragg condition of the lattice at angle θ, the x-ray is diffracted to wavevector k'. The corresponding reciprocal space vector Q is defined to be along the z-axis. When the lattice plane tilts with respect to the x-axis as the axis of rotation with a tilt angle, the diffracted X-ray also deviates from the x-z plane (k''). Accordingly, the reciprocal space
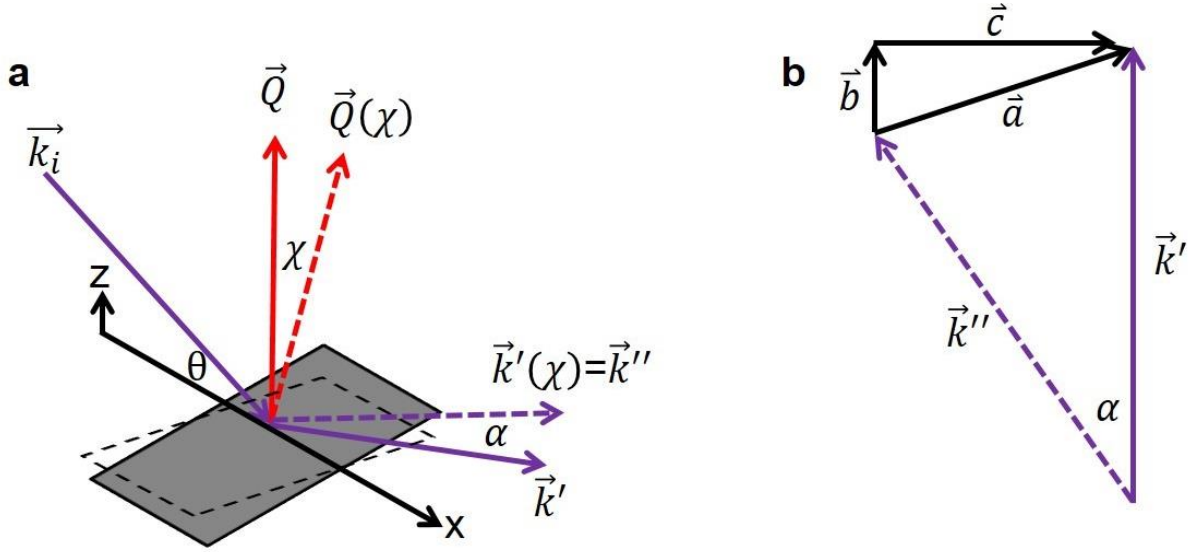
Figure 1-2: (a) Schematic of the x-ray diffraction geometry for studies of Si/SiGe heterostructures showing both cases of with (dotted) and without (solid) lattice tilt. k_i and k' are the wavevectors of the incident and diffracted X-rays at Bragg angle θ. Q is the corresponding reciprocal space vector without lattice tilt. When the lattice plane is tilted with tilt angle χ, diffracted X-ray beam is shifted by an angle α, and the corresponding wavevectors become $k'(\chi)$ and $Q(\chi)$. (b) Schematic showing diffracted X-rays both with and without lattice tilt. Three additional vectors a, b and c are defined to estimate the shift of diffracted X-ray using the trigonometrical function.

vector also depends on the tilt angle. Figure 1-2(b) shows a diagram of the relationship between

the diffracted x-rays from the tilted and untitled planes. The angle of the shift is equal to α, which

is equivalent to the shift of the diffraction pattern on the detector when it is small.

The vector components depicted in Figure 1-2(a) are defined in Eq. 1-1 in terms of three

angles: the incident Bragg angle (θ), shift of the diffraction pattern (α), and lattice tilt angle (χ).

$$\vec{k_i} = |k|cos\theta\hat{x} - |k|sin\theta\hat{z}$$

$$\vec{Q}(\chi = 0) = 2|k|sin\theta\hat{z}$$

$$\vec{Q}(\chi) = |Q|sin\chi\hat{y} + |Q|cos\chi\hat{z}$$

$$\vec{k}'(\chi = 0) = |k|cos\theta\hat{x} + |k|sin\theta\hat{z}$$

$$\vec{k}'(\chi) = \vec{k}'' = |k|\cos\theta\hat{x} + |Q|\sin\chi\hat{y} + (|Q|\cos\chi - |k|\sin\theta)\hat{z}$$

Equation 1-1

The shift of the diffraction patterns α is the angle between the wavevectors k' and k'', which can be calculated as defined in Eq. 1-2.

$$\alpha = \cos^{-1}\left(\frac{\vec{k}' \cdot \vec{k}''}{|\vec{k}'||\vec{k}''|}\right)$$

Equation 1-2

In the X-ray diffraction experiment, α is a measured value, and χ is determined from α. In Figure 1-2(b), three more vectors, *a*, *b* and *c* are defined. Here, *c* is the shift of diffraction patterns on the detector in the experiment. The vector *c* is approximately equal to *a* because *b* and α are small. Based on their definitions in Figure 1-2(b) we can find a relationship between these vectors:

$$\vec{a} = \vec{b} + \vec{c} = \vec{c} = \vec{k}' - \vec{k}'' = (2|k|\sin\theta - |Q|\cos\chi)\hat{z} - |Q|\sin\chi\hat{y}$$

Equation 1-3

When α is small, it can be simplified, as shown in Eq. 1-4 since $|a|=\alpha|k'|$. The direction of vector *a* is the same as the vector *c*, and $|a|=\sqrt{b^2 + c^2}$. Then, α is simply defined as a function of χ.

$$\alpha = \frac{|\vec{a}|}{|\vec{k}'|} = \frac{\sqrt{\vec{c}^2}}{|\vec{k}'|} = \frac{\sqrt{Q^2 sin^2\chi + 4K^2 sin^2\theta - 4KQsin\theta cos\chi + Q^2 cos^2\chi}}{|\vec{k}'|}$$

$$= \frac{\sqrt{8K^2 sin^2\theta(1-cos\chi)}}{|\vec{k}'|} = 2\sqrt{2}Ksin\theta \frac{\sqrt{(1-1+\frac{\chi^2}{2})}}{|\vec{k}'|} = 2sin\theta\chi$$

$$= \frac{Q}{K}\chi$$

Equation 1-4

Therefore, the lattice tilt angle χ is proportional to α simply multiplied by the quantity *K/Q*, which is equal to $1/(2sin\theta)$.

$$\chi = \frac{K}{Q}\alpha = \frac{\alpha}{2sin\theta}$$

Equation 1-5

1.5   Outline of thesis

This thesis describes extensive nanoscale characterization of materials with a focus on their nanoscale structure. The structure in turn influences properties such as the electronic band structure, the distribution of the ferroelectric polarization distribution, and charge carrier dynamics. The structural changes probed here are the result of fabrication processes involved in electrode deposition on Si/SiGe heterostructures, and nanoscale focused-ion-beam milling of the ferroelectric/dielectric superlattice heterostructures to fabricate the ferroelectric nanostructures. Other external stimuli consist of above-bandgap optical illumination, which generates photoexcited charge carriers.

Chapter 2 reports the discovery that the electrode deposition process in the formation of Si quantum dot devices on a Si/SiGe heterostructure results in the deformation of the quantum dots. Quantum devices employing this platform are based on the creation of the 2DEG layer at an interface between Si and SiGe. To operate the device, it is crucial to apply the electric fields vertically to the 2DEG layer to electrostatically define the depletion regions to form the nanoscale 1D area that stores electrons. Electrode deposition on the Si/SiGe heterostructure is therefore essential to realize the quantum devices because its operation is also carried out using these electrode structures on top of the heterostructures.

During film deposition, a complex microstructure growth mechanism accounts for stress generation and relaxation. During the deposition, metal adsorbates on semiconductors follows the Volmer-Weber mechanism [24], and there are three different stages that generates stresses. Initial compressive stress arises from island capillary force due to the surface stress while the sizes of islands are small [25,26]. Intermediate tensile stress originates from grain boundaries. When the grains of these islands grow and contact on another, they immediately form grain boundaries by rapidly filling in adjacent surfaces. A final mechanism is that atoms arriving on the surface on the surface during deposition are driven to grain boundaries, leading to compressive stress [26].

The stress from the electrodes is transferred through the underlying materials via electrode edges resulting in strain fields along the thickness, which changes the electronic band structure. X-ray nanodiffraction data shows that the 10-nm-thick Si QW layer is deformed in which the top and bottom interfaces of the QW experience different magnitudes of strain. This strain difference can be calculated from the shift of diffraction patterns on the detector plane. The strain calculated from the diffraction study is used to extract the extent of the change in band structure using deformation potential energy.

Chapter 3 reports the alignment of ferroelectric polarization nanodomains in PTO/STO superlattice heterostructures. PTO/STO superlattice thin films form 180° polarizations domains in which the polarizations are energetically stable with the formation of nanometer-size domains in random orientation. X-ray nanodiffraction reveals that these domains are aligned along the mechanical boundaries of elongated nanostructures fabricated using focused-ion-beam (FIB) lithography. More specifically, the domain diffuse scattering intensity in reciprocal space appears only at locations in reciprocal space corresponding to the directions of aligned domain patterns. In the unpatterned area, with its random domain distribution, the intensity forms a uniform ring. To understand the origin of the domain alignment, a thermodynamic theoretical approach is applied to calculate the free energy of the system.

Finally, Chapter 5 describes a study of the temperature dependence of the relaxation of optical effects on the domain pattern. X-ray nanodiffraction shows that the intensity of the domain diffuse scattering disappears while the superlattice is optically illuminated and slowly recovers over a period of seconds to hundreds of seconds. The analysis of the experimental results links the relaxation to charge-carrier dynamics in PTO/STO superlattices. In this model, charge carriers are excited by the above-bandgap optical laser and transported by the internal electric fields arising from depolarization fields. This charge carriers screen the depolarization fields, which reduces the electrostatic energy of the system. Thus, the ferroelectric polarization nanodomains in the superlattice transform to a uniform polarization state [27]. Measurements of the rate of the recovery of the domain pattern following the end of the illumination provide a key test of the trapping model.

1.6 References

[1]   F. Capasso and A. Y. Cho, Surf. Sci. **299**, 878 (1994).

[2]   E. Yablonovitch and E. O. Kane, J. Light. Technol. **4**, 504 (1986).

[3]   Y. Katayama, M. Morioka, Y. Sawada, K. Ueyanagi, T. Mishima, Y. Ono, T. Usagawa, and Y. Shiraki, Jpn. J. Appl. Phys **23**, L150 (1984).

[4]   L. Esaki and R. Tsu, IBM J. Res. Dev. **14**, 61 (1970).

[5]   M. Y. Li, C. H. Chen, Y. M. Shi, and L. J. Li, Mater. Today **19**, 322 (2016).

[6]   K. S. Novoselov, A. Mishchenko, A. Carvalho, and A. H. C. Neto, Science **353**, 7, aac9439 (2016).

[7]   Z. I. Alferov, Rev. Mod. Phys. **73**, 767 (2001).

[8]   A. Y. Cho and J. R. Arthur, Prog. Solid State Chem. **10**, 157 (1975).

[9]   A. Y. Cho, J. Vac. Sci. Technol. **8**, S31 (1971).

[10]   R. Dingle, W. Wiegmann, and C. H. Henry, Phys. Rev. Lett. **33**, 827 (1974).

[11]   L. L. Chang, L. Esaki, and R. Tsu, Appl. Phys. Lett. **24**, 593 (1974).

[12]   H. N. Lee, H. M. Christen, M. F. Chisholm, C. M. Rouleau, and D. H. Lowndes, Nature **433**, 395 (2005).

[13]   A. K. Yadav, C. T. Nelson, S. L. Hsu, Z. Hong, J. D. Clarkson, C. M. Schlepütz, A. R. Damodaran, P. Shafer, E. Arenholz, L. R. Dedon, D. Chen, A. Vishwanath, A. M. Minor, L. Q. Chen, J. F. Scott, L. W. Martin and R. Ramesh, Nature **530**, 198 (2016).

[14]   P. Zubko, N. Jecklin, A. Torres-Pardo, P. Aguado-Puente, A. Gloter, C. Lichtensteiger, J. Junquera, O. Stephan, and J. M. Triscone, Nano Lett. **12**, 2846 (2012).

[15]   P. Aguado-Puente and J. Junquera, Phys. Rev. B **85**, 184105 (2012).

[16]   M. B. Okatan, I. B. Misirlioglu, and S. P. Alpay, Phys. Rev. B **82**, 094115 (2010).

[17]   M. Dawber, N. Stucki, C. Lichtensteiger, S. Gariglio, P. Ghosez, and J. M. Triscone, Adv. Mater. **19**, 4153 (2007).

[18]   G. C. Osbourn, IEEE J. Quantum Electron. **22**, 1677 (1986).

[19]   J. Park, Y. Ahn, J. A. Tilka, K. C. Sampson, D. E. Savage, J. R. Prance, C. B. Simmons, M. G. Lagally, S. N. Coppersmith, M. A. Eriksson, M. V. Holt, and P. G. Evans, APL Mater. **4**, 066102 (2016).

[20]   J. Park, J. Mangeri, Q. Zhang, M. H. Yusuf, A. Pateras, M. Dawber, M. V. Holt, O. G. Heinonen, S. Nakhmanson and P. G. Evans, Nanoscale **10**, 3262 (2018).

[21]   E. Di Fabrizio, F. Romanato, M. Gentili, S. Cabrini, B. Kaulich, J. Susini, and R. Barrett, Nature **401**, 895 (1999).

[22]   P. G. Evans, P. P. Rugheimer, M. G. Lagally, C. H. Lee, A. Lal, Y. Xiao, B. Lai, and Z. Cai, J. Appl. Phys. **97**, 103501 (2005).

[23]   P. G. Evans, D. E. Savage, J. R. Prance, C. B. Simmons, M. G. Lagally, S. N. Coppersmith, M. A. Eriksson, and T. U. Schulli, Adv. Mater. **24**, 5217 (2012).

[24]   I. Markov, *Crystal Growth for Beginners: Fundamentals of Nucleation, Crystal Growth, and Epitaxy* (World Scientific, Singapore, 1995).

[25]   J. A. Floro, S. J. Hearne, J. A. Hunter, P. Kotula, E. Chason, S. C. Seel, and C. V. Thompson, J. Appl. Phys. **89**, 4886 (2001).

[26]   E. Chason, B. W. Sheldon, L. B. Freund, J. A. Floro, and S. J. Hearne, Phys. Rev. Lett. **88**, 156103 (2002).

[27]   Y. Ahn, J. Park, A. Pateras, M. B. Rich, Q. Zhang, P. Chen, M. H. Yusuf, H. Wen, M. Dawber, and P. G. Evans, Phys. Rev. Lett. **119**, 057601 (2017).

Chapter 2: Nanoscale strain in Si quantum wells

2.1 Introduction

Silicon is a promising material for quantum electronics because its electronic properties include favorable band alignment at heterostructure interfaces and weak spin-orbit coupling resulting in long electron spin coherence times. Si QWs formed in Si/SiGe heterostructures confine electrons. Furthermore, quantum dot (QD) structures can be electrostatically defined by top gate electrodes that are used to apply electric fields. Residual stress in the electrodes can arise due to complex microstructure growth mechanisms such as island coalescence and can be elastically transferred to the substrate. This chapter reports the discovery of that this residual stress deforms the Si QWs and perturb the electronic energy landscape. The structural study was conducted using a tightly focused X-ray nanobeam, which allowed the curvature of the Si QW to be measured and its strain to be calculated from the curvature.

2.1.1 Si quantum devices

Si is the host semiconductor material for quantum devices confining electrons within the artificially and electrostatically defined quantum structures such as QWs and QDs. The fabrication processes for these quantum structures are well developed. The electronic states in Si can be manipulated using elastic strain or electric fields [1-4]. For example, the QD structures are often electrostatically defined within strained-Si quantum wells (sSQWs) formed in Si/SiGe heterostructures. Gate electrodes are used to manipulate the population of electrons within the QDs, and to perform complex operations such as determining the quantum state of electrons [5]. Determining the values of the gate voltages while operating devices is an essential step yet complicated when the electronic potential-energy landscape is disordered. One potential source of

electronic potential disorder is the electric potential from fixed charges, for example from surface oxide layers [6].

In addition to the previously considered sources of disorder in QW, there are additional effects associated with the formation and patterning of the electrodes. Residual stress in the metal gate electrodes is elastically transferred to the sSQW. As discussed in this chapter, the detailed spatial distribution of the distortion is consistent with an elastic model. The strain within the QW can be determined from the structural measurements by computing the curvature of the quantum well and the strain that results from the curvature. The results show that the strain difference between the top and bottom layers of the sSQW is high enough to cause energy landscape disorders and thus difficulties in tuning gate voltages.

X-ray nanodiffraction was used to probe the magnitude of lattice deformation. Nanodiffraction is a non-destructive method to study structures that does not introduce any additional distortion during sample preparation. Nanodiffraction studies of the QWs are particularly sensitive to lattice tilt.

As shown Figure 2-1, the electrodes are deposited in a closely spaced pattern on Si/SiGe heterostructures, and their end points converge to electrostatically define QDs. Detailed studies of lattice tilt were conducted within the two regions of interest in the QD device that are indicated by the dashed and solid boxes in Figure 2-1. These boxes correspond to regions in which the lattice tilt is produced by (i) a single electrode connecting the QD to external contacts (dashed box) and (ii) near the set of gate electrodes used to define the QD device (solid box).

The results can be understood by systematically moving from simple to progressively more complex electrode geometries. First, the magnitude of the lattice tilt was measured in the sSQW
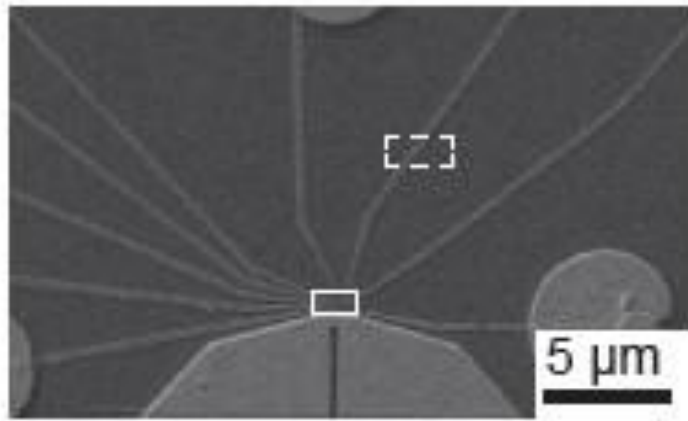
Figure 2-1: SEM image of a Si QD device showing the regions of interest in which x-ray nanodiffraction was used to probe the structural distortion. The regions of interest for the x-ray nanodiffraction are outlined with the two boxes. The dashed box indicates a region where a single linear gate electrode is deposited, and the solid box shows where many gate electrodes are closely deposited to make the electrostatically defined QD region.

near a single linear gate electrode. The corresponding strain differences of sSQW were extracted from the curvature resulting from lattice tilt. The results were compared with an elastic calculation using the edge force model to determine the interface residual stresses immediately beneath the electrode. A second series of measurements were conducted in the gate electrode region, which exhibits a more complex variation arising from the same set of interface stresses.

2.1.2 Si quantum well in Si/SiGe heterostructures

A schematic of the Si/SiGe heterostructure is shown in Figure 2-2. The layer sequence consists of a several micrometer-thick relaxed $Si_{1-x}Ge_x$ layers grown on a Si (001) substrate with a linearly graded Ge concentration from x = 0 to x = 0.3. A Si/SiGe heterostructure consisting of layers with the following thicknesses and composition was grown on this relaxed layer. It consisted of a 91 nm $Si_{0.7}Ge_{0.3}$ layer, the 10 nm sSQW, a 300 nm $Si_{0.7}Ge_{0.3}$ buffer, and a 5 nm Si cap. The lattice mismatch between Si and the relaxed SiGe layer leads to a 1% biaxial in-plane strain in the sSQW. Palladium (Pd) metal gate electrodes were defined and deposited using electron beam
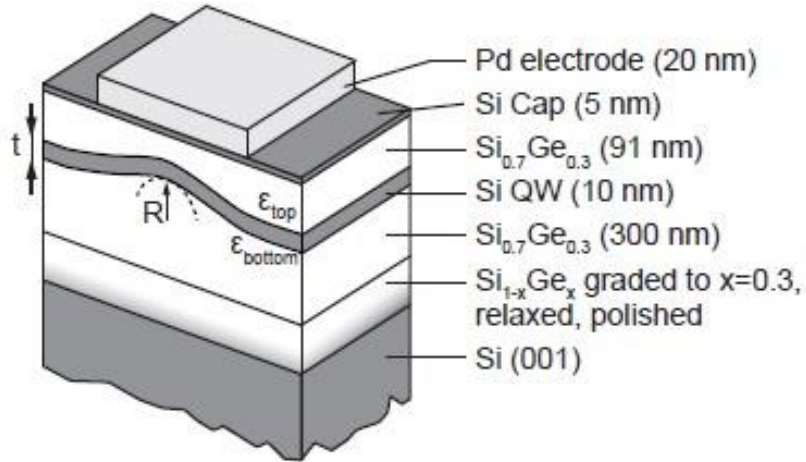
Figure 2-2: Cross section of the Si/SiGe heterostructure and Pd gate electrode. The sSQW is deformed with electrode-stress-induced radius of curvature R due the transferred stress from the electrode. The strain difference between bottom and top layer of SQW is defined as t/R.

lithography and electron beam evaporation, respectively, to electrostatically define QD structure.

The thickness of Pd electrode was 20 nm. The sSQW layer is curved with the radius of curvature

(*R*) as shown in Figure 2-2. The curvature leads to a strain difference between the bottom and top

of sSQW layer (ε_{bottom} - ε_{top}). The details of this elastic configuration are discussed in Chapter

2.4.1.

It is important to note that the lattice is also distorted in the regions far from the electrodes

due to effects related to the relaxation of the SiGe layer. The SiGe layer that relaxes during

deposition via dislocation formation that results in a characteristic cross-hatch structure [20, 21].

This plastic deformation during Si/SiGe heteroepitaxy induces a structural deformation of sSQW.

Due to the bending, a magnitude of the strain difference over the SQW thickness reaches

approximately 10^{-6}, resulting in conduction band change by 0.014 meV [22].

2.2   X-ray diffraction

2.2.1   Simulated diffraction patterns

A θ-2θ coupled scan of Si/SiGe heterostructures was simulated to provide insight into diffraction features around 004 sSQW Bragg reflections along the out-of-plane scattering vector (q_z). Structural deformations were not considered in the simulation. SiGe layers grown on Si substrate are usually tilted with respect to the substrate due to a substrate miscut [23] and sSQW layer grown on SiGe shares the same orientations with SiGe layer [24]. Therefore, in the simulation, the Si substrate was excluded because the substrate 004 Bragg reflection is located in a different q_z direction than the SiGe and sSQW layers.

Figure 2-3 shows a simulated θ-2θ coupled scan of a 91-nm-thick SiGe and a 10-nm-thick-sSQW. The simulation was conducted under conditions corresponding to the use of collimated or "parallel" incident x-ray beam. The simulation employed the kinematic scattering lattice sum method [25].

There are several important aspects of the simulation of the diffraction pattern. In the kinematic scattering approximation, the incoming X-rays are elastically scattered by the crystal lattice without absorption or multiple scattering. The diffracted intensity was calculated using the multilayer lattice sum method [25]. This sum considers a linear addition of several lattice sums,

one from each layer. The appropriate x-ray phase factor according to the position of the layer along the thickness is also considered.
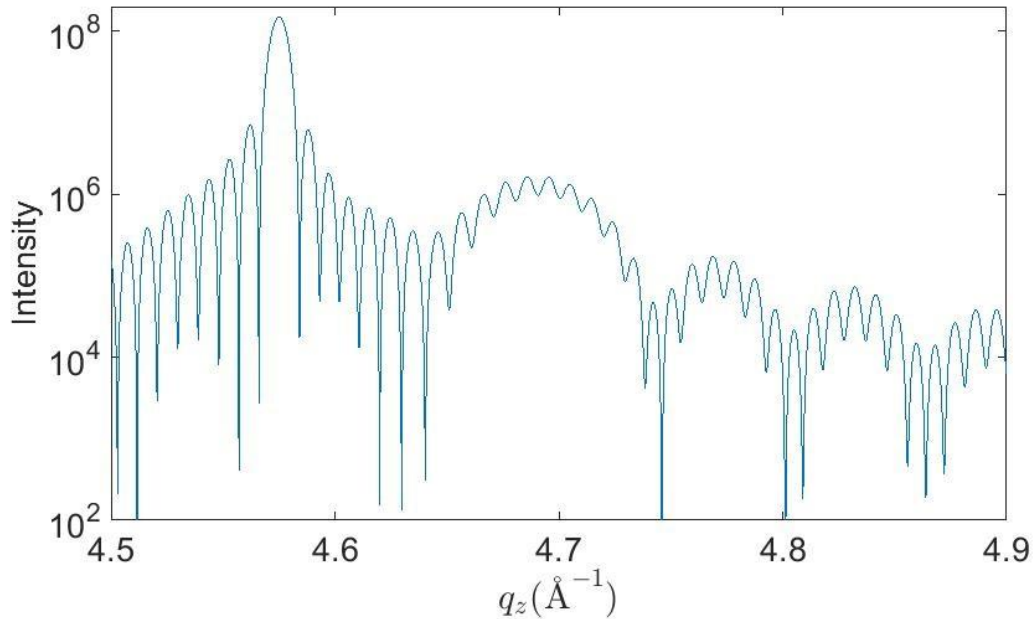
Figure 2-3: Simulated θ-2θ coupled scan of the sSQW and the top SiGe. The position of the Bragg peaks from the top SiGe and the sSQW along q_z are at 4.58 Å^{-1} and 4.69 Å^{-1}, respectively. Narrow and broad oscillating fringe components are from the thicknesses of the top SiGe and sSQW layers, which are 91 nm and 10 nm, respectively.

The simulation exhibits a series of diffraction features as shown in Figure 2-. The specular position of 004 Bragg reflections from the SiGe and sSQW layers are at $q_z = 4.58$ Å^{-1} and 4.69 Å^{-1}, respectively. The peak intensity of the Bragg reflection from the top SiGe layer is a factor of 150 greater than the peak intensity of the sSQW layer. Thickness fringe patterns oscillating with two different spatial frequencies are apparent in Figure 2-. The spacing of these fringes originates from thicknesses of the top SiGe and sSQW layers. A more detailed, quantitative comparison between the thickness fringes in the X-ray diffraction patterns is discussed in Chapter 2.3.

The diffraction patterns of Si/SiGe heterostructures were also simulated considering kinematic scattering of the focused X-ray beam produced by zone plate optics [26]. The result of

the simulated coherent diffraction pattern in comparison with the experimentally acquired coherent diffraction data is discussed in Chapter 2.3.

2.2.2 X-ray fluorescence microscopy

Compositional information can be gathered from a sample by X-ray fluorescence. When the incoming X-ray beam has sufficiently high energy relative to the binding energy of the core electrons of target atoms, the core electrons are knocked out from the shells, and the atoms become ionized. Outer shell electrons fall into the empty core states, releasing energy in the form of photons. This emission of light is referred to as fluorescence, a radiation process for which the photon energy is determined by the characteristic energy difference between the initial and final electron states [27].

The fluorescence signals in the experiments presented in this chapter were recorded by a silicon drift diode fluorescence detector. Fluorescence photons excite the electrons in the diode, and the excited electrons drift to the anode preamplifier. The number of excited electrons is proportional to the energy of the characteristic fluorescence x-ray photon. The output voltage of the preamplifier is digitized and sorted by pulse height in the corresponding channels of a multichannel analyzer. Choosing a value from the channel from the spectra recorded in a scanning the X-ray map provides an x-ray fluorescence microscopy image. The images provide a map of the distribution of the selected element on the sample surface.
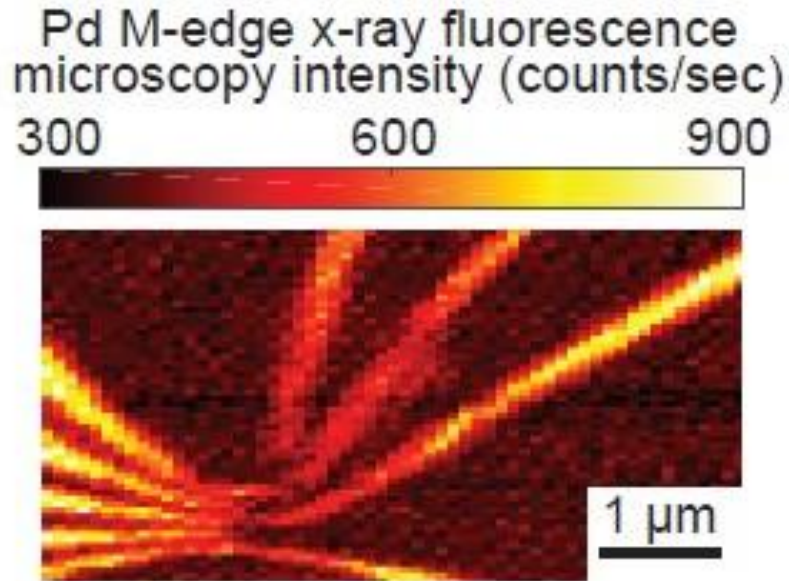
Figure 2-4: Map of the Pd M-edge fluorescence intensity in the quantum device region using x-ray nanobeam fluorescence microscopy. The fluorescence intensity becomes bright when the x-ray nanobeam illuminates the middle of each electrode, showing that nine Pd gate electrodes are deposited.

In this experiment, a Vortex-EX fluorescence detector was used to measure the X-ray fluorescence signal. The Pd M-edge fluorescence signal was selected for x-ray fluoresence microscopy maps in order to determine the positions of the electrodes and choose the areas of interest for sturctural studies. An advantage of this approach is that it allows important areas, such as the QD regions, to be determine precisely. Figure 2- shows a map of Pd M-edge fluorescence intensity indicating the location of the Pd electrodes in the QD device region.

2.3   X-ray nanodiffraction patterns arising from deformation in crystal

2.3.1   Shift of diffraction patterns due to lattice tilts

An x-ray detector image of a Si/SiGe heterostructure diffraction pattern acquired at the Bragg angle of 27.64° is shown in Figure 2-(a). One of the main features of the diffraction pattern is the set of vertical thickness fringes resulting from the 91-nm thick SiGe layer. The circular shadow observed in the middle of the diffraction pattern is from the center stop. The fringe spacing corresponds to a reciprocal-space separation (Δq_z) of 0.007 Å^{-1}. The thickness fringe arising from the sSQW is predicted to be $\Delta q_z = 0.063$ Å^{-1}, and does not appear in the span of the diffraction pattern because the focused X-ray angular convergence of 0.24° covers a wavevector range of only $\Delta q_z = 0.038$ Å^{-1}.

Figure 2-5: (a) Detector image of a diffraction pattern of the sSQW. Because the detector can capture two-dimensional reciprocal space information, the thickness fringe along the Δ2θ-direction is also visible. The thickness fringe arising from the 91-nm thick SiGe layer is superimposed on the sSQW Bragg peak, and the shadow of the center stop is also visible in the middle of the diffraction pattern. (b) Stack of the Tilt-direction intensity line profiles. The x-ray nanobeam was laterally displaced across the electrode at fifty locations. The diffraction patterns are summed along Δ2θ-direction to calculate the centroid along the Tilt direction. The summed diffraction patterns are stacked up on each other. The green curve exhibits change in centroid.

Structural deformation leads to a shift of the diffraction pattern on the detector. Surface features such as electrodes can impose lattice tilt due to transferred interface stress, which causes shifts in the diffraction pattern. The corresponding direction of the shift can be a combination of the *Tilt-* and *Δ2θ*-directions on the detector plane depending upon the direction of the deformation. For example, if the axis of rotation of the lattice tilt is parallel to the propagating X-ray beam direction, the diffraction pattern shifts along the *Tilt*-direction.

Figure 2-(b) shows the spatial variation of the shift of the diffraction pattern along the *Tilt*-direction. The X-ray nanobeam was laterally displaced along a line across the electrode and x-ray diffraction patterns were an acquired at a series of locations. Each diffraction pattern was integrated along the *Δ2θ*-direction to produce a plot of the intensity as a function of the angle spanning the *Tilt*-direction. These *Tilt*-direction intensity line profiles were then stacked to make the plot shown in Figure 2-(b). The map clearly shows that there is a shift of the diffraction patterns along the *Tilt*-direction as a function position near the electrode.

The magnitude of the shift of diffraction patterns was measured by calculating the centroid of the *Tilt*-direction intensity line. The centroid is given by:

$$X_c = \frac{\sum X_i I_i}{\sum I_i}$$

Equation 2-1

Here X_c is the centroid pixel position along the *Tilt*-direction of the diffracted intensity and I_i is the intensity at the pixel position X_i along the *Tilt*-direction. The profile of the centroid pixel positions is shown as the green curve in Figure 2-(b).

2.3.2 Fourier transform of thickness fringes in diffraction patterns

2.3.2.1 Thickness fringe visibility and Fourier transform intensity

In addition to the shift of the diffraction patterns, the electrodes-induced deformation leads to additional distinctive features associated with the thickness fringes of the x-ray diffraction patterns. In areas far from the tilted region, the SiGe thickness fringes appear in the diffraction pattern acquired at the Bragg angle of 27.64°, as shown in Figure 2-(a), which is superimposed over the broad sSQW fringe.

The experimental diffraction patterns were compared with simulated diffraction patterns. In order to do this, the coherent diffraction patterns of sSQW were simulated using a method described by Ying *et al.* [26]. Figure 2-(b) shows a simulated diffraction pattern that was computed using conditions matching the experiment. The experimental and simulated diffraction patterns exhibit the same thickness fringe patterns from the SiGe layer and have the same general distribution of diffracted intensity.
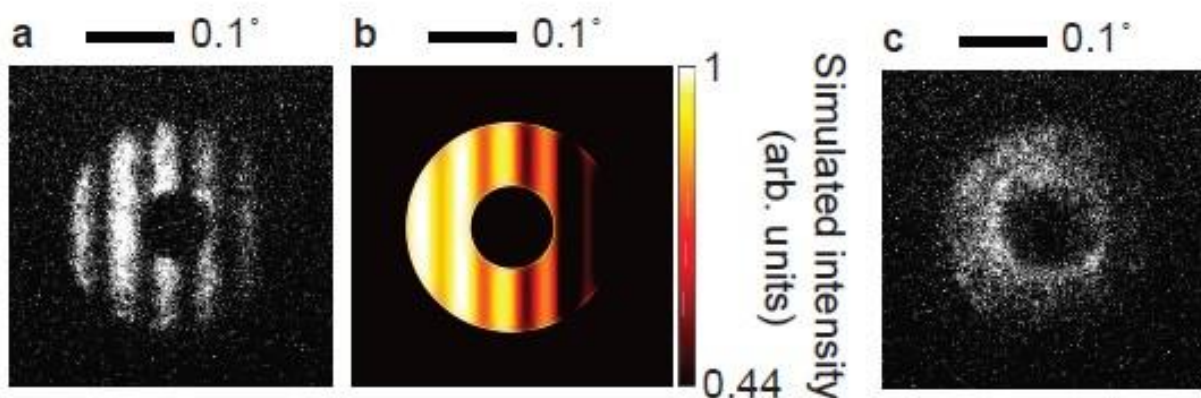
Figure 2-6: Comparison between experimental diffraction pattern and simulation, and between the diffraction patterns acquired (a) far from the electrode and (c) at the tilted region. (b) Simulated diffraction pattern using the method of Ref [26] and conditions corresponding to (a).

In the region near the electrodes, however, the experimental diffraction patterns were far more complicated than in the regions far from the electrodes. Figure 2-(c) shows a diffraction pattern acquired at the Bragg angle of 27.64° in a tilted region near an electrode. The diffraction pattern only again arises from the sSQW but the SiGe thickness fringes are not apparent. The interference producing the fringe features does not occur because the top and bottom interfaces of the SiGe layer are not parallel to each other in the tilted region. The diffraction patterns shown in Figure 2-(a) and 2-6(c) are located at different positions on the detector, because the diffraction pattern acquired at tilted regions shifted along the *Tilt*-direction due to lattice tilts as discussed in Chapter 2.3.1.
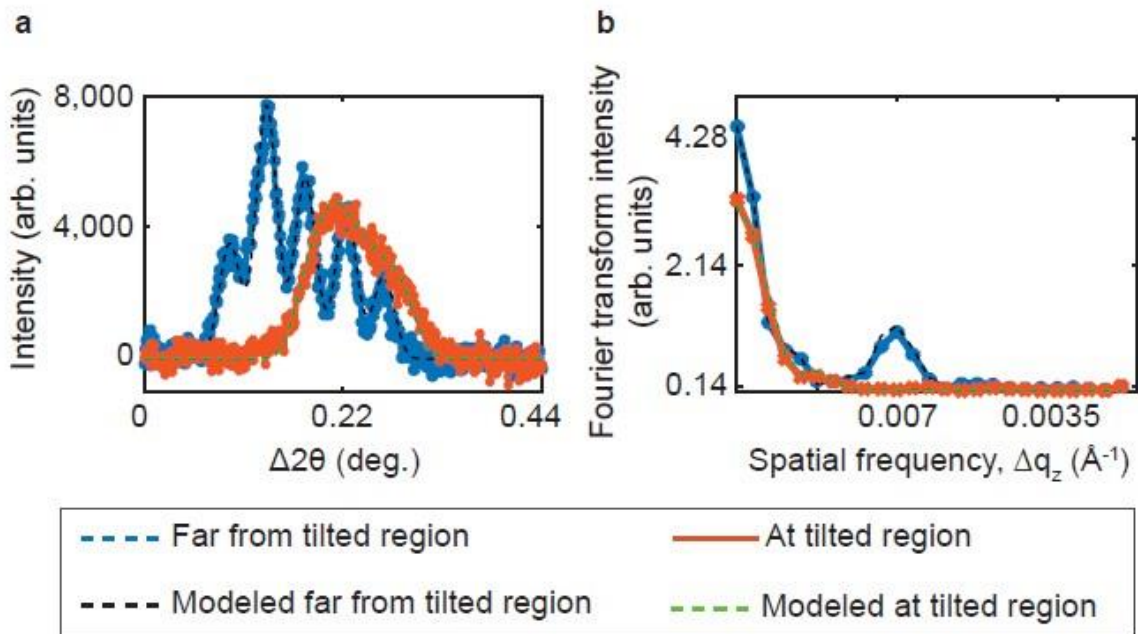
Figure 2-7: (a) Intensity line profiles of diffraction patterns integrated along the Tilt-direction of the detector, acquired in regions far from the tilted region (blue) and at the tilted region (orange). (b) Fourier transform intensities of the two intensity line profiles and the models shown in (a) as a function of spatial frequency, Δq_z. The Fourier transform intensity at $\Delta q_z = 0.007$ arises from the thickness fringe of the top SiGe layer, and the results of the Fourier transform of the model agree, as shown in the dotted curves.

In addition to the *Tilt*-direction intensity line profiles, *Δ2θ*-direction intensity line profiles of diffraction patterns may also be plotted by integrating diffraction pattern along the *Tilt*-direction. Figure 2-(a) shows the *Δ2θ*-direction intensity line profiles acquired far from the tilted regions (blue) and with the x-ray beam located at a tilted region (orange). The thickness fringes from the SiGe layer are visible in the *Δ2θ*-direction intensity line profile from the diffraction pattern acquired far from the tilted regions, but they are not visible in the diffraction pattern acquired at the tilted regions.

The *Δ2θ*-direction intensity line profiles can be used to confirm that the thickness fringe periodicity is missing visibility by computing the Fourier transform intensity of the fringe patterns. It is assumed that the Fourier transform intensity of the fringe patterns decreases as the fringe patterns disappear from the diffraction pattern. To confirm whether or not the change in Fourier transform intensity of the fringe patterns originates only from vanishing fringe patterns, the *Δ2θ*-direction intensity line profiles were modeled, and their Fourier transform intensities are compared with the experimental data.

The Fourier transform intensity at a spatial frequency matching the thickness fringe spacing $\Delta q_z = 0.007$ Å^{-1} can be used to verify the fringe visibility, as indicated in Figure 2-(b). The Fourier transform intensity at $\Delta q_z = 0.007$ Å^{-1} decreases as the thickness fringes disappear, and it becomes less than 0.14 a.u. when the thickness fringe is completely invisible. The results of the model fit well with the measured the *Δ2θ*-direction intensity line profiles, and the trends of their Fourier transform intensity at $\Delta q_z = 0.007$ Å^{-1} indicates that the decreasing Fourier transform intensity originates from the vanishing thickness fringe in the diffraction pattern acquired in the tilted regions.

2.3.2.2 Fringe intensity maps and fringe intensity variation in the in quantum dot device region

In Figure 2-(b), the Fourier transform intensity at $\Delta q_z = 0.007$ Å^{-1} is a factor of approximately 10 smaller when the thickness fringes are absent. An advantage of using the Fourier transform approach to analyze the structural deformation is that the visibility of the fringe pattern can be rapidly measured for large number of diffraction patterns.
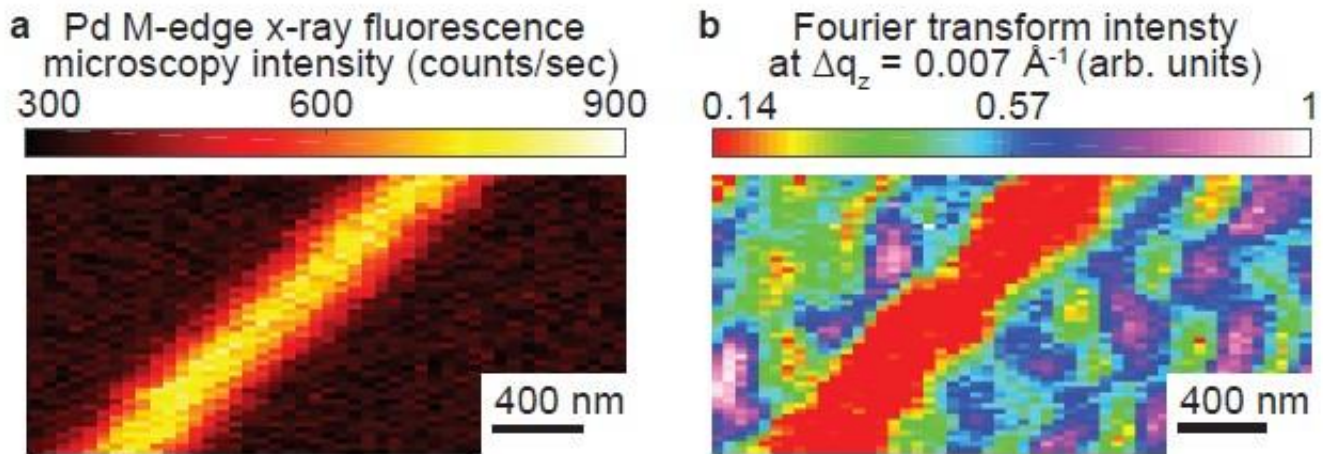
Figure 2-8: Map of the Pd M-edge fluorescence intensity in the region of a single linear Pd electrode using x-ray nanobeam microscopy. The intensity becomes bright when the x-ray beam illuminates the middle of the electrode. (b) Fourier transform intensity at a fringe spacing of $\Delta q_z = 0.007$ Å-1, exhibiting the disappearance of the SiGe layer interference fringes in the tilted region.

Figure 2-(a) shows a map of the Pd M-edge fluorescence intensity within the region of the dashed box in Figure 2-1, indicating the position of the single Pd electrode. Tracking the change in Fourier transform intensities at $\Delta q_z = 0.007$ Å^{-1}, a map of fringe visibility in Figure 2-(b) shows that the Fourier transform intensities are approximately a factor of 10 lower under the electrodes than in the region far from the electrodes, indicating that the thickness fringes disappeared under the electrode due to the structural deformation. The Fourier transform intensity is also reduced at

the boundaries of the cross-hatch regions far from the electrode. The fringe visibility map is thus a strong indicator of structural deformation in the sSQW.

Figure 2-(a) shows the Fourier transform intensity at a spatial frequency of $\Delta q_z = 0.007$ Å^{-1} in the area of the QD, matching the region shown in Figure 2-. In the QD device region, the electrodes are tightly patterned and the stress fields overlap, producing complex deformation. The quantum QDs is in the bottom left corner (black box) Figure 2-(a). The Fourier transform intensity is too low to recognize the locations of individual electrodes.
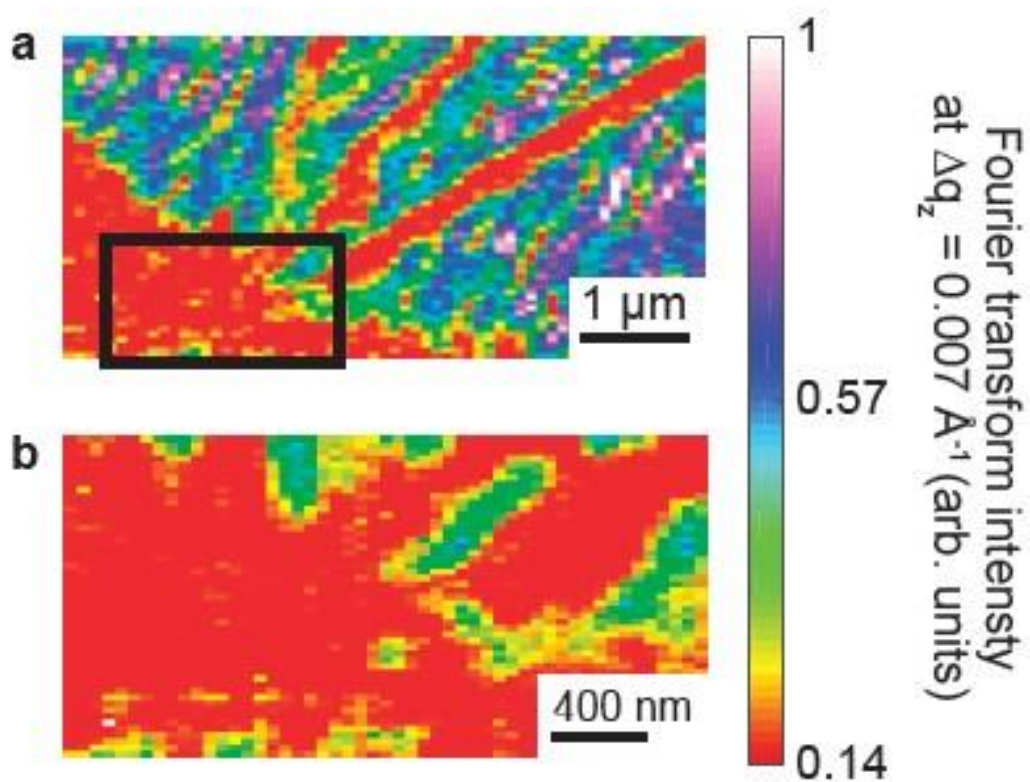
Figure 2-9: Fourier transform intensity at fringe spacing of $\Delta q_z = 0.007$ Å^{-1} for the areas shown in Figure 2-. The black box indicates the QD region where many electrodes are closely deposited, and the Fourier transform intensity of this region is shown in (b).

2.3.2.3 Deducing the angular shift of diffraction pattern from the Fourier transform phase

There is also structural information contained in the phase Fourier transform of the diffraction patterns. The Fourier transform phase can be used to estimate the magnitude of the angular shift of the diffraction patterns along the *Tilt*-direction. The analysis using the Fourier transform complements the centroid approach described above. The phase information of the particular spatial frequency is obtained by calculating the arctangent of the ratio of imaginary to real parts of the Fourier transform. Changing the unit of the phase from degrees to the number of pixels can be achieved by multiplying the phase information in degrees by $\frac{\# \, of \, total \, pixels}{360 \times spatial \, frequency}$.

Figure 2-10 shows the stack of the *Tilt*-direction intensity line profiles that was previously shown in Figure 2-(b). The shift calculated using the centroid line is plotted as the green line overlaying the shifts. The Fourier transform phase information of the *Tilt*-direction intensity line profiles is shown the blue line for comparison with the centroid approach. The phase information reasonably matches the centroid line in Figure 2-10. However, the width of the *Tilt*-direction intensity line profile significantly changes in the more deformed regions, which can result in different values of spatial frequency and slightly different structural information and thus we used the shifts from the centroid for our subsequent analysis.
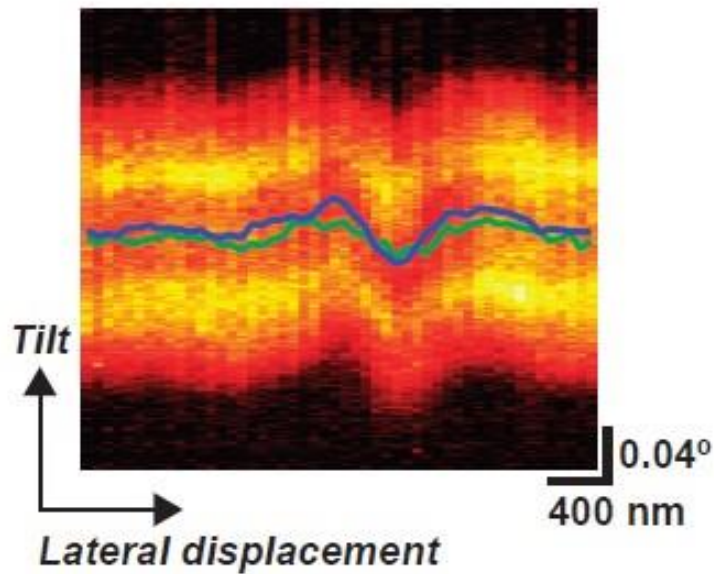
Figure 2-3: Stack of the Tilt-direction intensity line profiles for the comparison between two methods to track the shift of the diffraction pattern. The centroid information (green) already introduced in Figure 2- (b) is compared with the phase information (blue) extracted from the Fourier transform of the diffraction patterns.

2.4 Electrode-stress-induced deformation

The process of depositing the metal electrodes results in stress that results from a variety of mechanisms. The polycrystalline metal electrodes form via an island coalescence process during deposition [29, 30]. The islanding process is often described as the Volmer-Weber mechanism of thin film growth [28]. Surface-feature-stress-induced structural deformations have previously been probed in other semiconductor systems using various x-ray diffraction studies [8, 9, 11].

2.4.1 Mechanical elastic model

An analytical elastic model was employed to interpret the measured lattice tilts. Lattice tilts considered by I. A. Blech, *et al.* [31] are based on rotations of (H00) planes, and are equivalent to rotations of (00L) planes, which is the case in our experiments. The model selected for the analysis was termed the edge-force model. The primary assumption of the edge-force model is that the
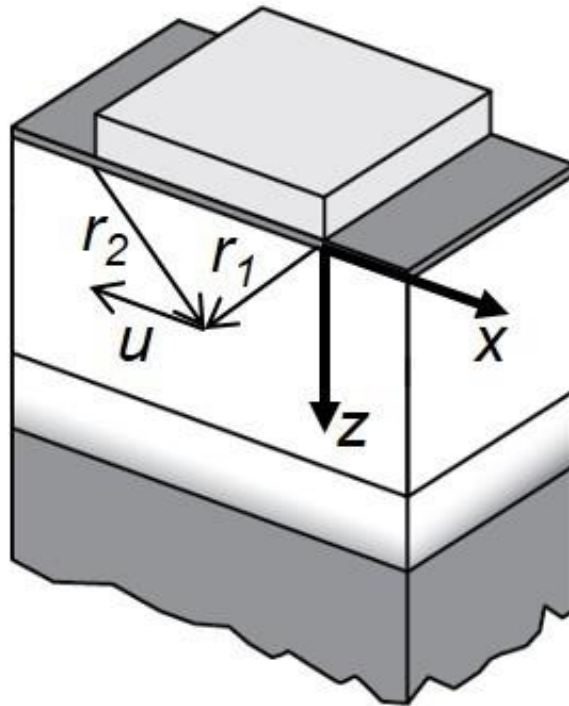
Figure 2-4: Si/SiGe heterostructure showing lattice displacements along the x-axis (u), which is a function of the two radial distances r_1 and r_2 measured in the x-z plane.

residual interface stress underneath the electrodes is elastically transferred to the substrate through

the electrode edges [1]. It is supposed that the lattice tilts arise only from the elastically transferred

residual stresses, and that the axis of rotation is parallel to the electrode length direction. As

illustrated in Figure 2-11, the electrode is assumed to be infinite along the *y*-axis, and lattice

displacements only occur along the *x*-axis. The contribution of the spatial variation in plastic

deformation is not considered. Ultimately, analysis using this model allows the stress imparted on

the sSQW by the Pd electrode to be inferred from an elastic analysis of the distortion.

The model considered of a 20-nm-thick and 230-nm-wide infinitely long Pd electrode

deposited on single SiGe layer. The use of a single SiGe layer is an appropriate approximation

given the thinness of the sSQW layer. It also simplifies the problem by neglecting the interface

between SiGe layer and sSQW layer, at which two different sets of elastic constants would be needed.

The lattice displacement along the x-axis is defined as u and is a function of two radial distances, r_1 and r_2 from the two edges of the electrodes in the x-z plane, as shown in Figure 2-11. The lattice tilt can be calculated by taking the first derivative of u with respect to the depth using:

$$\frac{du(r_1, r_2)}{dz} = \frac{2Sz(1+v)}{\pi E}\left\{(1-v)\left[\frac{1}{r_2{}^2} - \frac{1}{r_1{}^2}\right] + \left[\frac{x_2{}^2}{r_2{}^4} - \frac{x_1{}^2}{r_1{}^4}\right]\right\}$$

Equation 2-2

Here S is the interface residual stress-thickness product, v is Poisson's ratio, and E is the Young's modulus of SiGe.

A 3D drawing of the depth-dependence of the lattice tilt angle is shown in Figure 2-12. The sSQW position is outlined with a black box at a depth of 100 nm. In the model, the lattice tilt angles are $\pm 0.13°$ immediately under the electrode edges. The magnitude of the tilt decreases through the thickness and becomes around 0.03° at the depth of the sSQW. A more detail analysis of the results is discussed in Chapter 2.4.4.
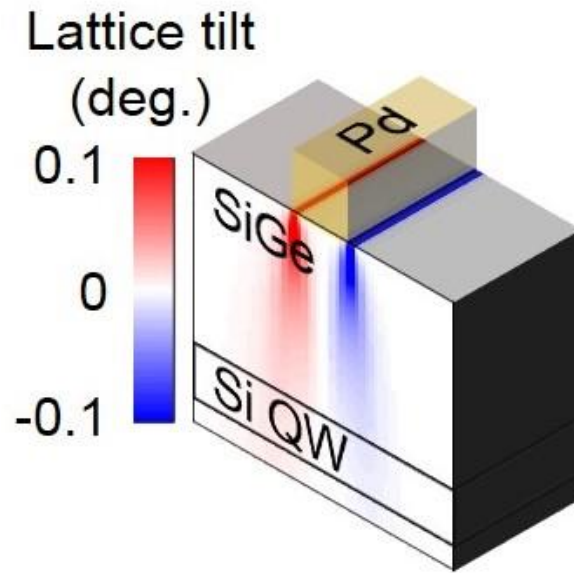
Figure 2-5: 3D map of lattice tilt angles calculated from the first derivative of u in terms of the depth z. The magnitude of lattice tilts under electrode is depth dependent, and it becomes 0.03° approximately 100 nm below the surface at which sSQW is located (outlined with a black box).

2.4.2 Apparent position of electrodes and Si quantum well

There is a 90-nm offset in position between the apparent center of the electrode in the x-ray fluorescence microscopy map in Figure 2-(a) and the apparent center of the distortion in the diffraction maps, for example as in Figure 2-(b). This effect results from the experimental X-ray diffraction geometry because the depths of the electrode and sSQW are different. The incident X-ray beam at the Bragg angle of 27.64° illuminates both the electrode and the sSQW under the electrode at laterally different positions, as illustrated in Figure 2-13(a). The position of the red dot in Figure 2-13(a) the particular location where the incident x-ray beam intercepts the surface at the Bragg angle. The incident beam at this location is labeled with wavevector k_i, which illuminates the sSQW buried immediately beneath the electrode. The x-ray beam k_i' represents the location of the beam at a different position in the scan, at which beam intersects the edge of electrode and
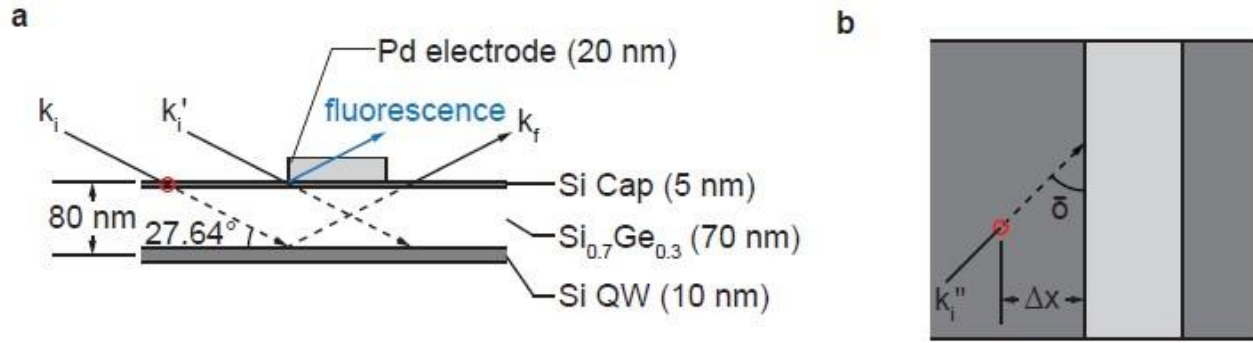
Figure 2-6: (a) Cross-sectional diagram of X-ray diffraction geometry explaining the apparent offset of the apparent electrode positions between Figures. 2-8(a) and 2-8(b). The red dot is a particular surface location at which the incident x-ray k_i, illuminates sSQW buried immediately beneath the electrode. k_i', is another incident x-ray at which fluorescence signal from electrode is initially generated. (b) Plan view of experimental X-ray diffraction geometry. The direction of incident X-ray and the electrode direction different by an angle δ provides Δx = 108 nm when considering the approximate value of the angle δ of 45°.

generates the fluorescence signal. The lateral distance between the surface locations intersected by

k_i and k_i' is (80 nm) $\tan^{-1}(27.49°) = 153$ nm.

The experimentally observed offset is slightly more complicated because the orientations of the footprint of the incident X-ray and the direction of the electrode are not usually parallel in the experiment, rather they differ by angle, δ. In Figure 2-13(b), a plan view of the diffraction geometry shows the incident X-ray, k_i'', deviates from the electrode length direction by δ. Considering δ = 45°, which is the experimental condition, a theoretical distance between the red dot and the electrode (Δx) is calculated to be 153 nm · cos45° = 108 nm. In the experiment, the observed Δx was 90 nm, which is close to the theoretical difference.

2.4.3 Rotation matrix

As discussed in Chapter 2.4.1, the electrode is infinitely long along the *y*-axis, and the lattice planes are displaced mainly along the *x*-axis which is perpendicular to the electrode length direction. Owing to lattice displacements, lattice tilts occur with respect to the *y*-axis as the axis of

rotation in which the diffraction pattern on the detector shifts only along the *Tilt* direction. In the experiment, however, the diffraction pattern on the detector shifts not only along the *Tilt* direction but also the *Δ2θ* direction because the incident X-ray and the electrode length directions are not usually parallel as discussed in Chapter 2.4.2.

The shifted diffraction pattern on the detector consisting of both components along the *Tilt*- and *Δ2θ*-directions must be decoupled to calculate the lattice tilt angle only associated with the lattice displacement along the *x*-axis and perpendicular to the electrode length direction. First, the shift of the centroid of the diffraction pattern along both the *Tilt*- and *Δ2θ*-directions was

Figure 2-7: Illustration of a Cartesian coordinate Tilt-Δ2θ plane. P(Tilt, Δ2θ) is a position of diffraction pattern on detector. P(α⊥, α‖) is a new position on α⊥-α‖ plane converted by a rotation matrix. The α⊥ and α‖ are directions perpendicular and parallel to electrode length direction, respectively. The shift in the diffraction pattern on the detector is determined by computing the shift of centroid of the diffraction patterns on the Tilt-Δ2θ plane and then reconsidered on the α⊥-α‖ plane by the rotation matrix.

calculated. Then the change in the centroid of diffraction patterns was converted to the

corresponding tilt angle perpendicular ($\alpha_\perp$) or parallel ($\alpha_\parallel$) to the electrode direction using the rotation matrix described in Eq. 2-3. Based on this assumption, the angle between the electrode and the X-ray is δ is shown in Figure 2-14.

$$P\big(0,\alpha_\parallel\big) = \overline{AB} + \overline{BO} = P(Tilt,0)sin\delta + P(0,\varDelta 2\theta)cos\delta$$

$$P(\alpha_\perp,0) = -(\overline{BD} - \overline{CD}) = P(Tilt,0)cos\delta - P(0,\varDelta 2\theta)sin\delta$$

$$\begin{pmatrix}P\big(0,\alpha_\parallel\big)\\P(\alpha_\perp,0)\end{pmatrix} = \begin{pmatrix}cos\delta & sin\delta\\-sin\delta & cos\delta\end{pmatrix}\begin{pmatrix}P(0,\varDelta 2\theta)\\P(Tilt,0)\end{pmatrix}$$

Equation 2-3

2.4.4 Lattice tilt maps

In the X-ray nanodiffraction experiment, the structural deformation of the sSQW was studied in detail in the region of an isolated single Pd electrode. The location of this electrode on the sample is indicated by the dashed box in Figure 2-1. Figure 2-15 shows a map of the lattice tilt angle in the same regions as the fluorescence map shown in Figure 2-(a). The tilt angle reaches $\pm 0.03°$ at the two electrode edges, and the sign of tilt angle rapidly changes at the middle of the electrode. Based on the sign of the tilt angle, the sSQW planes have the concave-down bending beneath the electrode. The slight mismatch of the electrode positions in the fluorescence and the tilt images is due to the difference in the depth between the electrode and the sSQW as discussed in Chapter 2.4.2 above.
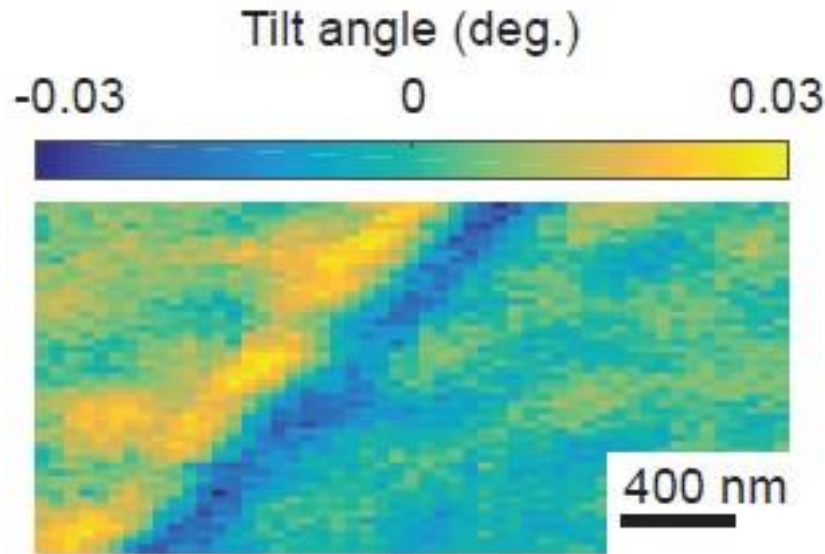
Figure 2-8: Map of the sSQW lattice tilt angles in a single electrode area indicated by the dotted box in Figure 2-1. Lattice tilt angles are measured by computing shifts in diffraction patterns from sSQW, for which the maximum magnitude becomes 0.03° under the electrode. The sign of lattice tilt changes at the middle of the electrode, which might arise from lattice deformations by elastically transferred electrode stress.

The elastic deformation in the region where several electrode patterns define the QDs is more complicated than for a region of a single electrode. Figure 2-16(a) shows a Pd fluorescence map in the QD region indicated by the solid box in Figure 2-1. The locations of electrode patterns are outlined with the dotted lines, and the asterisk indicates the position of a QD. The tilt magnitude of the same region is shown in Figure 2-16(b). The tilt magnitude reaches up to 0.05° at the left side of the map where the five electrodes (dotted lines) are closely spaced. This magnitude is a factor of 2.5 larger than at the single electrode. The structural deformation is larger in this area due to the overlap of the stress fields of adjacent electrodes, as previously observed at a much larger scale in metal test patterns on Si [8].
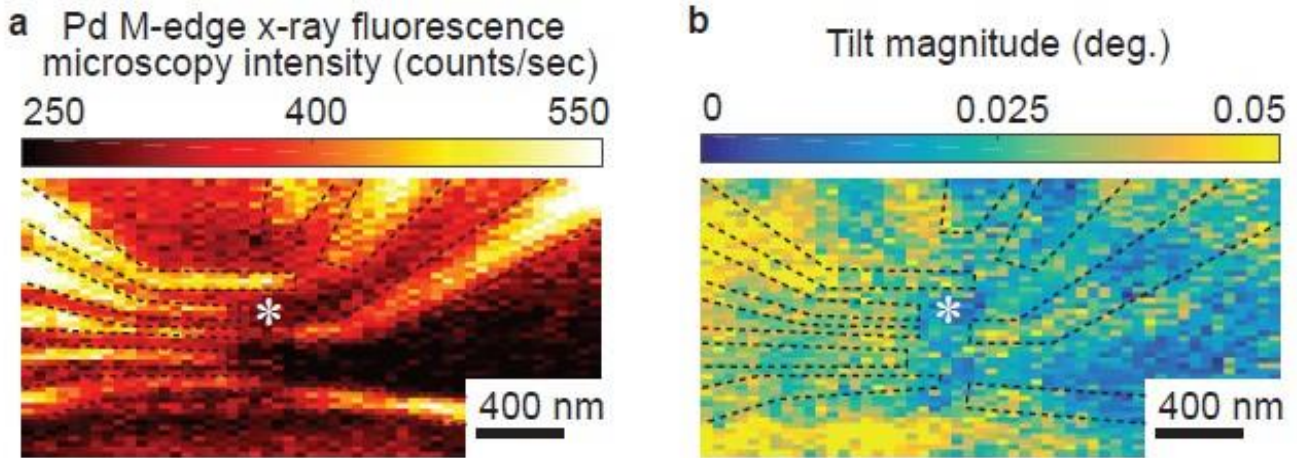
Figure 2-9: (a) Map of the Pd M-edge fluorescence intensity in the QD region. Many electrodes are closely deposited, as outlined with dotted lines. The asterisk indicates the position of a QD. (b) Tilt magnitude map of the sSQW lattice planes in the same area. The maximum tilt magnitude is 0.05°, which is a factor of 2.5 larger than at the single electrode.

2.4.5 Strain difference

2.4.5.1 Curvature and strain
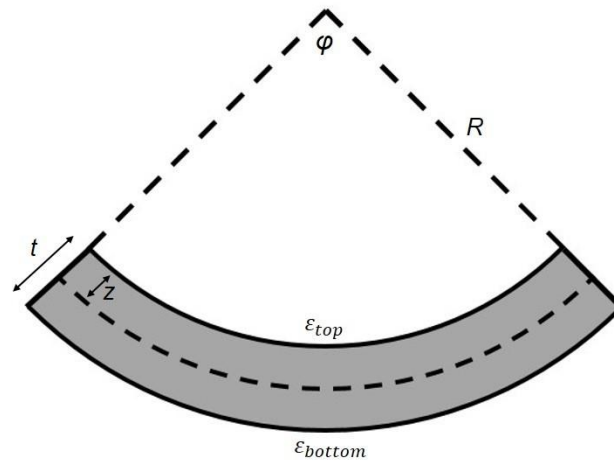
Figure 2-10: Diagram showing the concave-up bending of sSQW (gray) arising from the lattice tilt under the electrode with the radius of curvature (R), thickness (t), and the tilt angle (φ). Strain neutral plane is indicated by the dotted line inside gray box. Z is the distance between the middle plane and the top layer.

The difference in strains between the bottom and top of sSQW layer can perturb the local energy band structure. The magnitude of this effect can be comparable to the electron charging energy in the QD device [16, 22]. Figure 2-17 shows the bending of the sSQW due to the lattice

tilt under the electrode. The radius of curvature and the thickness of the sSQW are defined as R and t, respectively.

In the experiment, the curvature, R can be measured by calculating the first derivative of the lattice tilt angles (φ) in terms of lateral distance ($d\varphi/dx$), which is equivalent to d/dx (du/dz) in the edge force model. The strain difference ($\varepsilon_{bottom} - \varepsilon_{top}$) is estimated by calculating t/R as derived in Eq. 2-4. When φ is small, the lateral length of the neutral plane of the sSQW is φR. The strains are the difference in the lateral length as a result of bending as compared to that of at the neutral plane, which are *-z/R* and *(t-z)/R* for ε_{top} and ε_{bottom}, respectively. The sign of the strain difference under the electrode in the experiment was negative due to a concave-down bending of the sSQW.

$$\varepsilon_{top} = \frac{\varphi(R-z) - \varphi R}{\varphi R} = -\frac{z}{R}$$

$$\varepsilon_{bottom} = \frac{\varphi(R-z+t) - \varphi R}{\varphi R} = \frac{(t-z)}{R}$$

$$\varepsilon_{bottom} - \varepsilon_{top} = \frac{(t-z) + z}{R} = \frac{t}{R}$$

Equation 2-4

2.4.5.2 Strain difference in quantum dot device region

Figure 2-18(a) shows the measured lattice tilt angle (solid) and modeled tilt angle (dashed) as a function of the distance from the electrode. The center of the electrode is at position zero. The modeled tilt angle is calculated from the displacement of the lattice planes at a depth of 100 nm under the electrode. A stress-thickness product of 80 GPa·Å provides the best fit to the experimental data. The magnitude of the stress-thickness products is similar to the stress reported

in other metal thin films [29, 30, 32]. The small difference in the tilt angle between the start and end points of the blue curve in Figure 2-18(a) originate from differences in the plastic relaxation of the bottom SiGe layer.
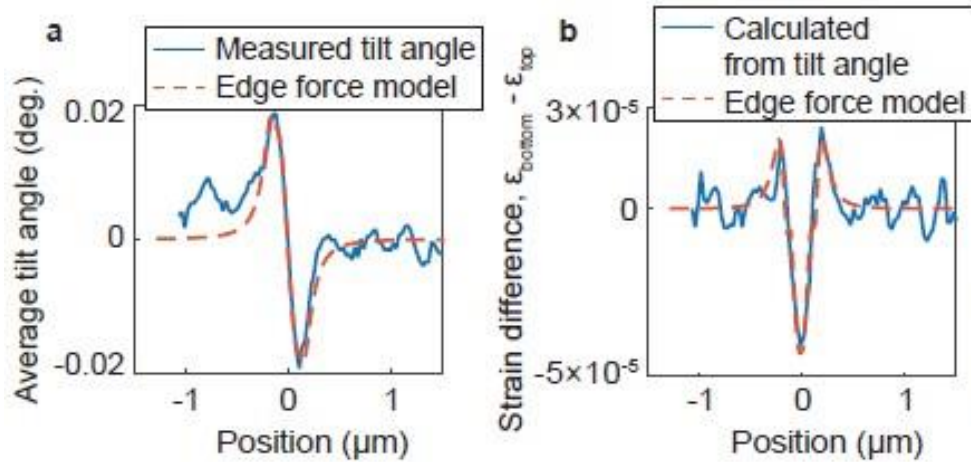
Figure 2-18: Plots of the lattice tilt and strain difference of sSQW (gray) arising from the bending curvature under the electrode.

The curvature of the sSQW is numerically extracted both from the measured and modeled tilt angles and used to calculate the strain difference between the bottom and top of the sSQW. At the position zero, which is the center of the electrode, the average tilt angle abruptly changes the sign. The steep change results in the maximum strain difference of 4×10^{-5}, corresponding to a radius of curvature of 25 μm. The maximum strain difference is a factor of 10 larger than the previously reported one, which arises from the plastic relaxation [22].

The strain difference in the region of the QD is determined using the two-dimensional curvature K_{2D} as defined in Eq. 2-5 and Eq. 2-6. The tilt angle φ both along the *Tilt* and *Δ2θ* directions are considered. In addition, φ along each direction contains two-dimensional information in positions, *x* and *y* with the interval *Δx* or *Δy* of 50 nm.

$$K_{2D}(x,y) = \nabla \frac{\nabla \varphi(x,y)}{|\nabla \varphi(x,y)|} = \frac{\varphi_{xx}\varphi_y{}^2 - 2\varphi_x\varphi_y\varphi_{xy} + \varphi_{yy}\varphi_x{}^2}{(\varphi_x{}^2 + \varphi_y{}^2)^{1.5}}$$

Equation 2-5

where

$$\varphi_x = \frac{\varphi_{Tilt}(x + \Delta x, y) + \varphi_{Tilt}(x - \Delta x, y)}{2\Delta x}$$

$$\varphi_y = \frac{\varphi_{\Delta 2\theta}(x, y + \Delta y) + \varphi_{\Delta 2\theta}(x, y - \Delta y)}{2\Delta y}$$

$$\varphi_{xx} = \frac{\varphi_{Tilt}(x + \Delta x, y) - 2\varphi_{Tilt}(x, y) + \varphi_{Tilt}(x - \Delta x, y)}{\Delta x^2}$$

$$\varphi_{yy} = \frac{\varphi_{\Delta 2\theta}(x, y + \Delta y) - 2\varphi_{\Delta 2\theta}(x, y) + \varphi_{\Delta 2\theta}(x, y - \Delta y)}{\Delta y^2}$$

$$\varphi_{xy} = \frac{\varphi_{xy,1} + \varphi_{xy,2}}{2}$$

$$\varphi_{xy,1} = \frac{\varphi_{Tilt}(x + \Delta x, y + \Delta y) + \varphi_{Tilt}(x + \Delta x, y - \Delta y) - \varphi_{Tilt}(x - \Delta x, y + \Delta y) - \varphi_{Tilt}(x - \Delta x, y - \Delta y)}{4\Delta x \Delta y}$$

$$\varphi_{xy,2} = \frac{\varphi_{\Delta 2\theta}(x + \Delta x, y + \Delta y) + \varphi_{\Delta 2\theta}(x - \Delta x, y + \Delta y) - \varphi_{\Delta 2\theta}(x + \Delta x, y - \Delta y) - \varphi_{\Delta 2\theta}(x - \Delta x, y - \Delta y)}{4\Delta x \Delta y}$$

Equation 2-6

The two-dimensional strain difference determined from the measured tilt angle information is shown in Figure 2-19(a). In this region, the strain difference measured at the asterisk is significantly larger than the one measured at the single electrode region. In Figure 2-19(b), the strain differences measured at the single electrodes and the QD regions are directely compared. The strain difference values along the bottom of the tilt image in Figure 2-15 and the vicinity of the asterisk in Figure 2-19(a), are used for the comparison between the single electrode and the QD regions, respectively. The strain difference from the QD region is a factor of 10 larger than

that from the single electrode region. The energy variation in QD region is therefore 1.4 meV, which is on the same order of magnitude of the charging energy in few-electron QDs.
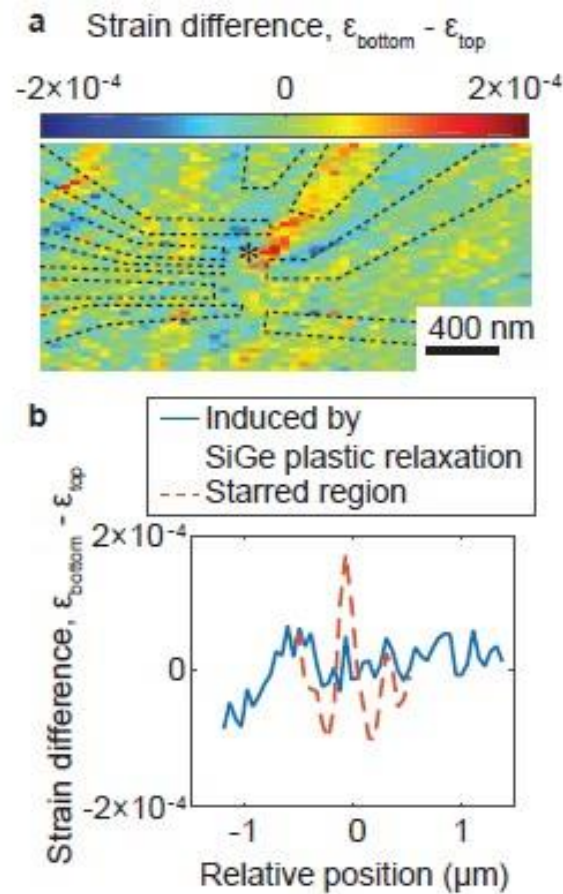
Figure 2-19: (a) Map of the strain difference across the thickness of the sSQW in the QD region. (b) Comparison between strain differences induced by the single electrode along with the intrinsic tilt from plastic relaxation of the SiGe layer and the QD electrodes near the region indicated by the asterisk in (a).

2.5   Conclusion

In conclusion, significant structural deformation of sSQW in Si/SiGe heterostructures is induced both by the plastic relaxation of the SiGe substrate and residual interface stresses imparted from the deposited Pd gate electrode on the surface. The lattice tilt resulting from the distortion can be modeled by a mechanical elastic edge force model. The model assumes that residual stress is transferred through the electrode edges and the lattice planes are displaced perpendicular to the

electrode length direction. The lattice tilt of the sSQW layer is caused by different magnitudes of lattice displacements along the depth direction.

X-ray nanodiffraction was employed to measure the lattice tilt of the sSQW by tracking the shift in diffraction patterns of sSQW layer. Both experimental data and the model indicate that the sSQW layer is curved due to the lattice tilt, resulting in a strain difference between the bottom and top of sSQW layer up to 10^{-4} over the sSQW thickness in QD region. This is a factor of 100 greater than the strain difference arising from the SiGe substrate plastic relaxation. This variation in strain contributes to the potential energy landscape difference of 1.4 meV in gate electrode-defined quantum devices, which is on the same order of magnitude of the charging energy in few-electron QDs. Thus, gate electrode-stress-induced strain variation leads to a substantial source of disorder in gate electrode-defined semiconductor quantum electronics.

The Fourier transform of the diffraction pattern provides both Fourier transform intensity and phase information of the *Tilt-* and *Δ2θ*-direction intensity line profiles and enables the characterization of structural deformation using fringe visibility and tracking shift of diffraction patterns. However, in the QD device region, the fringe visibility method lacks sufficient resolution because the size of structural deformation is larger than the size of a focused X-ray nanobeam, and phase information loses its significance because the spatial frequency of the *Tilt*-direction intensity line profiles significantly changes in the deformed regions.

2.6 References

[1] B. M. Maune, M. G. Borselli, B. Huang, T. D. Ladd, P. W. Deelman, K. S. Holabird, A. A. Kiselev, I. Alvarado-Rodriguez, R. S. Ross, A. E. Schmitz, M. Sokolich, C. A. Watson, M. F. Gyure, and A. T. Hunter, Nature **481**, 344 (2012)

[2] E. Kawakami, P. Scarlino, D. R. Ward, F. R. Braakman, D. E. Savage, M. G. Lagally, M. Friesen, S. N. Coppersmith, M. A. Eriksson, and L. M. K. Vandersypen, Nat. Nanotech. **9**, 666 (2014)

[3] D. Kim, Z. Shi, C. B. Simmons, D. R. Ward, J. R. Prance, T. S. Koh, J. K. Gamble, D. E. Savage, M. G. Lagally, M. Friesen, S. N. Coppersmith, and M. A. Eriksson, Nature **511**, 70 (2014)

[4] M. Veldhorst, C. H. Yang, J. C. Hwang, W. Huang, J. P. Dehollain, J. T. Muhonen, S. Simmons, A. Laucht, F. E. Hudson, K. M. Itoh, A. Morello, and A. S. Dzurak, Nature **526**, 410 (2015)

[5] C. B. Simmons, M. Thalakulam, N. Shaji, L. J. Klein, H. Qin, R. H. Blick, D. E. Savage, M. G. Lagally, S. N. Coppersmith, and M. A. Eriksson, Appl. Phys. Lett. **91**, 213103 (2007)

[6] E. P. Nordberg, H. L. Stalford, R. Young, G. A. Ten Eyck, K. Eng, L. A. Tracy, K. D. Childs, J. R. Wendt, R. K. Grubbs, J. Stevens, M. P. Lilly, M. A. Eriksson, and M. S. Carroll, Appl. Phys. Lett. **95**, 202102 (2009)

[7] K. Haruta, and W. J. Spencer, J. Appl. Phys. **37**, 2232 (1966)

[8] I. C. Noyan, P. C. Wang, S. K. Kaldor, and J. L. Jordan-Sweet, Appl. Phys. Lett. **74**, 2352 (1999)

[9] C. E. Murray, I. C. Noyan, P. M. Mooney, B. Lai, and Z. Cai, Appl. Phys. Lett. **83**, 4163 (2003)

[10] P. G. Evans, P. P. Rugheimer, M. G. Lagally, C. H. Lee, A. Lal, Y. Xiao, B. Lai, and Z. Cai, J. Appl. Phys. **97**, 103501 (2005)

[11] C. E. Murray, A. Ying, S. M. Polvino, I. C. Noyan, M. Holt, and J. Maser, J. Appl. Phys. **109**, 083543 (2011)

[12] S. O. Hruszkewycz, M. V. Holt, C. E. Murray, J. Bruley, J. Holt, A. Tripathi, O. G. Shpyrko, I. McNulty, M. J. Highland, and P. H. Fuoss, Nano Lett. 12, 5148 (2012)

[13] M. V. Holt, S. O. Hruszkewycz, C. E. Murray, J. R. Holt, D. M. Paskiewicz, and P. H. Fuoss, Phys. Rev. Lett. **112**, 165502 (2014)

[14] N. Hrauda, J. Zhang, E. Wintersberger, T. Etzelstorfer, B. Mandl, J. Stangl, D. Carbone, V. Holy, V. Jovanovic, C. Biasotto, L. K. Nanver, J. Moers, D. Grutzmacher, and G. Bauer, Nano Lett. **11**, 2875 (2011)

[15] L. K. Nanver, V. Jovanović, C. Biasotto, J. Moers, D. Grützmacher, J. J. Zhang, N. Hrauda, M. Stoffel, F. Pezzoli, O. G. Schmidt, L. Miglio, H. Kosina, A. Marzegalli, G. Vastola, G. Mussler, J. Stangl, G. Bauer, J. van der Cingel, and E. Bonera, Solid State Electron. **60**, 75 (2011)

[16] J. Park, Y. Ahn, J. A. Tilka, K. C. Sampson, D. E. Savage, J. R. Prance, C. B. Simmons, M. G. Lagally, S. N. Coppersmith, M. A. Eriksson, M. V. Holt, and P. G. Evans, APL Mater. **4**, 066102 (2016)

[17] Xiaojing Huang, Michael Wojcik, Nicolas Burdet, Isaac Peterson, Graeme R. Morrison, David J. Vine, Daniel Legnini, Ross Harder, Yong S. Chu, and Ian K. Robinson, Opt. Express, **20**, 24038 (2012)

[18] M. Holt, R. Harder, R. Winarski, and V. Rose, Annu. Rev. Mater. Res. **43**, 183 (2013)

[19] D. Attwood, Soft x ray and extreme ultraviolet radiation: principles and applications (Cambridge Univ. Press, Cambridge, 1999).

[20] M. A. Lutz, R. M. Feenstra, F. K. LeGoues, P. M. Mooney, and J. O. Chu, Appl. Phys. Lett. **66**, 724 (1995)

[21] P. M. Mooney, J. L. Jordan-Sweet, and S. H. Christiansen, Appl. Phys. Lett. **79**, 2363 (2001)

[22] P. G. Evans, D. E. Savage, J. R. Prance, C. B. Simmons, M. G. Lagally, S. N. Coppersmith, M. A. Eriksson, and T. U. Schulli, Adv. Mater. **24**, 5217 (2012)

[23] F. K. LeGoues, P. M. Mooney, and J. O. Chu, Appl. Phys. Lett. **62**, 140 (1993)

[24] D. M. Paskiewicz, D. E. Savage, M. V. Holt, P. G. Evans, and M. G. Lagally, Sci. Rep. **4**, 4218 (2014)

[25] J. A. Tilka, J. Park, Y. Ahn, A. Pateras, K. C. Sampson, D. E. Savage, J. R. Prance, C. B. Simmons, S. N. Coppersmith, M. A. Eriksson, M. G. Lagally, M. V. Holt, and P. G. Evans, J. Appl. Phys. **120**, 015304 (2016)

[26] A. Ying, B. Osting, I. C. Noyan, C. E. Murray, M. Holt, and J. Maser, J. Appl. Cryst. **43**, 587 (2010)

[27] B. D. Cullity, Elements of X-Ray Diffraction (Addison-wesley publishing company, Massachusetts, 1956).

[28] I. V. Markov, Crystal Growth for Beginners: Fundamentals of Nucleation, Crystal Growth, and Epitaxy (World Scientific, Singapore, 1995).

[29] J. A. Floro, S. J. Hearne, J. A. Hunter, P. Kotula, E. Chason, S. C. Seel, and C. V. Thompson, J. Appl. Phys. **89**, 4886 (2001)

[30] E. Chason, B. W. Sheldon, L. B. Freund, J. A. Floro, and S. J. Hearne, Phys. Rev. Lett. **88**, 156103 (2002)

[31] I. A. Blech, J. Appl. Phys. **38**, 2913 (1967)

[32] G. Guisbiers, O. V. Overschelde, M. Wautelet, P. Leclère, and R. Lazzaroni, J. Phys. D: Appl. Phys. **40**, 1077 (2007)

Chapter 3: Domain alignment within ferroelectric/dielectric PbTiO₃/SrTiO₃ superlattice nanostructures

3.1 Introduction

This chapter reports the discovery that merging two independent methods for creating nanostructured ferroelectrics, ultrathin ferroelectric/dielectric superlattices (SLs) and nanostruture format, present a new route towards the nanoscale control of ferroelectricity. Patterned SL nanostructures possess a possibility for a new in-plane orientation of domain structures by minimizing the total free energy. The shape, size, and crystallographic orientation of the nanostructure can drastically alter the competition among the different contributions to the total free energy of the system and thus have a significant impact on fiinal ferroelectric domain configurations. The experimetnal study reported in this chapter shows that fabricating nanostructures produces specific orientations of the nanodomain patterns in which the 180° stripe domains observed in ferroelectric/dielectric SLs are aligned parallel to the edges of the nanostructure. Further processes to understand and control ferroelectric polarization may lead to other exotic polarization configurations, and can enable a variety of applications, including data storage, optical devices, and reconfigurable electronics [1-3].

3.1.1 Polarization domains in ferroelectric thin films

The cubic perovskite structure of compounds with the chemical formula ABO_3 has a unit cell in which consist of A cations at the (0, 0, 0) corners, B cations (0.5, 0.5, 0.5) body center, and anions (O) at (0.5, 0.5, 0), (0.5, 0.5, 0), and (0.5, 0.5, 0). $SrTiO_3$ (STO), for example, has this cubic structure. Small atomic displacements of the cations relative to anions result in distortion of the unit cell and lead to a ferroelectric polarization with a non-zero net dipole moment. $PbTiO_3$ (PTO) in its tetragonal phase at a temperature below its Curie temperature has displacements of the Ti

and O atoms that lead to a tetragonal distortion of the unit cell and produce a large net electric dipole moment. The distortion of the unit cell and the electrostatic effects associated with the electric dipole are the key phenomena underpinning the formation and patterning of ferroelectric domain structures [4].

The creation of surfaces or interfaces can lead to discontinuities in the structure and polarization. The change in the magnitude of the polarization leads the creation of a large interfacial charge density, termed a bound charge [5]. The bound charge in turn induces an electrostatic potential distribution, a so-called depolarization field. The depolarization field increases the total free energy of the ferroelectric thin films by increasing the electrostatic energy [6]. The free energy can be reduced by lowering the depolarization field through the formation of a ferroelectric domain pattern in which the polarization alternate in direction [7]. A pattern of 180° ferroelectric striped domains forms in few-nm PTO thin films grown on STO substrates [4]. The formation of ferroelectric domains, however, leads to the formation of domain walls and the domain size is determined by a trade-off between the electrostatic and domain wall energies [7].

3.1.2 Manipulation of domains using mechanical stress and size effects

The polarization and domain configuration within ferroelectrics can be manipulated by externally applied stresses using a strained buffer layer, a mechanical load, or lattice-mismatched substrates [8-12]. The properties can include the ferroelectric transition temperatures and preferred directions of domain walls. A mechanical load that bends the thin film can introduce a higher density of domain walls in PTO thin films [9]. Controlling strain and electrostatic boundary conditions by choosing various substrates can eliminate unfavorable ferroelastic variants in $BiFeO_3$ (BFO) thin films resulting in domain wall alignments [10-12]. Subtle properties associated with the response of domains to applied fields can also be modified by applied stresses. For

example, the domain wall velocity increases in $PbZr_{0.2}Ti_{0.8}O_3$ thin films as a function of biaxial strain [8].

A variety of phenomena influenced by size effects arise in nanostructured ferroelectric materials. Examples of ferroelectric nanomaterials include crystalline epitaxial islands [13], composites incorporating nanoscale ferroelectric crystallites [14,15], ferroelectric layers with nanoscale thickness [16]. The ferroelectric domain configurations are influenced by the structural distortion when creating nanostructures, for example, in BFO nanostructures the domain configuration depend on the out-of-plane lattice strain and can be changed after a mechanical milling process elastically releases the substrate-imposed stress [17]. The nanoscale polarization configurations also depend on the boundary conditions imposed by the shapes of nanostructures [18]. In elongated $BaTiO_3$ nanostructures, polar vector domains aligned along the length direction are accompanied by other polar vector domains parallel to the shorter direction [19].

3.1.3   Formation of ferroelectric/dielectric superlattice nanostructures

Many of the size effects observed in nanostructured ferroelectric also occur in ferroelectric SL thin films in which the individual component layers have few nm thicknesses [4,20,21]. This chapter focuses in particular on materials consisting of alternating ultrathin layers of ferroelectric and dielectric oxides, termed ferroelectric/dielectric superlattices. Ferroelectric/dielectric SLs have domain configurations that differ significantly from those observed in ultrathin ferroelectric thin films with a uniform composition [22-24]. Specifically, striped nanodomains are formed with typical widths of several nanometers [25,26]. The specific value of the width is determined by the balance of domain wall and depolarization energies [23,24,26-30].

3.1.4   Nanodomain configuration in PbTiO₃/SrTiO₃ superlattice nanostructures

PTO/STO ferroelectric/dielectric SLs nanostructures can be defined by using lithographic patterning techniques. A synchrotron x-ray nanobeam diffraction study of the SL nanostructures that there is an anisotropy in the intensity distribution of the x-ray diffuse scattering produced by the domain pattern. The angular distribution of X-ray diffuse scattering intensity from nanodomains indicates that domains are aligned within an angular range of approximately 20° with respect to the edges of the nanostructure.

A computational investigation of the energetics of the polarization patterns calculated using Landau–Ginzburg–Devonshire (LGD) theory indicates that domain wall orientation parallel to the edges of the structure yields elastic distortions that allow for the greater magnitude of the remnant polarization than other domain orientations. The greater magnitude polarization in the domains with the parallel orientation to the nanostructure edges can minimize the total energy of the system by lowering of bulk and electrostrictive contributions to the total free energy.

As described below, the x-ray study also provides results that can be used to test alternative hypotheses for the origin of the alignment effects. The nanodiffraction experiments show that the fabrication process mechanically distorts the SL nanostructure to a samll extent. A range of applied stresses corresponding to this distortion was included in the computational model to understand the possible role of this strain in the domain alignment. A study of the free energies of the competing domain configurations as a function of the applied stress shows that the observed configuration was favorable under all stresses. Similarly, the domain wall alignment with the geometrical features of the nanostructure was robust for the experimental widths of nanostructures considered.

3.2   Experimental setup

3.2.1   Fabrication of PbTiO₃/SrTiO₃ superlattice nanostructures

The SL thin film consisting of alternating PTO and STO layers were deposited using off-axis radio-frequency sputtering with a repeating unit of 7 unit cells of PTO and 3 unit cells of STO. This composite unit was repeated 25 times to attain a 100-nm thick SL thin film deposited on a SrRuO₃ (SRO) thin film on a (001)-oriented STO substrate. The deposition, structural characterization, and equilibrium domain pattern in the materials have been previously described [25,27,31]. As shown in Figure 3-1(a), the SL nanostructures were fabricated using focused-ion-beam (FIB) milling lithography. In order to protect the SL from ion-induced damage, a double layered cap was deposited before the Ga-ion milling process. The dimensions of the area covered by the protective cap were approximately 3 µm × 2 µm, extending beyond the area that was eventually milled during the FIB process. The bottom layer of the protective cap consisted of a 130 nm-thick Pt layer deposited by electron-beam-induced deposition. The top layer of the cap consisted of a 230 nm-thick layer of carbon produced by Ga-ion-induced deposition.

The nanostructures were fabricated by milling regions to mechanically decouple them from the surrounding area of SL thin film. Within the milled regions, the cap, SL, and underlying substrate were removed to a depth of 3 µm. The milling was conducted using a Ga-ion accelerating potential of 30 kV and current of 50 pA in a large number of passes of the beam over each area to be removed. Figure 3-1(b) shows a scanning electron microscopy (SEM) image of a SL nanostructure with width W = 800 nm and length L = 2 µm. The analysis employs a Cartesian coordinate system in which the long direction of the nanostructures is parallel to the *x*-axis and the *z*-axis is along the substrate surface normal. A previous study of submicron thick STO sheets has

shown that the FIB milling process induces bending of the STO crystals, but does not introduce extended defects [32].

3.2.2 X-ray nanodiffraction
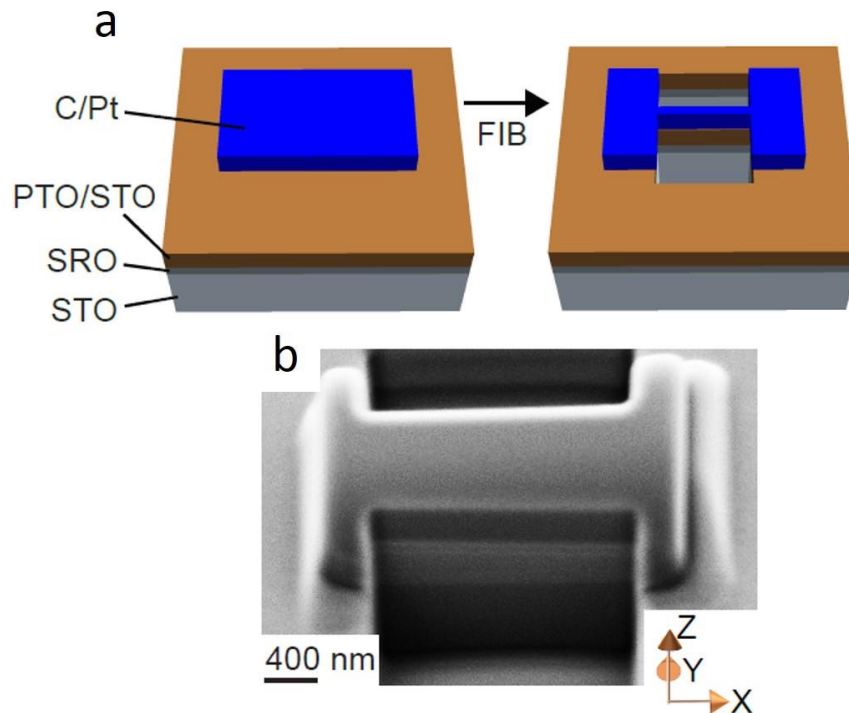
Figure 3-1: (a) Schematic of nanostructure fabrication. (b) SEM image of an 800 nm-wide PTO/STO SL nanostructure created using FIB lithography. The protective cap appears as a raised region covering the ridge-shaped nanostructure. The cap also extends slightly into the region beyond the unpatterned area of the SL at each edge of the nanostructure.

The changes in the SL lattice and domain structures were studied using synchrotron X-ray nanobeam diffraction at station 26-ID-C of the Advanced Photon Source of the Argonne National Laboratory. An X-ray beam with a photon energy of 9 keV was focused to a spot size of 50 nm full-width-at-half maximum using a 160 µm-diameter Fresnel zone plate. A 60 µm-diameter center stop and an order sorting aperture were used to attenuate the unfocused beam and X-rays focused to higher orders. The convergence of the focused X-ray nanobeam was 0.26° at the focal spot. The thickness of the SL is less than its absorption length [33], so the focused X-ray nanobeam can

penetrate the entire SL thickness, thereby providing information about SL lattice distortion and its nanoscale domain structures [34]. The x-ray diffraction patterns were collected using a charge coupled device detector consisting of a 1024×1024 array of 13 μm square pixels.
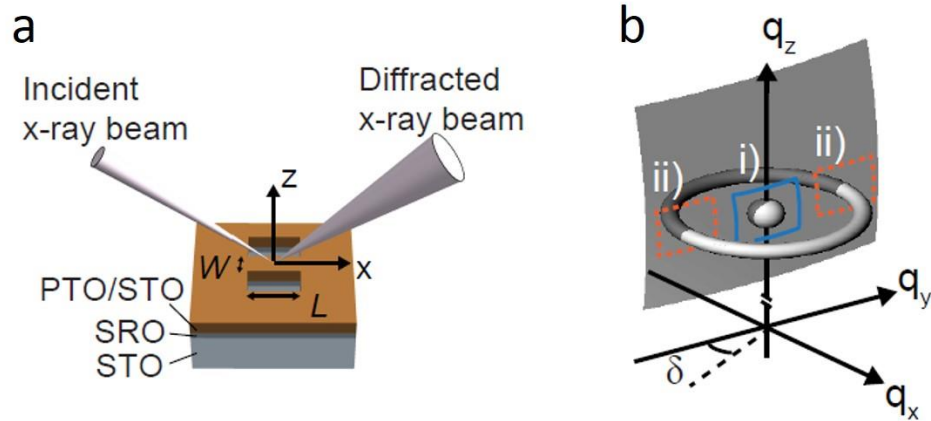
Figure 3-2: (a) X-ray nanodiffraction geometry including the PTO/STO SL thin film heterostructure, underlying SRO layer, and STO substrate. (b) Geometry of reciprocal space near the 002 X-ray reflection of the PTO/STO SL. When the diffraction experiment matches the Bragg condition for the SL, at $\Delta\theta = 0$, the Ewald sphere (dark gray) intersects (i) Bragg reflection and (ii) the ring of domain diffuse scattering. At other values of $\Delta\theta$ the Ewald sphere intersects the ring of domain diffuse scattering at a different value of δ.

As illustrated in Figure 3-2(a), the elongated SL nanostructure was placed such that the focused X-ray nanobeam propagated parallel to the length direction of the nanostructure on the *x–z* plane. The benefit of this X-ray geometry is that the focused X-ray nanobeam travels along the length direction of the nanostructure, allowing the variation of structural and ferroelectric properties across the width of the nanostructure to be studied. The incident angle of the X-ray beam was fixed near the 0_{th} order Bragg angle of the 002 PTO/STO SL Bragg reflection, corresponding to the average crystallographic d-spacing of the SL. The Bragg angle for this reflection was $\theta_B = 20.11°$, with the out-of-plane wavevector q_z of 3.14 Å^{-1} [35]. A distribution of diffuse x-ray scattering intensity arises in reciprocal space due to scattering from the striped
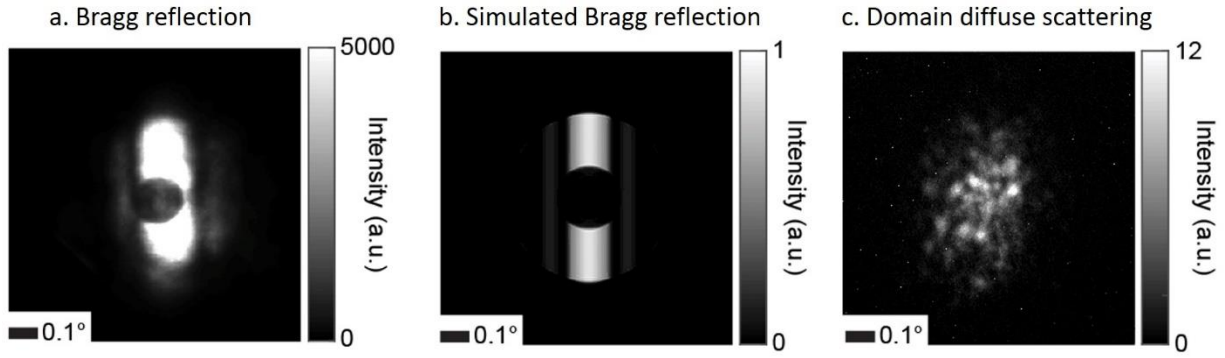
Figure 3-3: Detector images of diffraction patterns of (a) SL Bragg reflection, (b) simulated SL Bragg reflection, and (c) domain diffuse scattering acquired at the Bragg condition. The 2θ diffraction angle is in the horizontal direction in the diffraction patterns in this figure.

nanodomains. In the unpatterned region of the PTO/STO SL the diffuse scattering intensity is nearly uniformly distributed around a ring with a reciprocal-space radius of $0.097\ \text{Å}^{-1}$ [4,21,25,30]. This radius corresponds to a real-space stripe nanodomain period Λ of 6.5 nm.

Figure 3-2(b) shows the geometry of reciprocal space near the 002 Bragg reflection of the PTO/STO SL. The diffuse scattering intensity from the unpatterned region of the film is distributed as a uniform ring in the q_x–q_y plane, which is schematically shown as a toroid in Figure 3-2(b). The details are discussed in Chapter 3.4.1. At the Bragg condition, the Ewald sphere intersects (i) the Bragg reflection and (ii) the ring of domain diffuse scattering.

Images of the two-dimensional diffraction patterns are shown in Figure 3-3. The horizontal axis of the images is the $\Delta 2\theta$ direction associated with the conventional 2θ scattering angle. The diffraction patterns contain the reciprocal information over a range $\Delta q_z = 0.039\ \text{Å}^{-1}$ corresponding to the convergence of the focused X-ray beam.

Figure 3-3(a) shows the diffraction pattern of the SL 002 Bragg reflection. The SL Bragg reflection has an angular width along the $\Delta 2\theta$ direction that is inversely proportional to the total thickness of the SL. The simulated intensity distribution at this Bragg reflection, shown in Figure

3-3(b), was generated using a nanobeam simulator [36,37]. This simulation simulates the coherent x-ray nanodiffraction pattern acquired using a monochromatic focused x-ray beam and allows the simulation of multilayer heterostructures [37,38].

The domain diffuse scattering appears in the diffraction pattern shown in Figure 3-3(c). The diffuse scattering intensity is distributed in a speckle pattern, an uneven distribution of intensity in narrow "speckles". Speckle patterns are commonly observed in diffuse scattering of coherent x-rays from disordered systems. The observation of a speckle pattern in the domain diffuse scattering indicates that the striped nanodomain pattern is highly random. A similar observation has also been reported for PTO/STO superlattices probed with coherent x-ray beams focused to much larger sizes [39].

3.3 Elastic lattice distortion in PbTiO$_3$/SrTiO$_3$ superlattice nanostructures

FIB lithography often results in the introduction of defects and other sources of stress that distort nanostructures [40]. The FIB milling process was thus expected to distort the SL nanostructures. The X-ray nanobeam diffraction study reveals that the SL nanostructures are elastically distorted. The distortion leads to a position-dependent angular shift of the SL Bragg reflection on the detector plane along a direction perpendicular to the X-ray beam footprint direction by an angle $\Delta\chi$ due to the local tilting of the lattice planes by an angle $\Delta\alpha$. The tilting of the lattice planes ($\Delta\alpha$) can be determined by measuring the angular shift of the diffraction patterns on the detector using the relationship $\Delta\alpha = \Delta\chi/2\sin(\theta_B)$. A similar approach was used to determine the tilting of lattice planes in the Si/SiGe heterostructure described in Chapter 2. The derivation of the details relationship between $\Delta\alpha$ and $\Delta\chi$ and other details the X-ray analysis of the tilts are discussed in Chapter 2. A plan-view SEM image of the 800-nm-width nanostructure and a map of $\Delta\alpha$ for its crystal lattice are shown in Figures 3-4(a) and Figures 3-4(b), respectively. The maps of

the tilt indicate that the lattice is rotated by up to 0.07° with respect to the average orientation. The lattice tilt resulting from the elastic distortion is shown as a surface plot in Figure 3-4(c), illustrating the local curvature of the SL nanostructure.
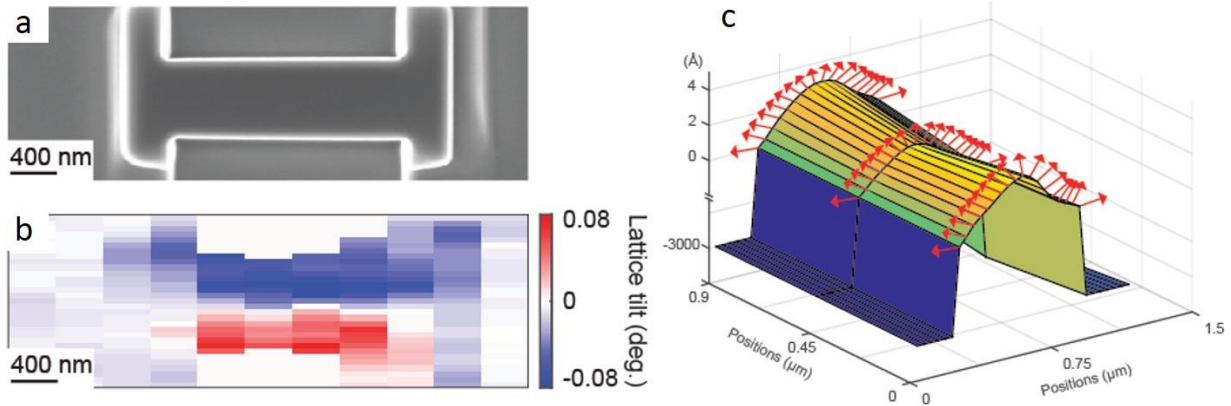
Figure 3-4: (a) SEM image of an 800 nm-wide SL nanostructure, and (b) its crystal lattice tilt with (c) Schematic of a curved lattice resulting from the lattice tilt with its estimated magnitude of curvature calculated using the derivation of the lattice tilt angles. The red arrows indicate the surface normal directions.

3.3.1 Determining the strain in the nanostructure from its curvature

The magnitude of the curvature was measured by computing the numerical derivative of the lattice tilt angles with respect to the measured positions [41]. The curved shape of nanostructure imposes a strain in the SL nanostructure, with the largest magnitude along the in-plane direction.

Figure 3-5 shows a plot of the structural relaxation in the nanostructure. The average in-plane structural relaxation is defined as $\frac{1}{t}\int_0^t \frac{D}{R}dD = \frac{t}{2R}$, where t is the film thickness, and D is a variable spanning the film thickness. In the nanostructure, however, the curvature reaches up to 5880 m^{-1}. This corresponds to a radius of curvature R of 0.17 mm based on the assumption that the relaxation arises only from the bending of the SL. The average in-plane relaxation for the curved SL nanostructure shown in Figure 3-5 is 0.03%. The unpatterned regions away from the SL nanostructure in Figure 3-5 show no systematic variation structural relaxation.

Figure 3-5: In-plane structural relaxation computed under the assumption that the strain arises only from bending of the nanoscale sheet.

3.3.2 Out-of-plane strain measurement using x-ray nanodiffraction

A second estimate of the changes in lattice of the PTO/STO nanostructure can be obtained by analyzing the difference between the diffraction patterns of the SL nanostructure and unpatterned regions. Here we consider only the shift of the diffraction pattern along the $\Delta 2\theta$ direction, perpendicular to $\Delta\chi$ direction. Analyzing the shift of Bragg reflection along the $\Delta 2\theta$ direction provides an estimate of the out-of-plane strain. An area near a 500 nm-wide SL nanostructure was scanned using the focused X-ray nanobeam. The 002 SL Bragg reflections appears on the detector whenever the (002) planes of the SL meet the Bragg condition. This condition is relatively easy to achieve because of the large angular range spanned by the convergence of the focused X-ray nanobeam.

Figure 3-6 shows a set of diffraction patterns acquired at different positions along the length of the 500-nm-wide nanostructure, following the path indicated by the green line. All the diffraction patterns were acquired at a nominal X-ray incident angle 0.03° less than the Bragg angle of the unpatterned regions. The diffraction patterns numbered 1, 2, 3, 4, 9, 10, 11, and 12 in Figure 3-6 were acquired outside of the nanostructure and diffraction patterns 5, 6, 7, and 8 were acquired within the nanostructure. Note that the *2θ* direction is vertical in the diffraction patterns in Figure 3-6. The *2θ* angles of the PTO/STO 002 Bragg reflection in each diffraction pattern image were measured using the centroid calculation of the intensity distribution along the *Δ2θ*

direction. The Bragg reflections within the nanostructure appear at a value of *2θ* that is 0.017°

larger than in the diffraction patterns acquired outside of the nanostructure. This angular difference

(Δ) arises because the out-of-plane lattice parameter within the nanostructure is smaller than for

the unpatterned region. The angular difference can be used to calculate the out-of-plane strain

using the relationship $\varepsilon_z = -\cot(\theta_B) \Delta$, which leads to $\varepsilon_z = -0.08$ %.

The in-plane relaxation can be found from the value of ε_z measured in Figure 3-6. The

relationship between the in-plane strain ε_x and the out-of-plane strain ε_z is $\varepsilon_x = \varepsilon_z (v - 1)/v$ [42,43].

Here v is the Poisson ratio. The value of $v = 0.3125$ for the PTO [44,45] is used here, assuming the

mechanical properties of the PTO/STO SL are similar to those of PTO. The strain in-plane *x*-

direction is thus $\varepsilon_x = 0.18\%$.

The strain observed in the PTO/STO SLs has a similar magnitude to the strain observed in

STO sheets formed using FIB [32]. The strain observed here is slightly less than what has been

recently reported in Si or Au nanocrystals exposed to FIB, because the top of the SL is protected
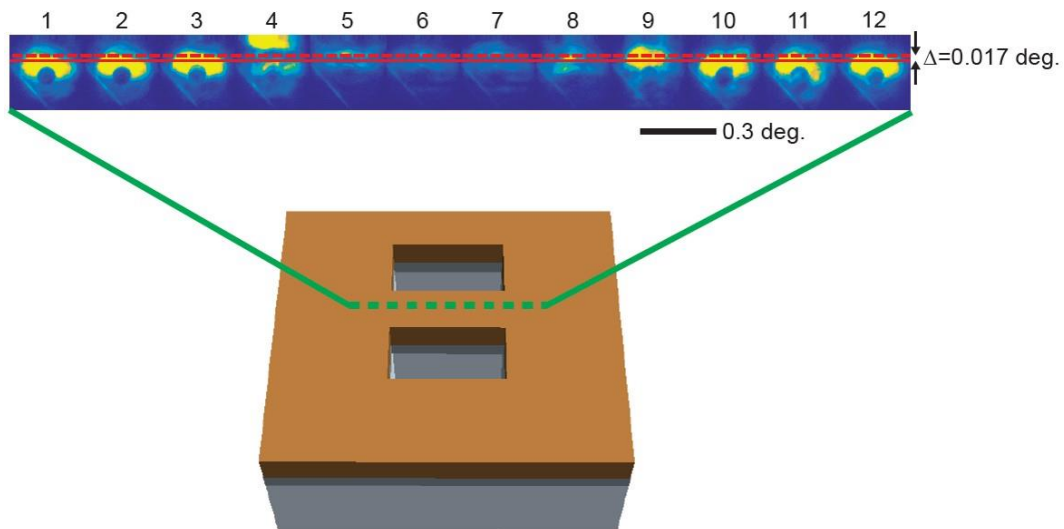
Figure 3-6: Diffraction patterns acquired along the length of a 500-nm-width nanostructure. The X-ray beam was scanned along the path indicated by the green dotted line. The diffraction patterns are shifted on the detector plane, and the angular difference (Δ) arises because the out-of-plane lattice parameter within the nanostructure. The 2θ diffraction angle is in the vertical direction in the diffraction patterns in this figure.

with a capping layer and is not directly milled [40,46,47]. The observed in-plane relaxation provides an important parameter for demonstrating the validity of the computational results described below.

3.4   Models of nanodomain alignment

3.4.1   Measuring the azimuthal domain distribution

It is useful to define two different limiting cases of the domain configuration in order to simplify the discussion of the nanodomain directions within the nanostructures. Two distinct stripe nanodomain configurations with different domain-wall orientations, termed "perpendicular" and "parallel" are shown in Figure 3-7. The orientations of the domain walls are aligned either perpendicular or parallel relative to the edges of the nanostructures. As illustrated in the diagram of reciprocal space shown in Figure 3-2(b), the azimuthal angle δ is defined with respect to the y-axis to describe the orientation of domains relative to the SL nanostructure length direction. The same definition the angle δ is illustrated in real space Figure 3-7(c) with respect to the stripe nanodomain orientation. The perpendicular and parallel configurations have $\delta = 90°$ and $\delta = 0°$, respectively. In order to describe the orientation of stripe nanodomain with respect to the SL nanostructure, a position-dependent unit vector n is defined as the local normal vector to the planes of the domain walls at all positions. The in-plane orientation of n at each position is described by a corresponding δ angle, as illustrated in Figure 3-7(c).

The domain diffuse scattering intensity forms in a ring in reciprocal space, in a q_x-q_y plane with a radius of $2\pi/\Lambda$, where Λ is the real-space domain period. In cases of a non-uniform distribution of the orientations of the domain walls, there is also a non-uniform distribution of the domain diffuse scattering intensity around the ring. Figure 3-8 shows sections of reciprocal space in the q_x-q_y and q_x-q_z planes passing through the 002 SL Bragg reflection and the ring of domain
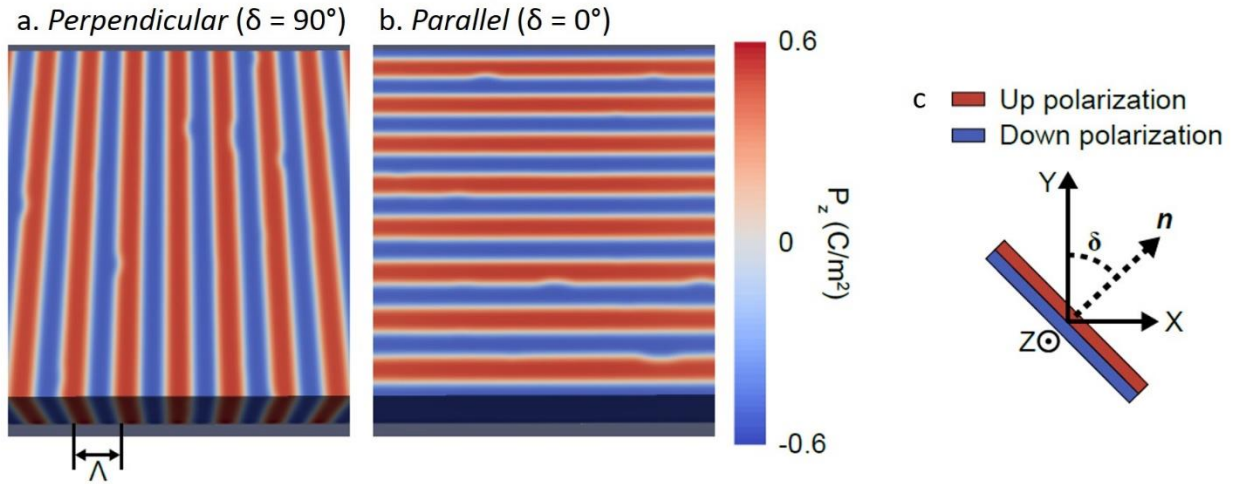
Figure 3-7: Diagrams of the polarization within SL nanostructures in (a) perpendicular (δ = 90°) and (b) parallel (δ = 0°) domain configurations. (c) Definitions of the parameters used to describe the domain wall orientation: the local domain-wall in-plane normal (n) and azimuthal angle (δ) with respect to the y-axis.

diffuse scattering intensity (yellow). The 002 SL Bragg reflection is at $q_x = q_y = 0$, and $q_z = z_0$, but

is not shown. Figure 3-8(a) and Figure 3-8(c) show Ewald sphere intersecting the ring of domain

diffuse scattering intensity in which the incident X-ray beam meets the 002 SL Bragg condition.

In this case, the slice of domain diffuse scattering intensity appears on the detector plane. Other

sections of the ring of domain diffuse scattering intensity can also be obtained by rotating the

sample by and angle $\Delta\theta$. This rotation of the sample corresponds to changing the x-ray incident

angle and rotating reciprocal space with respect to the Ewald sphere. Figure 3-8(b) shows the

corresponding new section of domain diffuse scattering intensity resulting from the displacement

of the Ewald sphere along the q_x axis Δx. In terms of the incident angles the magnitude of Δx is:

$$\Delta x = r\ (cos\theta_1 - \ cos\theta_2)$$

Equation 3-1

The angles $\theta_1 = \theta_1 + \Delta\theta$, and θ_2 are defined in Figure 3-8(d). The azimuthal angle $\boldsymbol{\delta}$ angle at which

the Ewald sphere intercepts the domain diffuse scattering can be determined using the relationship:

$$\theta_2 = sin^{-1}\frac{z_2}{r} = sin^{-1}\frac{z_0 - z_1}{r} = sin^{-1}(2sin\theta_B - sin\theta_1)$$

Equation 3-2

Which gives:

$$\delta = sin^{-1}\frac{\Delta x}{2\pi/\lambda} = \frac{\Lambda}{\lambda}(cos(sin^{-1}(2sin\theta_B - sin\theta_1) - cos\theta_1))$$

Equation 3-3

By using the trigonometric identity $cos(sin^{-1}(\alpha)) = \sqrt{1 - \alpha^2}$ the expression for δ angle can be simplified to:

$$\delta(\Delta\theta) = \frac{\Lambda}{\lambda}\left(\sqrt{1 - (2sin\theta_B - sin(\theta_B + \Delta\theta))^2} - cos(\theta_B + \Delta\theta)\right)$$

Equation 3-4

Here λ is the wavelength of the x-rays.

The maximum value of $\Delta\theta$ at which the Ewald sphere can geometrically intersect the ring of domain diffuse scattering is 1.77°. For magnitudes of $\Delta\theta$ less than approximately 1°, a target in this study, $\delta(\Delta\theta) \approx \frac{2\Lambda\,\Delta\theta\,sin\theta_B}{\lambda}$, or approximately $\delta(\Delta\theta) = 32.4\,\Delta\theta$.
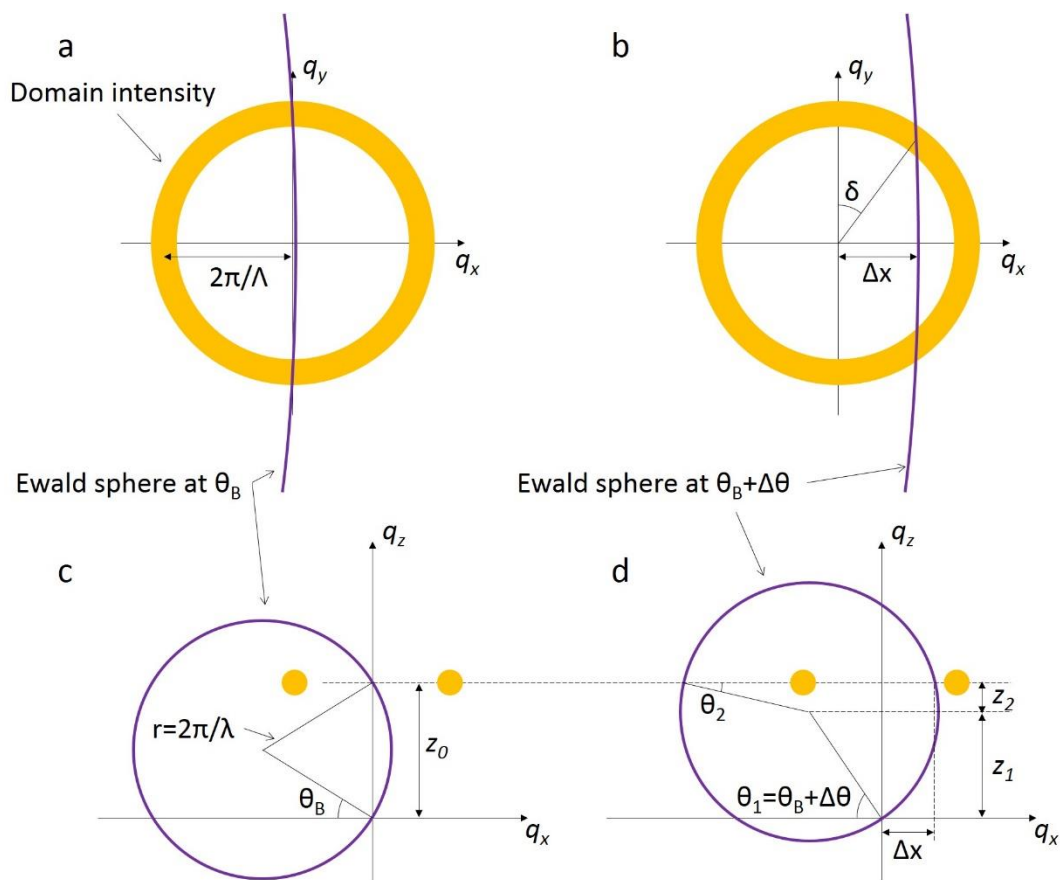
Figure 3-8: Reciprocal space maps with Ewald sphere (purple) and the domain intensity (yellow). The superlattice Bragg peak is not shown. The corresponding x-ray incident angles are (a, c) θ_B and (b, d) $\theta_B + \Delta\theta$

3.4.2 Domain intensity enhancement in nanostructure at small δ

The domain diffuse scattering intensity measured at each value of δ arises from the population of striped nanodomains with matching directions of the in-plane real-space domain orientation. Figure 3-9(a) shows a plan view of an example of the striped nanodomain patterns in real space. The striped nanodomain patterns comprise the lateral repetitions of up and down polarizations.

The orientation of the domain patterns is disordered in the regions far from the SL nanostructures. In this region, the Fourier transform of the real space domain patterns would generate a ring shape with a uniform intensity distribution in reciprocal space, as shown in Figure 3-9(b). A model of the aligned domain pattern in real space and the corresponding Fourier transform intensity are shown in Figure 3-9(c) and Figure 3-9(d). In the model of the aligned domains the domain period is set to be the same as in Figure 3-9(a), but the domain walls are approximately aligned with the normal vector n along the y axis. Accordingly, the domain diffuse scattering intensity in reciprocal space is more intense at two locations along the q_y direction. With
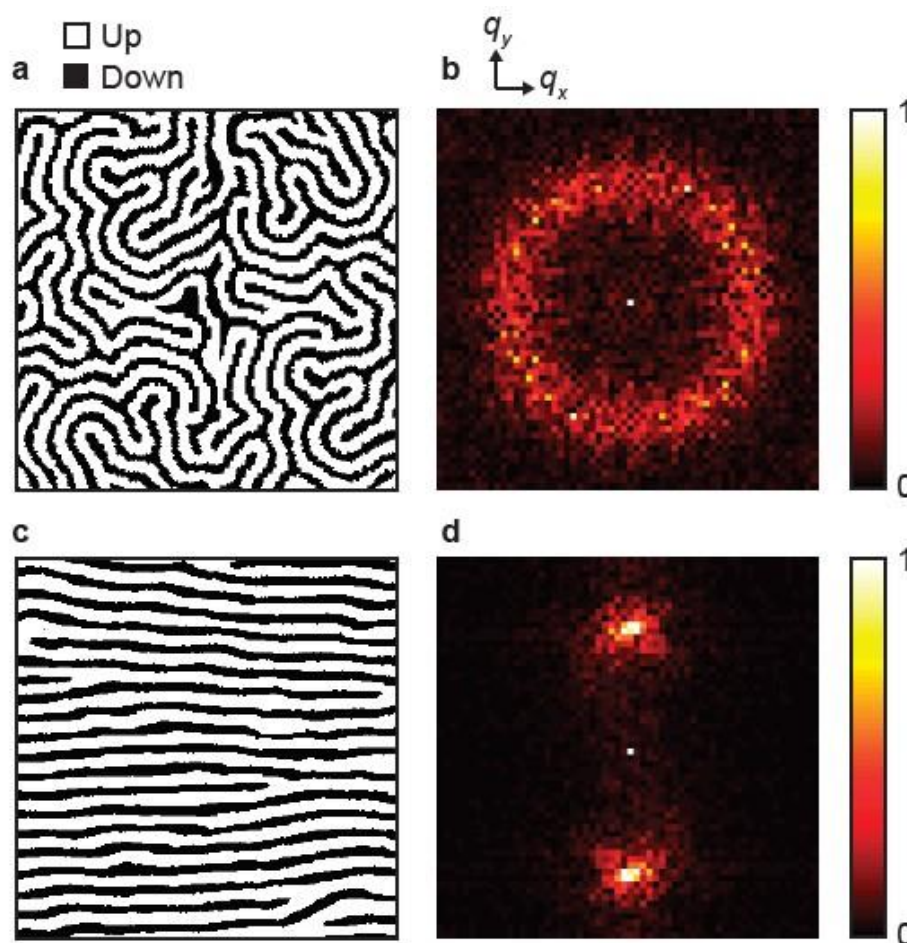
Figure 3-9: Plan view of models for ferroelectric stripe domain patterns in real space with up (white) and down (black) polarizations with (a) disordered and (c) aligned domain patterns. The domain period is defined as the distance covering both up and down polarizations. (b, d) Fourier transform intensity of (a) and (c) in reciprocal space arising from the lateral repetition of the domain period.

the aligned domain pattern, there are thus several locations in reciprocal space where the domain diffuse scattering intensity is higher than in the disordered case. This effect is apparent in the Fourier transforms of the disordered and ordered cases shown in Figure 3-9(b) and Figure 3-9(d). The anisotropy of scattered intensity around the ring of domain diffuse scattering has been previously observed in ordered magnetic striped domain systems [48].The domain diffuse scattering intensity at small values of δ angle will reduced perpendicular to the mechanically milled edges of the SL nanostructure, and increased when the domain walls are parallel to the edges.
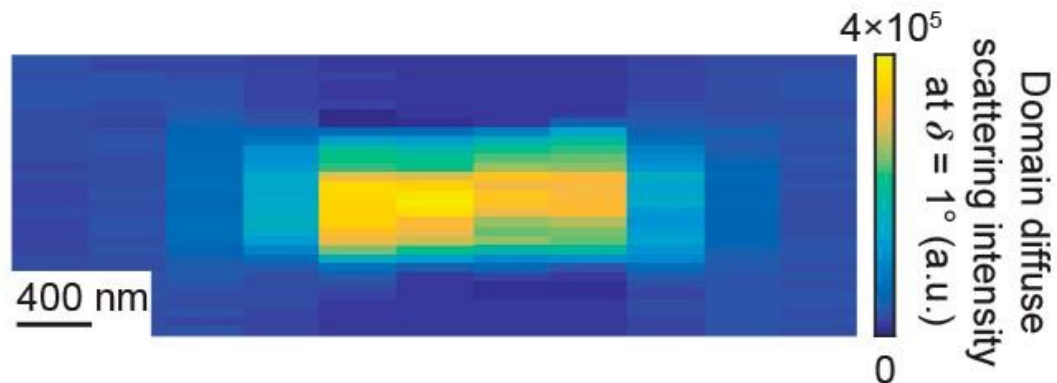
Figure 3-10: Map of domain diffuse scattering intensity acquired at Δθ = 0.03°, corresponding to δ = 1° in the area shown in (c). The intensity within the nanostructure is higher than that in the unpatterned region by a factor of 7.

The experimental study of the domain diffuse scattering shows that fabrication of the nanostructure induces anisotropy in the distribution of domain diffuse scattering. An experiment was conducted in which the domain diffuse scattering intensity was collected at several values of the incident angle to measure the changes in domain intensity at multiple values of the angle δ. The domain diffuse scattering intensity from the nanostructure was first collected at $\delta(\Delta\theta = 0.03°)$ = 1°. A map of the domain diffuse scattering intensity as a function of position within and near the SL nanostructure is shown in Figure 3-10. The domain intensity is a factor of 7 more in intensity

in the nanostructure than in the unpatterned region. The local enhancement of the diffuse scattering indicates that domain walls in the SL nanostructure are aligned with the edges of the structure.

Figure 3-10 also shows regions with relatively low domain diffuse scattering intensity near the edges of the nanostructure. These regions of low intensity arise from artifacts in the X-ray imaging due to a combination of a slight defocus (and thus larger spots size) of the X-ray beam and an azimuthal misalignment of the focused X-ray nanobeam footprint with the long axis of the nanostructure.

Further information about the azimuthal distribution of domain diffuse scattering intensity was obtained by comparing the domain diffuse scattering intensities measured at $\Delta\theta = 0.03°$ with a second set of intensities measured at $\Delta\theta = 0.25°$. The two incident angles correspond to $\delta = 1°$ and $8°$. The azimuthal dependence of the domain diffuse scattering intensities for SL nanostructures with widths of 500 nm and 800 nm are plotted in Figure 3-11, along with the intensities acquired at the same angles in unpatterned regions. The intensities are plotted on a scale
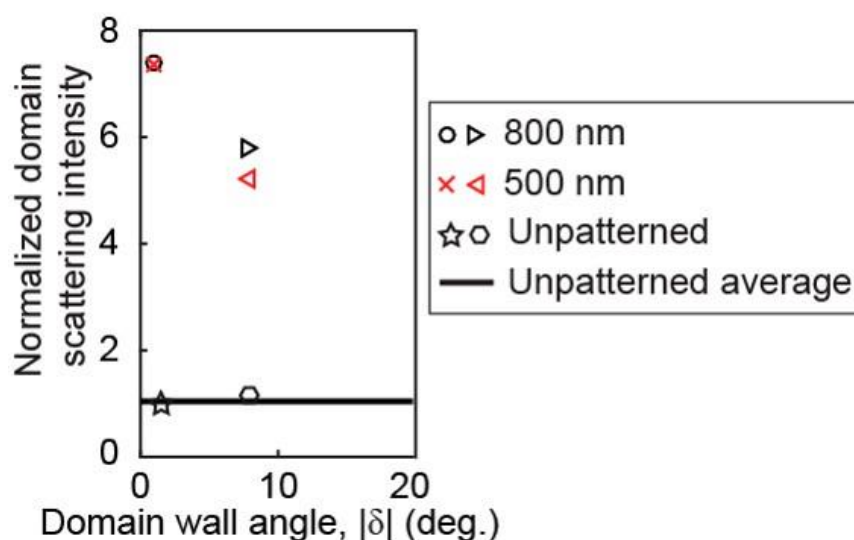
Figure 3-11: Normalized domain diffuse scattering intensities as a function of azimuthal angle δ. Domain scattering intensities were measured in unpatterned regions and in 500 nm- and 800 nm-wide SL nanostructures at domain normal angles δ = 1° and 8°.

normalized by the average intensity of the measurements at the two orientations in the unpatterned region. On this scale, the normalized intensity of the unpatterned regions is close to 1. The domain diffuse scattering intensities in SL nanostructures are high at a low δ angle, as expected based on the map shown in Figure 3-10, and are lower at the larger δ angle.

The conclusion drawn from Figure 3-10 is that the domain walls are preferentially aligned along the mechanical edges of the nanostructures. Assuming that the distribution of domain wall directions is symmetric about $\delta = 0$, a fit of a normal distribution of domain wall orientations gives a full-width at half-maximum of 20°. This angular width indicates that the domain walls are parallel to the long edge of the nanostructure with deviations in their orientations of approximately ±10°.

The presence of the capping layer makes domain wall imaging by piezoelectric force microscopy (PFM) impossible because the electrical contact between a probe tip and the ferroelectric is interrupted. Similarly, the formation of the thin sections of the SL that required for transmission electron microscopy could potentially perturb the original conditions leading to domain alignment. Thus, neither of these two techniques were employed for probing the obtained domain wall configurations.

3.5 Other possible artifacts for domain intensity enhancement in nanostructures

This section considers three artifacts that could lead to the enhanced domain diffuse scattering intensity observed in the SL nanostructures without domain alignment. First, an increase in the total number of domain walls within the region illuminated by the X-ray beam, corresponding to a decrease in domain period, could lead to increased domain diffuse scattering. A comparison of the domain diffuse scattering from patterned and unpatterned regions shows that

the domain period in SL nanostructures is 3% smaller than the unpatterned region. This would produce a 6% increase in intensity within the nanostructures because the X-ray diffuse intensity is proportional to the square of the total number of domain walls [23,29]. The expected intensity change due to the domain period is thus much smaller than the measured intensity difference between patterned and unpatterned areas.

A second possible artifact is related to the possibility that SL nanostructures have reduced domain wall width and thus higher X-ray scattering in comparison with the unpatterned region. This possibility can be evaluated using the domain diffuse scattering intensities derived as a function of domain-wall width [49]. Assuming the domain wall width is zero in the SL nanostructure, the observed intensity enhancement occurs only when the domain wall width reaches 16 nm in the unpatterned region, which is an impractically large value that is larger than the domain period [50,51].

One last artifact would arise if the areas occupied by up and down polarizations within the nanodomain period were different in the SL nanostructure than in the unpatterned region. The intensity of the diffuse scattering depends on the up-down domain fraction and reaches a maximum with equal populations of up and down polarizations [23,29]. An up-polarization fraction $p_{up} = 0.5$ in the SL nanostructure and $p_{up} = 0.1$ in the unpatterned region would lead to the observed intensity enhancement. The change in up-down polarization fraction, however, is unreasonable because $p_{up} = 0.5$ is expected in the unpatterned region, as observed in previous studies of PTO/STO SLs grown on STO substrates [26]. Therefore, none of these artifacts accounts for the observed intensity enhancement.

3.6 Thermodynamic models of domain alignment

A computational study using a phase-field method was conducted by Dr. John Mangeri and Prof. Serge Nakhmanson of the University of Connecticut to evaluate the total free energies of different domain wall arrangements in the SL nanostructures. A range of computational methods, including density functional theory and phase field modeling, can be used to predict the polarization configuration of nanoscale ferroelectrics [18,26,52,53]. Dr. Mangeri and Prof. Nakhmanson have developed methods allowing precise simulations of ferroelectric nanostructures employing phase field modeling [54,55]. This section describes the output of the discussion between myself and Dr. Mangeri and Prof. Nakhmanson regarding the physical assumptions underpinning the thermodynamic model and summarizes a series of studies that reveal how the edges of the nanostructure favor the parallel domain configuration.

3.6.1 Landau-Ginzburg-Devonshire free energy calculation

Previous studies have shown that the STO layers are strongly polarized [20,56] when the PTO component dominates the SL repeating unit [31,57]. In this case, there is a with a nearly constant polarization with a magnitude less than the equilibrium PTO polarization [31,57]. Once the STO layers are polarized, the polarization is approximately continuous through the entire PTO/STO repeating unit. In order to simplify the simulations, the model configuration adopted a uniform ferroelectric material of PTO to represent the SL.

The total free energy of the PTO F_{total} is the sum of the bulk, electrostatic, domain wall formation, elastic, and coupled energy contributions:

$$F_{total} = \int f \, dxdydz = \int \left[f_{bulk} + f_{domain\_wall} + f_{electrostatic} + f_{elastic} + f_{coupled} \right] dxdydz$$

Equation 3-5

The bulk energy contribution of the Landau free energy density was calculated using a sixth order expansion in the components of the polarization P:

$$f_{bulk} = \alpha_1(T)\left(P_x^2 + P_y^2 + P_z^2\right) + \alpha_{11}\left(P_x^4 + P_y^4 + P_z^4\right) + \alpha_{12}\left(P_x^2 P_y^2 + P_y^2 P_z^2 + P_z^2 P_x^2\right)$$

$$+ \alpha_{111}\left(P_x^6 + P_y^6 + P_z^6\right) + \alpha_{112}\left(P_x^4\left(P_y^2 + P_z^2\right) + P_y^4\left(P_z^2 + P_x^2\right) + P_z^4\left(P_y^2 + P_x^2\right)\right)$$

$$+ \alpha_{123}\left(P_x^2 P_y^2 P_z^2\right)$$

Equation 3-6

Here α_1, α_{11}, α_{12}, α_{111}, α_{112}, and α_{123} are the expansion coefficients, which at room temperature are, -7.1×10^7, -7.3×10^7, 7.5×10^8, 2.6×10^8, 6.1×10^8, -3.7×10^8, and -7.1×10^7 for PTO. The minima of the bulk energy determine the preferred directions and magnitude of the polarization in the unit cell at a given temperature, T. The polarization is non-zero when T is below the Curie temperature, T_c, the phase transition temperature between ferroelectric and paraelectric states.

The domain wall formation energy contribution arises from the local gradient in polarization across the domain wall, defined as:

$$f_{domain\_wall} = \frac{1}{2}G_{11}\left[\left(\frac{\partial P_x}{\partial x}\right)^2 + \left(\frac{\partial P_y}{\partial y}\right)^2 + \left(\frac{\partial P_z}{\partial z}\right)^2\right] + G_{12}\left[\frac{\partial P_x}{\partial x}\frac{\partial P_y}{\partial y} + \frac{\partial P_y}{\partial y}\frac{\partial P_z}{\partial z} + \frac{\partial P_z}{\partial z}\frac{\partial P_x}{\partial x}\right]$$

$$+ \frac{1}{2}G_{44}\left[\left(\frac{\partial P_x}{\partial y} + \frac{\partial P_y}{\partial x}\right)^2 + \left(\frac{\partial P_y}{\partial z} + \frac{\partial P_z}{\partial y}\right)^2 + \left(\frac{\partial P_z}{\partial x} + \frac{\partial P_x}{\partial z}\right)^2\right]$$

$$+ + \frac{1}{2}G'_{44}\left[\left(\frac{\partial P_x}{\partial y} - \frac{\partial P_y}{\partial x}\right)^2 + \left(\frac{\partial P_y}{\partial z} - \frac{\partial P_z}{\partial y}\right)^2 + \left(\frac{\partial P_z}{\partial x} - \frac{\partial P_x}{\partial z}\right)^2\right]$$

Equation 3-7

Here G_{11}, G_{12}, G_{44}, and G'_{44} are the gradient energy coefficients, and have values of 0.6 G_{110}, 0, 0.3 G_{110}, and 0.3 G_{110}, respectively, with $G_{110} = 1.73 \times 10^{-10}$ C^{-2}m^{4}N.

The electrostatic energy contribution represents the interaction of the ferroelectric polarization with the internal and external electric fields and is defined as

$$f_{electrostatic} = -\boldsymbol{P} \cdot \nabla \boldsymbol{\Phi}$$

Equation 3-8

Here P is the polarization field and Φ is the electrostatic potential.

The elastic energy contribution to the total energy is:

$$f_{elastic} = \frac{1}{2} C_{ijkl} (\varepsilon_{ij} - \varepsilon_{ij}^0)(\varepsilon_{kl} - \varepsilon_{ij}^0)$$

Equation 3-9

C_{ijkl} is the elastic stiffness tensor with $i, j, k,$ and l being either 1, 2, or 3, and $C_{11} = 281$ Gpa, $C_{12} = 116$ Gpa, and $C_{44} = 97$ Gpa for PTO. ε_{ij}^0 is the strain arising from the polarization [52]:

$$\varepsilon_{11}^0 = Q_{11}P_x^2 + Q_{12}(P_y^2 + P_z^2), \varepsilon_{23}^0 = Q_{44}P_yP_z$$

$$\varepsilon_{22}^0 = Q_{11}P_y^2 + Q_{12}(P_z^2 + P_x^2), \varepsilon_{13}^0 = Q_{44}P_zP_x$$

$$\varepsilon_{33}^0 = Q_{11}P_z^2 + Q_{12}(P_x^2 + P_y^2), \varepsilon_{12}^0 = Q_{44}P_xP_y$$

Equation 3-10

Q_{11}, Q_{12}, and Q_{44} are the electrostrictive tensors and are 0.089, -0.026, and 0.034, respectively.

The elastic strain tensor is defined as $\varepsilon_{ij} = \frac{1}{2}\left(\frac{\partial u_i}{\partial x_j} + \frac{\partial u_j}{\partial x_i}\right)$ where u is the displacement vector fields.

The coupled energy contribution accounting for the coupled strain to the polarization is:

$$\boldsymbol{f}_{coupled} = \frac{1}{2} q_{ijkl} \varepsilon_{ij} \boldsymbol{P}_k \boldsymbol{P}_l$$

Equation 3-11

Here $q_{ijkl} = 2Q_{ijmn}C_{mnkl}$. The elastic and coupled energy contributions are separated because the variation of the differentiation with respect to the polarization in the time-dependent Landau-Ginzburg-Devonshire (TDLGD) equations provides a nonzero solution for each contribution.

3.6.2 Relaxational approach

The temporal evolution of $\boldsymbol{P}$ within the system at each location was described by TDLGD equation [54,55]:

$$-\gamma \frac{\partial \boldsymbol{P}}{\partial t} = \frac{\delta}{\delta \boldsymbol{P}} \int_V f(\boldsymbol{P}) d^3 r$$

Equation 3-12

Here, $f(P)$ is the local LGD free energy density introduced above, and γ is a time constant related to the mobility of domain walls [58], which is arbitrarily set to unity, and therefore the final steady-state system configurations evolves over an arbitrary time scale. This assumption is based on the fact that the elastic strain relaxes much faster than polarization in ferroelectric materials [59]. The temperature was then immediately set below T_c for the TDLGD to be evolved until a local energy minimum was found, and the initial condition was chosen as discussed below. The simulation exit criterion is when the difference in the magnitude of the total energy is below 0.1% during two consecutive time steps. The evolution of the polarization is also coupled with that of the local internal electrostatic potential by the Poisson equation:

$$\nabla \cdot (\nabla \mathbf{\Phi}) = -\rho_b$$

Equation 3-13

where ρ_b is the bound volume charge, which is equal to $\nabla \cdot P$. The bound charges originate from the polarization discontinuities at the interfaces corresponding to the depolarization field.

For the computational model, three different sizes of SL nanostructure of $40 \times 40 \times 25$, $60 \times 60 \times 25$, and $80 \times 80 \times 25$ nm^3 were considered with periodic boundary conditions along the x-direction. The system is therefore infinitely long along the periodic direction, which is the length direction of the nanostructure in the experiment. The y- and z-directions are the non-periodic direction, and the system remains finite but considerabley smaller than the experimentally fabricated nanostructures. The nanostructure was surrounded by vacuum regions along the non-periodic directions.

Two domain configurations were considered in which the polarization within the PTO film was initially biased to form the stripe nanodomains. The domain walls are aligned either perpendicular or parallel to the milled edges of the nanostructures. An initial polarization domain period matches the experimental values also as a part of the initial conditions. The initial simulated magnitude of the polarization is 0.6 C m^{-2} in each up and down domains. No conversion of perpendicular configuration into parallel configuration or vice versa was observed but their domain configurations retained the original orientations and evolved into distinct local energy minima.

The simulations revealed that, in the nanostructures with both domain configurations, the lattices are elastically relaxed along the non-periodic directions. The relaxations along the y-direction (U_y) in perpendicular and parallel configurations are shown in Figure 3-12(a). This relaxation map indicates that both perpendicular and parallel configurations relax toward the edges

of the structure. These expansions are slightly different for the two configurations: the relaxation for the perpendicular configuration is 0.20 nm while the relxation for the parallel configuration is 0.18 nm at the edges. Particularly, the parallel configuration develops a corrugated surface, with the same periodicity as the domain pattern. The surface corrugation is expected to result from the in-plane compression of the nanostructure at domain walls in which the in-plane polar vectors at the surface are under compressive strain [26].

The simulation reveals that bulk and coupled free energy contributions among the free energy contributions are significantly different in perpendicular and parallel domain configurations as shown in Figure 3-12(b). In the parallel configuration, both energy contributions are lower than the perpendicular configuration due to the greater magnitude of the z-component of polarization, P_z. The larger P_z results from the corrugated-surface-induced compression at the near-surface domain walls. A similar near-surface relaxation at the domain boundaries has been observed in simulations of ultrathin PTO layers [60]. Although these lower energy contributions counterbalance the higher elastic energy of the parallel configuration, the total energy of the parallel configuration is still lower than that of the perpendicular configuration due to the lower bulk and coupled energy contributions. Differences in other energy contributions have a smaller influence on the total free energy compared to the difference in bulk and coupled contributions. For both perpendicular and parallel configurations, the electrostatic energy contribution is negligibly small in comparison with other energy contributions.

The results of these models of smaller nanostructures can be extrapolated to predict the behavior of nanostructures with the experimental widths of 500 and 800 nm. Figure 3-12(c) shows the dependence of the total energy of the perpendicular and parallel configurations on the width of the nanostructures. As discussed above, the total energy of the parallel configuration is always

lower than that of the perpendicular configuration for all three sizes. The extrapolation of the data in Figure 3-12 (c) indicates that the convergence in free energy of both systems will occur when the lateral sizes are much larger than the experimental samples of 500 nm and 800 nm. Therefore, the parallel configuration is energetically more favorable than perpendicular configuration in the
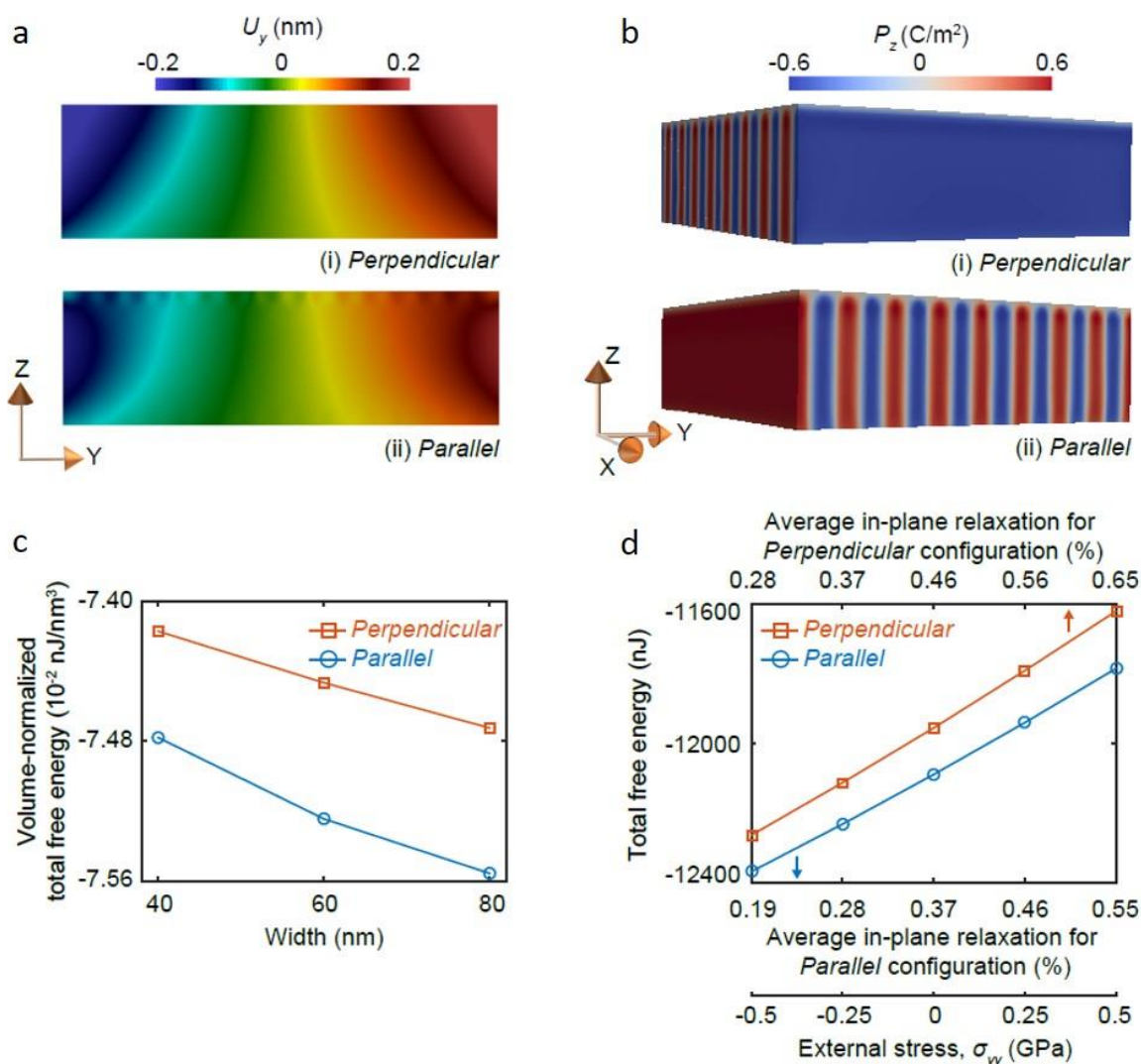
Figure 3-12: Maps of (a) the relaxation along y-direction (U_y) (b) z-component of the polarization (P_z) in the (i) perpendicular and (ii) parallel configurations in an 80 nm-wide SL nanostructure. (c) Nanostructure-width-dependent volume-normalized total free energy. Extrapolation to larger widths indicates that the parallel configuration remains energetically favorable at the experimental nanostructure widths. (d) Free energy as a function of external stress applied along the y-direction σ_{yy}, indicating that the parallel configuration is favorable under experimentally applied stresses that arise from the lithography processes.

SL nanostructures, and the observed differences between the energy contributions in both configurations are experimentally meaningful at these sizes.

It is also important to consider the possibility of the structural distortions arising from the fabrication of the SL nanostructures. For example, the SL nanostructures can be externally stressed during the FIB lithography process. To examine whether external stresses could influence the energetics of the domain wall formation, the simulation was repeated under a range of applied external stresses (σ_{yy}) up to ±0.5 GPa along the y-direction. The stress dependence of the computed free energy is shown in Figure 3-12(d). The average in-plane relaxations range from 0.28% to 0.65% or from 0.19% to 0.55%, for perpendicular and parallel configurations, respectively. The simulations show that the parallel configuration remains energetically preferable throughout the entire range of probed external stresses. The range of relaxations considered in the simulations spans (and far exceeds) the experimentally observed average in-plane strain of less than 0.1%. Therefore, the elastic artifacts associated with the lithographic processes do not substantially alter the domain-wall configuration.

3.7   Conclusion

Striped nanodomains with very small period form in the ferroelectric/dielectric PTO/STO SL contains striped nanodomains. Creating SL nanostructures provides a new direction to control the polarization domain pattern. X-ray nanobeam diffraction shows that the domain pattern is aligned with the edges of the structure. LGD calculations predict that the alignment in the SL nanostructure in which the domain wall configuration parallel to the mechanical nanostructure edges is energetically favorable than the perpendicular configuration. In particularly, the formation of the nanostructure relaxes the mechanical constraint present in the two-dimensional film. The free energy of parallel configuration is lower because the magnitude of z-component

polarization is larger, in turn, emerges because of the in-plane structural distortion present in the nanostructure. In addition, the free energy is not influenced by any external stresses that might arise from the lithography process.

A recent similar study of the edges of much larger patterns in a nearly identical PTO/STO ferroelectric/dielectric SL also indicates that domain walls are aligned along mechanical edges [61]. We thus suspect that the alignment due to mechanical phenomena will be observed in a large range of patterned structures. Manipulating the orientation and position of these complex polarization states via creating the SL nanostructures provides a new channel for applying the functional properties of nanoscale ferroelectrics.

3.8 References

[1]   J. R. Whyte and J. M. Gregg, Nat. Commun. **6**, 7361 (2015).

[2]   C. Baeumer, D. Saldana-Greco, J. M. P. Martirez, A. M. Rappe, M. Shim, and L. W. Martin, Nat. Commun. **6**, 6136 (2015).

[3]   P. Sharma, Q. Zhang, D. Sando, C. H. Lei, Y. Y. Liu, J. Y. Li, V. Nagarajan, and J. Seidel, Sci. Adv. **3**, e1700512 (2017).

[4]   S. K. Streiffer, J. A. Eastman, D. D. Fong, C. Thompson, A. Munkholm, M. V. R. Murty, O. Auciello, G. R. Bai, and G. B. Stephenson, Phys. Rev. Lett. **89**, 067601 (2002).

[5]   S. Hong, *Nanoscale phenomena in ferroelectric thin films* (SPRINGER-SCIENCE+BUSINESS MEDIA, LLC, New York, 2004). p. 16

[6]   D. J. Kim, J. Y. Jo, Y. S. Kim, Y. J. Chang, J. S. Lee, J. G. Yoon, T. K. Song, and T. W. Noh, Phys. Rev. Lett. **95**, 237602 (2005).

[7]   G. Catalan, J. Seidel, R. Ramesh, and J. F. Scott, Rev. Mod. Phys. **84**, 119 (2012).

[8]   E. J. Guo, R. Roth, A. Herklotz, D. Hesse, and K. Dorr, Adv. Mater. **27**, 1615 (2015).

[9]   W. J. Chen, Y. Zheng, W. M. Xiong, X. Feng, B. Wang, and Y. Wang, Sci. Rep. **4**, 5339 (2014).

[10]   Z. Chen, J. Liu, Y. Qi, D. Chen, S.-L. Hsu, A. R. Damodaran, X. He, A. T. N'Diaye, A. Rockett, and L. W. Martin, Nano Lett. **15**, 6506 (2015).

[11]   C. M. Folkman, S. H. Baek, H. W. Jang, C. B. Eom, C. T. Nelson, X. Q. Pan, Y. L. Li, L. Q. Chen, A. Kumar, V. Gopalan, and S. K. Streiffer, Appl. Phys. Lett. **94**, 251911 (2009).

[12]   Y. H. Chu, Q. He, C. H. Yang, P. Yu, L. W. Martin, P. Shafer, and R. Ramesh, Nano Lett. **9**, 1726 (2009).

[13]   A. Gruverman and A. Kholkin, Rep. Prog. Phys. **69**, 2443 (2006).

[14]   C. G. Duan, S. S. Jaswal, and E. Y. Tsymbal, Phys. Rev. Lett. **97**, 047201 (2006).

[15]   H. Zheng, J. Wang, S. E. Lofland, Z. Ma, L. Mohaddes-Ardabili, T. Zhao, L. Salamanca-Riba, S. R. Shinde, S. B. Ogale, F. Bai, D. Viehland, Y. Jia, D. G. Schlom, M. Wuttig, A. Roytburd, R. Ramesh, Science **303**, 661 (2004).

[16]   M. Dawber, K. M. Rabe, and J. F. Scott, Rev. Mod. Phys. **77**, 1083 (2005).

[17]   J. A. Klug, M. V. Holt, R. N. Premnath, A. Joshi-Imre, S. Hong, R. S. Katiyar, M. J. Bedzyk, and O. Auciello, Appl. Phys. Lett. **99**, 052902 (2011).

[18]   S. Hong, J. A. Klug, M. Park, A. Imre, M. J. Bedzyk, K. No, A. Petford-Long, and O. Auciello, J. Appl. Phys. **105**, 061619 (2009).

[19]   A. Schilling, R. M. Bowman, G. Catalan, J. F. Scott, and J. M. Gregg, Nano Lett. **7**, 3787 (2007).

[20]   S. M. Nakhmanson, K. M. Rabe, and D. Vanderbilt, Appl. Phys. Lett. **87**, 102906 (2005).

[21]   D. D. Fong, G. B. Stephenson, S. K. Streiffer, J. A. Eastman, O. Auciello, P. H. Fuoss, and C. Thompson, Science **304**, 1650 (2004).

[22]   G. B. Stephenson and K. R. Elder, J. Appl. Phys. **100**, 051601 (2006).

[23]   P. Zubko, N. Stucki, C. Lichtensteiger, and J. M. Triscone, Phys. Rev. Lett. **104**, 187601 (2010).

[24]   P. Zubko, N. Jecklin, N. Stucki, C. Lichtensteiger, G. Rispens, and J. M. Triscone, Ferroelectrics **433**, 127 (2012).

[25]   J. Y. Jo, P. Chen, R. J. Sichel, S. J. Callori, J. Sinsheimer, E. M. Dufresne, M. Dawber, and P. G. Evans, Phys. Rev. Lett. **107**, 055501 (2011).

[26]   P. Aguado-Puente and J. Junquera, Phys. Rev. B **85**, 184105 (2012).

[27]   M. Dawber, C. Lichtensteiger, M. Cantoni, M. Veithen, P. Ghosez, K. Johnston, K. M. Rabe, and J. M. Triscone, Phys. Rev. Lett. **95**, 177601 (2005).

[28]   H. N. Lee, H. M. Christen, M. F. Chisholm, C. M. Rouleau, and D. H. Lowndes, Nature **433**, 395 (2005).

[29]   R. Takahashi, O. Dahl, E. Eberg, J. K. Grepstad, and T. Tybell, J. Appl. Phys. **104**, 064109 (2008).

[30]   C. Thompson, D. D. Fong, R. V. Wang, F. Jiang, S. K. Streiffer, K. Latifi, J. A. Eastman, P. H. Fuoss, and G. B. Stephenson, Appl. Phys. Lett. **93**, 182901 (2008).

[31]   M. Dawber, N. Stucki, C. Lichtensteiger, S. Gariglio, P. Ghosez, and J. M. Triscone, Adv. Mater. **19**, 4153 (2007).

[32]   J. A. Tilka, J. Park, K. C. Sampson, Z. Cai, and P. G. Evans, APL Mater. **4**, 126108, 126108 (2016).

[33]   Y. Ahn, J. Park, A. Pateras, M. B. Rich, Q. Zhang, P. Chen, M. H. Yusuf, H. Wen, M. Dawber, and P. G. Evans, Phys. Rev. Lett. **119**, 057601 (2017).

[34]   J. Y. Jo, P. Chen, R. J. Sichel, S.-H. Baek, R. T. Smith, N. Balke, S. V. Kalinin, M. V. Holt, J. Maser, K. Evans-Lutterodt, C.-B. Eom, and P. G. Evans, Nano Lett. **11**, 3080 (2011).

[35]   R. M. Fleming, D. B. McWhan, A. C. Gossard, and W. Wiegmann, Bull. Am. Phys. Soc **51**, 357 (1980).

[36]   X-Ray Nanobeam Diffraction Simulator

http://xray.engr.wisc.edu/nanobeamsimulation/html/index.php.

[37]   J. A. Tilka, J. Park, Y. Ahn, A. Pateras, K. C. Sampson, D. E. Savage, J. R. Prance, C. B. Simmons, S. N. Coppersmith, M. A. Eriksson, M. G. Lagally, M. V. Holt, and P. G. Evans, J. Appl. Phys. **120**, 015304 (2016).

[38]   A. Ying, B. Osting, I. C. Noyan, C. E. Murray, M. Holt, and J. Maser, J. Appl. Crystallogr. **43**, 587 (2010).

[39]   Q. Zhang, E. M. Dufresne, P. Chen, J. Park, M. P. Cosgriff, M. Yusuf, Y. Dong, D. D. Fong, H. Zhou, Z. Cai, R. J. Harder, S. J. Callori, M. Dawber, P. G. Evans, and A. R. Sandy, Phys. Rev. Lett. **118**, 097601 (2017).

[40]   F. Hofmann, E. Tarleton, R. J. Harder, N. W. Phillips, P.-W. Ma, J. N. Clark, I. K. Robinson, B. Abbey, W. Liu and C. E. Beck, Sci. Rep. **7**, 45993 (2017).

[41]   J. Park, Y. Ahn, J. A. Tilka, K. C. Sampson, D. E. Savage, J. R. Prance, C. B. Simmons, M. G. Lagally, S. N. Coppersmith, M. A. Eriksson, M. V. Holt, and P. G. Evans, APL Mater. **4**, 066102 (2016).

[42]   P. Cendula, S. Kiravittaya, Y. F. Mei, C. Deneke, and O. G. Schmidt, Phys. Rev. B **79**, 085429 (2009).

[43]   B. Krause, C. Mocuta, T. H. Metzger, C. Deneke, and O. G. Schmidt, Phys. Rev. Lett. **96**, 165502 (2006).

[44]   N. A. Pertsev, A. G. Zembilgotov, and A. K. Tagantsev, Phys. Rev. Lett. **80**, 1988 (1998).

[45]   G. Rispens and B. Noheda, Integr. Ferroelectr. **92**, 30 (2007).

[46]   E. Salvati, T. Sui, A. J. G. Lunt, and A. M. Korsunsky, Mater. Des. **92**, 649 (2016).

[47]   A. M. Korsunsky, J. Guenole, E. Salvati, T. Sui, M. Mousavi, A. Prakash, and E. Bitzek, Mater. Lett. **185**, 47 (2016).

[48]   N. Bergeard, S. Schaffert, V. L.-Flores, N. Jaouen, J. Geilhufe, C. M. Günther, M. Schneider, C. Graves, T. Wang, Be. Wu, A. Scherz, C. Baumier, R. Delaunay, F. Fortuna, M. Tortarolo, B. Tudu, O. Krupin, M. P. Minitti, J. Robinson, W. F. Schlotter, J. J. Turner, J. Lüning, S. Eisebitt, and C. Boeglin, Phys. Rev. B **91**, 054416 (2015).

[49]   A. Boulle, I. C. Infante, and N. Lemee, J. Appl. Crystallogr. **49**, 845 (2016).

[50]   S. Choudhury, Y. Li, N. Odagawa, A. Vasudevarao, L. Tian, P. Capek, V. Dierolf, A. N. Morozovska, E. A. Eliseev, S. Kalinin, Y. Cho, L.-Q. Chen, and V. Gopalan, J. Appl. Phys. **104**, 084107 (2008).

[51]   X. W. Deng and X. F. Chen, Opt. Express **18**, 15597 (2010).

[52]   Y. L. Li, S. Y. Hu, Z. K. Liu, and L. Q. Chen, Appl. Phys. Lett. **78**, 3878 (2001).

[53]   I. Naumov and A. M. Bratkovsky, Phys. Rev. Lett. **101**, 107601 (2008).

[54]   J. Mangeri, Y. Espinal, A. Jokisaari, S. P. Alpay, S. Nakhmanson, and O. Heinonen, Nanoscale **9**, 1616 (2017).

[55]   D. Gaston, C. Newman, G. Hansen, and D. Lebrun-Grandie, Nucl. Eng. Des. **239**, 1768 (2009).

[56]   J. Y. Jo, R. J. Sichel, E. M. Dufresne, H. N. Lee, S. M. Nakhmanson, and P. G. Evans, Phys. Rev. B **82**, 174116 (2010).

[57]   B. Bein, H. C. Hsing, S. J. Callori, J. Sinsheimer, P. V. Chinta, R. L. Headrick, and M. Dawber, Nat. Commun. **6**, 10136 (2015).

[58]   Q. P. Meng, M. G. Han, J. Tao, G. Y. Xu, D. O. Welch, and Y. M. Zhu, Phys. Rev. B **91**, 054104 (2015).

[59]   Y. L. Li, S. Y. Hu, Z. K. Liu, and L. Q. Chen, Acta Mater. **50**, 395 (2002).

[60]   Z. J. Jiang, R. Z. Zhang, D. W. Wang, D. Sichuga, C. L. Jia, and L. Bellaiche, Phys. Rev. B **89**, 214113 (2014).

[61]   M. Hadjimichael, E. Zatterin, S. Fernandez-Pena, S. J. Leake, and P. Zubko, Phys. Rev. Lett. **120**, 037602 (2018).

Chapter 4: Focused optical pump/X-ray probe nanodiffraction

4.1 Introduction

The interaction between light and matter in a crystal results in a photostrictive distortion of the atomic unit cell, which is a non-thermal structural deformation associated with photoinduced converse piezoelectric effects in polar materials [1,2]. The photostrictive effect is observed in the ultrafast time regime using ultrafast optical pulses with durations from femtoseconds to picoseconds. This regime is an excellent match for the ultrafast lattice dynamics in solids [3] that can be studied by time-resolved X-ray diffraction. The technique can elucidate ultrafast phenomena of condensed matter, including ultrafast laser-induced lattice dynamics of oxide materials [4-7]. In other systems, ultrafast optical pulses are widely used for applications in materials processing via local heating [8], laser ablation [9-11], and laser structuring [12].

Photostriction in complex oxide ferroelectric systems such as bismuth ferrite, $BiFeO_3$ (BFO), a room temperature multiferroic [13], has been observed as an ultrafast photoinduced lattice expansion on the order of 0.1% at the picosecond timescale [2,4,5,7]. The results were obtained using time-resolved X-ray diffraction combined with an ultrafast optical laser setup. The optical beam is used as a pump signal and the X-ray beam is used to measure optically induced structural changes. This system provides insight into time-dependent optically induced structural alterations in crystals by probing either the intensities or positions of the Bragg reflections. To resolve the structural changes in the ultrafast time regime, optical pulses with durations of femtoseconds are used to pump the structure. The arrival time of the optical pulses to the sample must be delayed relative to the X-ray beam to probe the time-dependent structural changes. The optical pump beam is often focused down to sizes that match (or exceed) the size of the X-ray beam footprint. This ensures the information about structural changes is measured only from the

optically excited volume. The X-ray beam must be focused when higher spatial resolution is necessary [14]. The development of X-ray focusing optics, such as the Fresnel zone plates and Kirkpatrick-Baez mirrors, permits the creation of X-ray beams from synchrotron light sources with spot sizes on the order of tens to hundreds of nanometers [15-17].

This chapter describes an instrument allowing tightly focused optical beams (a few micrometers) combined with X-ray nanodiffraction [18]. Development of this instrument is essential whereby the optical illumination can be spatially confined in an area of several micrometers to probe the localized and optically induced transient. Another benefit of using the focused optical beam is to improve the thermal stability of the X-ray experiment by reducing the total optical power, yet retaining sufficiently high optical fluence. The required optical fluence ranges from several mJ/cm^2 for non-destructive studies of optically induced transients [4,5,8,12] to several J/cm^2 for purposes of ablation, machining, and surface structuring [9-11]. When using the focused optical beam, the low optical power on the order of 10 µW produces a fluence of 1 mJ/cm^2 with experimentally useful repetition rates of tens of kHz. Attaining a similar optical fluence with more conventional 500 µm-scale optical beams would require the total power on the order of 10 mW, which would lead to a time-averaged temperature increase in the sample. Thus, the tightly focused optical beam can reduce the optical power by more than three orders of magnitude ensuring thermal stability during the X-ray nanobeam studies.

4.2 Experimental setup

The focused optical pump was combined with X-ray nanodiffraction. The focused optical beam was delivered to the sample while the X-ray nanobeam probed the sample at various delay times from several hundred picoseconds to tens of nanoseconds. The optical pump/X-ray nanobeam instrument is schematically shown in Figure 4-1. There are three important aspects of

the design: (i) optical and X-ray focusing optics, (ii) optical focal spot characterization and alignment, and (iii) positioning the sample and optical arrangement to permit two-dimensional X-ray diffraction microscopy.

As shown in Figure 4-1, the ultrafast optical pulse was coupled with the optical fiber and delivered to the focusing optics. The focusing optics is consisted of the collimator and the objective lens mounted on the 3-axis piezoelectric positioner, which is referred to as an objective translation stage (OTS). The OTS and the sample were mounted on the same metal frame (sample stage), which were in turn mounted on the 3-axis piezoelectric flexure scanning stage, which is referred to as a piezoelectric translation stage (PTS, nPoint, Inc.). The OTS was used to move the focused optical beam over the sample surface to ensure spatial overlap between the optical beam and the footprint of the X-ray nanobeam. The PTS was used to drive the focused X-ray beams, while the position of the focused optical beam spot was fixed on the sample surface for the X-ray microscopy. The PTS was mounted on the 3-axis stepper-motor-driven coarse translation stage, which is referred to as a stepper-motor translation stage (STS, MFN25PP, Newport, Inc.) for a course motion ($\sim \mu m$), for example, choosing different regions of interest on the sample. Lastly, the STS was mounted on the four-circle x-ray diffractometer to provide control of the angular orientation of the sample for the *2θ* scattering.
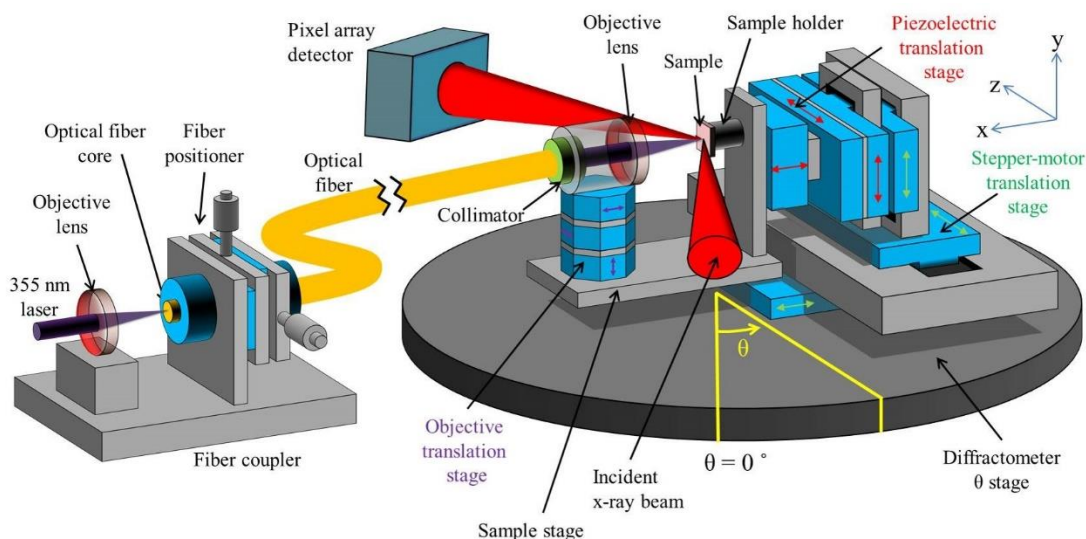
Figure 4-1: Optical pump/x-ray nanobeam instrument. An optical pulse with wavelength 355 nm is coupled into a single-mode optical fiber. The output of the fiber is collected by a collimator and focused by an objective lens onto the sample.

4.2.1 Fiber coupling and focusing

In the experiment, optical pulses (Duetto, Time-Bandwidth Products AG) producing 10 ps-durations at a fundamental wavelength of 1064 nm were converted to 355 nm (3.49 eV) through third harmonic generation [19]. The maximum optical power was 10 W with a repetition rate of 54 kHz, which corresponds to 18.5 μJ/pulse. The repetition rate was chosen to match 1/5 of 6.5 MHz, a repetition rate of the 24-bunch synchrotron X-ray operating mode of the Advanced Photon Source (APS) at the Argonne National Laboratory (ANL). Matching the repetition rates of the optical and the synchrotron X-ray beams is important to have precise temporal overlap in the time-resolved pump/probe experiment. Especially, the high repetition rate of the optical beam allows shortening of the measurement time as well as reducion of laser-induced damage on the sample. The time interval between optical pulses of 18.5 μs was suitable for the time-resolved optical excitation experiment in which the recovery of the optically induced transient was completed before re-excitation by a subsequent optical pulse.

The femtosecond pulsed ultrafast optical beam was coupled to a single-mode optical fiber providing a better-confined shape of the focused optical beam in which the spatial overlap between the focused optical beam and the X-ray nanobeam is required for small objects. Moreover, less than 10% coupling efficiency of the optical fiber allows us to lower the optical power to reduce the time-averaged temperature increase. Considering a multimode fiber instead of using the single-mode fiber is also valid, but the laser pulse width broadening effect matters when the broadened pulse width is much larger than the synchrotron X-ray duration. This is due to a modal dispersion in which the coupled optical rays propagate in the fiber with various incident angles set by the fiber numerical aperture (NA) relative to the traveling axis. Difference in the paths of the optical propagation in the fiber leads to different arrival times at the other end of the fiber. The maximum difference in the path length is determined by two rays propagating in the fiber with the extreme incident angles set by the NA. The estimated maximum difference in the path length, considering 1-m-long fiber with its NA of 0.13 and refractive index n of 1.47, is about 8.6 mm. It corresponds to the temporal broadening of several tens of picoseconds. The temporal broadening of the optical pulse resulting from a multimode optical fiber would thus be much less than the typical X-ray duration in the 24-bunch operating mode of the APS at the ANL [20,21].

Staring from the far-left side of Figure 4-1, one end of the optical fiber (F-SM-300- SC, Newport, Inc.) with its wavelength range of 305–450 nm was connected to the fiber positioner (FPR1-C1A, Newport, Inc.) on the fiber coupler (F-91-C1, Newport). The optical beam was focused using the first objective lens (U-27X, Newport, Inc.) placed on the other side of the fiber coupler. The mode field diameter, specified as the diameter at which the field intensity is reduced by a factor of $1/e^2$ of its maximum [22], was 3 µm. The NA of the objective lens was 0.13, and that of the fiber ranged from 0.12 to 0.14. The fiber positioner was then gently adjusted to place

the focused optical beam in the middle of the fiber core. The laser-coupled optical fiber was then delivered to the sample stage. The optical beam exiting the fiber was collected by the collimator (CFC-11X-A, ThorLabs, Inc.) with a focal length of 11 mm. The collimated optical beam was focused down to a spot size of several micrometers using another objective lens (UV0928, Universe Kogaku America, Inc.) with an NA of 0.18 and front and back focal lengths of 8.995 and 11.075 mm, respectively. The collimator and the second optical objective lens were mounted on the OTS (ANPx101 and ANPz101, Attocube System AG) consisting of three piezoelectric stages (x, y, and z-stages). The role of these stages is to translate the focusing optics to place the depth of field (DOF) of the optical beam on the sample surface (using x-stage). Translating the focusing optics ensures spatial overlap between the laser focal spot and the footprint of the focused X-ray spot (using y and z-stages).

The translation motions for the laser focusing optics was controlled independently of the rotational parts for the X-ray diffraction. Therefore, the laser focusing optics was placed on the sample stage together with the sample, and the incident angle of the focused optical beam was always normal to the sample surface. This provides consistent optical absorption by the sample while the Bragg diffraction angle varies depending on the order of Bragg condition. For example, the 001 and 002 Bragg reflections for the general complex oxide ferroelectric thin films, of which the lattice constant is about 4 Å, are typically at around 10° and 20° when using a 10 keV X-ray photon energy.

Additionally, the laser focusing optics on the OTS should be lighter than the maximum load of each stage, which is 100 and 200 g for x or y and z stages, respectively. The optical power was measured at the output of the optical fiber to determine the coupling efficiency and thus the

experimental optical power was selected. A LabVIEW program was coded to operate the stages as discussed in Chapter 4.2.2.

4.2.2 LabVIEW control program

The OTS was responsible for positioning the focused optical beam on the sample as well as its DOF at the sample surface. The piezoelectric-driven stick-slip principle was used to translate the stages by applying a pulsed electric field using the piezo positioning controller (ANC 300, Attocube System AG). The pulse rate was manually fixed to be 1 kHz, and thus the travel distance was set by the magnitude and duration of the pulsed electric field. Precise motion control is required to ensure the spatial overlap between the focused optical beam and the X-ray spots on the sample surface and to measure the focused optical beam spot size as described in Chapter 4.2.3.

Figure 4-2 shows the front panel (control interface) of the coded LabVIEW program. As soon as the program was running, it started communicating with the piezo positioning controller, and the user chose the stages to move (top, middle, and bottom correspond to x-, y-, and z- stages) as well as the travel direction. The default setting of the magnitude of the pulsed electric filed were 20 and 30 V for the stage along x- (or y-) and z-stages, respectively. The traveling distance was measured by an optical microscope, and the traveling speed (µm/step) was manually calibrated for each stage. Once the target travel direction and distance were determined, the number of pulses was automatically calculated and applied to the stages. There are two operation modes (single and continuous) in which the stage moves only one time to the target distance, or the stage continuously
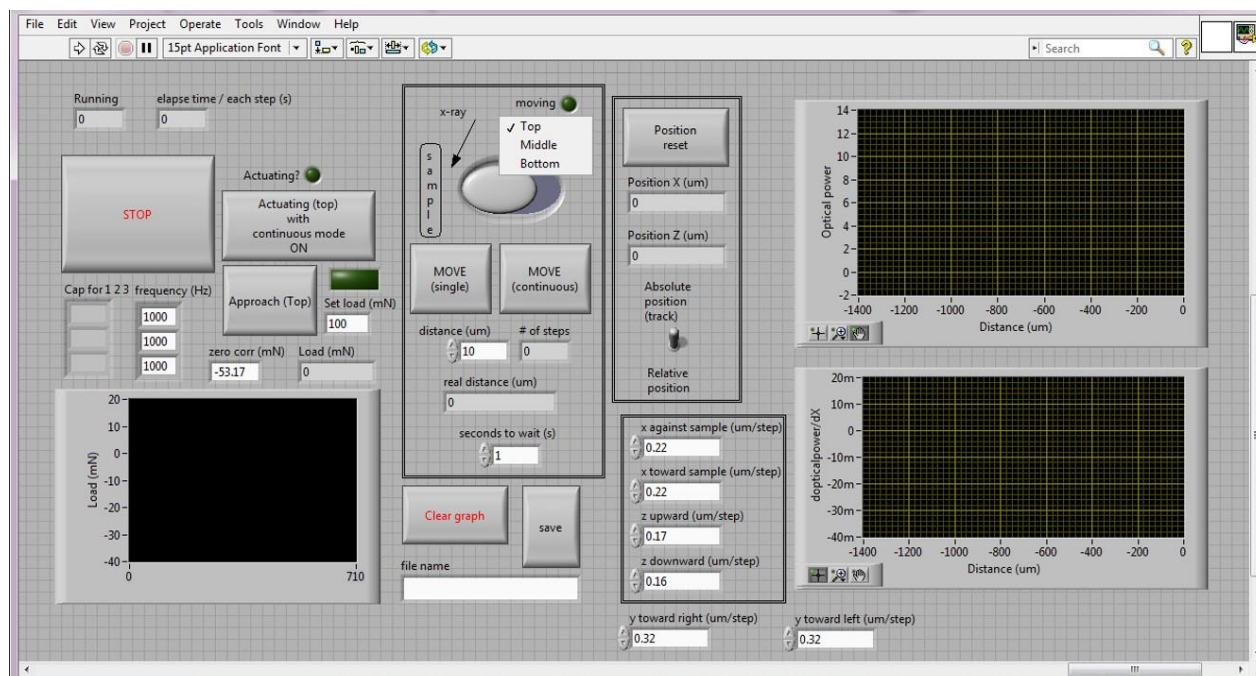
Figure 4-2: Front panel of LabVIEW program that shows how the user interface looks like to operate the program. Each stage can be selected to run separately, and their traveling speed is required to be manually calibrated before experiments. Measured optical power and the travel distance can be monitored and plotted in the two graphs on the right in real time, and saved upon clicking the save button when needed.

moves by the target distance until cancelled. The program also communicated with the optical

power meter to display the measured optical power in real time while the pulsed electric field was

applied. The travel distance and its direction were also monitored at the same time and plotted in

two graph indicators, as shown in Figure 4-. A round trip can be programmed by setting a turning

point in which the sign of the electric field application is inverted when the stage reaches the set-

point and travels back to the starting point.

4.2.3 Optical spot size characterization

The size of the optical beam on the sample in previous time-resolved pump/probe

experiments ranged from 50 to 500 µm, for which a large amount of total optical power might

increase the sample temperature. To avoid an unwanted temperature-rise, the total optical input

power needs to be reduced. Thus, the size of the optical beam size needs to be smaller to retain the

optical fluence for the optically induced transient. The typical size of the focused X-ray on the sample in the experiment was about 300 nm, and the focused optical beam spot size on the sample matched the focused X-ray spot size. The FWHM of the focused laser spot size D on the sample surface can be computed from the size of the image of the mode field radius w of the fiber [23].

$$D = \frac{\sqrt{2ln2}}{2} \times M \times w$$

Equation 4-1

With the magnification (M, in our case it is 1.01), which is defined as the ratio of the focal length of the collimator to the back focal length of the objective lens, the mode field radius (half of the diameter) is magnified. The FWHM is a factor of $\sqrt{2ln2}$ larger than the magnified mode field radius. Here D is expected to be 1.8 µm, which is approximately 30 to 300 times smaller than the typical optical pump sizes employed in previous experiments.

The size of the focused optical spot was measured using a setup shown in **Error! Not a valid bookmark self-reference.** (a). An opaque knife edge was used to block half of the power meter. This allowed measurement of the size of the focused optical beam spot. The objective lens together with the collimator were vertically translated across the knife edge while the optical power was measured. Before measuring the focused optical beam spot size, the objective lens and the collimator were scanned along the *x*-axis using the round-trip technique by the LabVIEW program to ensure the DOF of the focused optical beam was on the power meter detector plane. As shown in **Error! Not a valid bookmark self-reference.** (b), parabolic shapes of the optical power were measured because the middle of DOF was located when the power was at the minima, and continuous mode was used to plot multiple curves of the power. After locating the focused optical
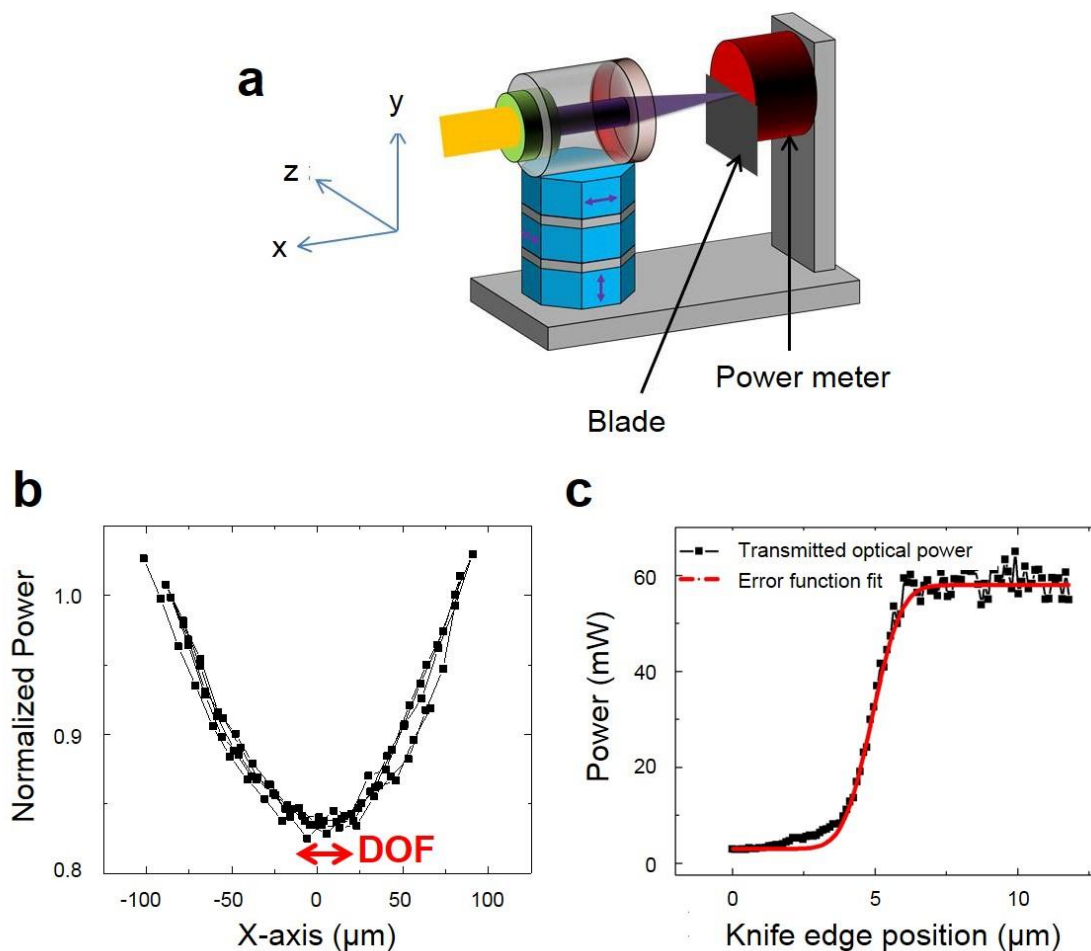
Figure 4-3: (a) Optical spot size measurement by scanning the focused optical beam across a knife edge using the translation stage supporting the collimator and objective lens. (b) Transmitted optical power as a function of the displacement along the x-axis of the laser in which the half of laser power is blocked by the knife edge. The laser is positioned in the middle of the depth of focus (DOF) before measuring the power while moving the laser along the y-axis. (c) Transmitted optical power as a function of the displacement along the y-axis of the laser relative to the knife edge. The full width at half maximum given by the error function fit (solid line) is 1.9 µm.

beam at the minima, the transmitted optical power as a function of the relative knife edge position

along the *y*-axis was measured, as shown in **Error! Not a valid bookmark self-reference.** (c).

The error function fit of the optical power curve gives a FWHM of 1.9 µm for the intensity of the

focused optical beam.

The absorbed fluence (F_a) was used to describe the magnitude of the sample excitation. F_a

is defined as the optical fluence transmitted through the surface of the sample and absorbed within

a thin film sample [5]. At normal incidence, F_a depends on the incident laser fluence (F_i), the optical refractive index of the sample (n_s), the optical absorption coefficient of the film (α), and the film thickness (Δ). With approximations that reflection at the substrate/film interface and nonlinear effects are negligible, the absorbed fluence is

$$F_a = F_i\left(1 - \left(\frac{n-1}{n+1}\right)^2\right)(1 - exp(-\alpha\Delta))$$

Equation 4-2

For BFO, n and α are 3.396 and 0.035 nm^{-1} at a wavelength of 355 nm [24]. For the present case of a film with thickness $\Delta = 35$ nm, F_a is $0.49F_i$.

4.3   Time-resolved X-ray diffraction on BiFeO₃

The optical pump/X-ray probe system was characterized using a time-resolved X-ray nanodiffraction experiment at station 7-ID-C of the APS, in which the pulsed optical beam was delayed relative to the X-ray arrival time to the sample. The concept of the timing in which the optical and X-ray pulses coincide on the sample surface is called time-zero (T_0). The positive (negative) T_0 represents the arrival time of the optical beam after (before) the X-ray pulse arrives at the sample. The X-ray detector was gated to choose the number of the X-ray pulses reflected from the sample before or after the optical excitation. As shown in Figure 4-4, an X-ray pulse of 100 ps width was delivered to the sample every 152 ns. The laser repetition rate was 54 kHz, which is useful for the experiments with the recovery time of the photoinduced effect being less than 18.5 μs. The photoinduced lattice response was measured as a function of optical beam delay. Previous optical pump/X-ray probe time-resolved studies on 35 nm thick BFO thin films have reported a
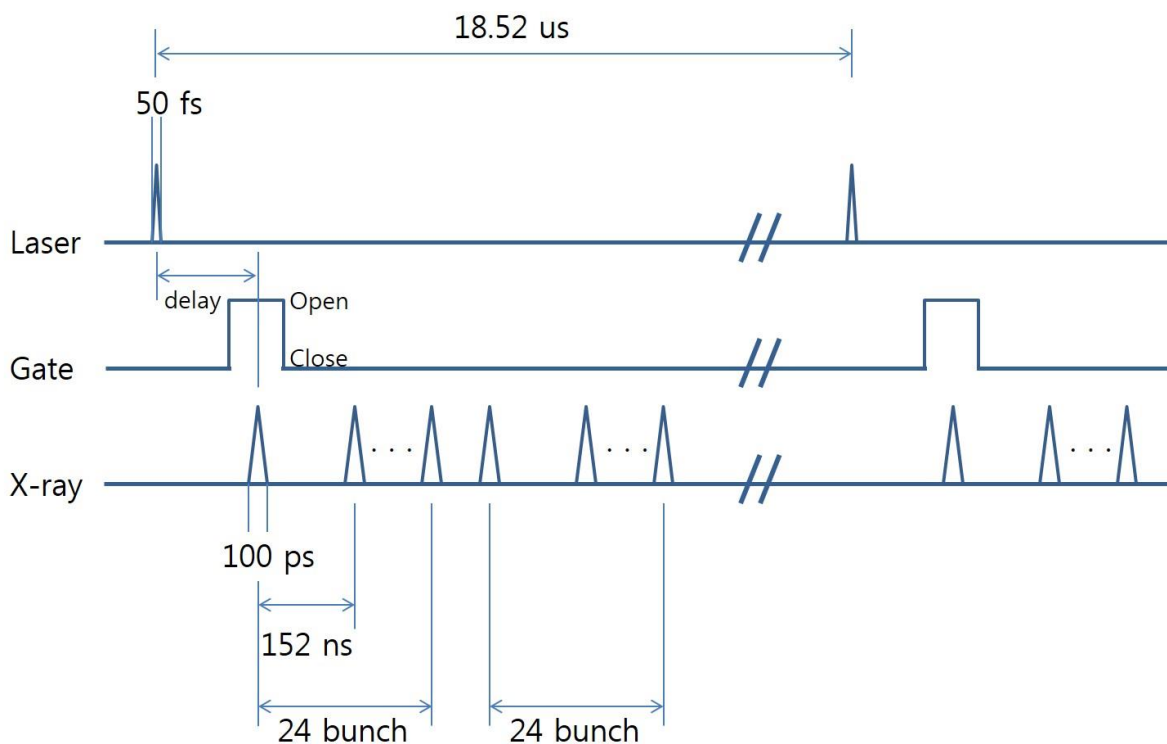
Figure 4-4: Timings of laser pump and x-ray probe pulses as well as the detector gating signal. The laser width is 50 fs with the repetition rate of 54 kHz (18.52 μs), and its time of arrival to the sample can be delayed relative to 100-ps x-ray pulses with the repetition rate of 6.5 MHz. The detector gating can also be electronically selected to collect the limited number of diffracted x-ray pulses.

photoinduced out-of-plane lattice expansion up to 0.44% within a time less than 100 ps with an absorbed fluence of 3.5 mJ/cm^2 [20,21].

The charge carriers excited by the optical illumination screen the depolarization field in the ferroelectric film, which leads to the photoinduced lattice expansion. The time dependence was investigated using the X-ray diffraction with various optical pulse delays. Incident X-rays with photon energy of 10 keV were focused to a spot of 300 nm FWHM on the sample using a Fresnel zone plate. The diffraction angles for the Bragg condition led to a large footprint of approximately 1 μm. Diffraction patterns were collected using a pixel array detector (Pilatus 100K, Dectris, Ltd.), and gated to detect only diffracted X-rays arriving after a specified delay. The detector was placed on the *2θ* arm of the four-circle diffractometer and located at 36.4°, a nominal *2θ* angle for BFO

pseudocubic 002 Bragg reflection. The regions of interest illuminated by the X-ray beam were required to be positioned at the center of rotation of the four-circle diffractometer, at which the X-ray nanobeam was also focused. Several one- or two-dimensional scans using the OTS were carried out to search for the spatial overlap between the focused optical and X-ray beams. Micrometer-scale maps of the optical response were acquired by scanning the sample using the PTS. The time-dependence of the response of the BFO following the optical excitation was observed by varying the arrival time of the optical pulses relative to the fixed timing of the X-ray pulses.

4.4   Photoinduced structural changes

The spatial variation and dynamics of the optically induced effects were evaluated by a series of X-ray diffraction experiments. As observed in the previous optical pump/X-ray probe experiments in ferroelectric thin films, there are normally photoinduced effects on a lattice that expands or contracts depending on the origin or time scale of the measurement. The photoinduced effect observed in BFO thin film was a lattice expansion measured using X-ray diffraction studies with the focused optical beam. The lattice expansion results from both electronic and thermal contributions. The depolarization screening effects increases the magnitude of the polarization as well as the lattice constant, and the heat generated by the absorbed laser by the sample leads to thermal expansion. These results were observed by conducting rocking curve scans around the 002 BFO Bragg reflection to investigate changes in the lattice constant by measuring the position of the Bragg reflection. The time-resolved rocking curve scan was also conducted to probe the dynamics of the lattice expansion.
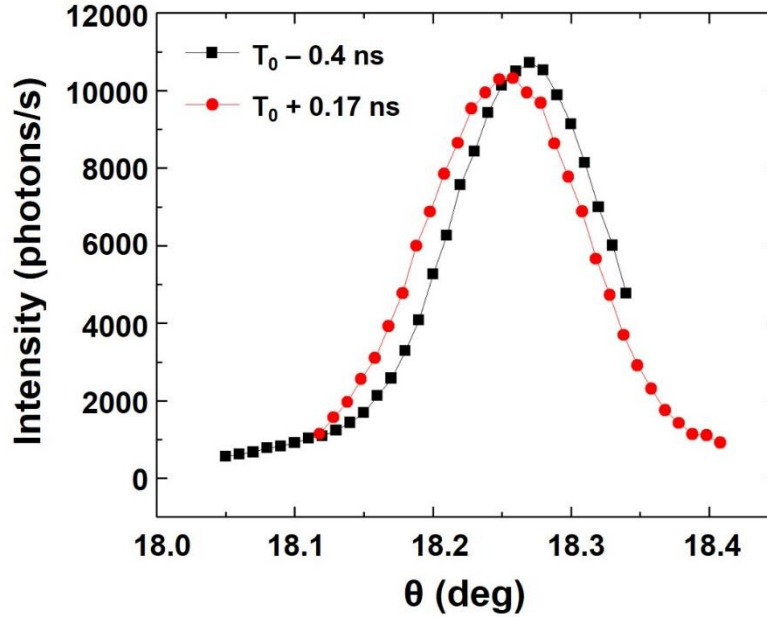
Figure 4-5: Rocking curves of the intensity of the BiFeO3 pseudocubic 002 Bragg reflection as a function of the incident x-ray beam angle. The diffracted x-ray intensity was measured with x-ray pulses arriving at times 0.4 ns before (black) and 0.17 ns after (red) the temporal coincidence of the optical and x-ray pulses, defined as time T_0. The scan at positive delay exhibits a peak shift from 18.27° to 18.25°, corresponding to an optically induced out-of-plane lattice expansion of 0.11%.

When using a two-dimensional X-ray detector, rocking curve scans around Bragg reflections also scans a specular direction along the 00L direction of the structure in reciprocal space. Figure 4- shows rocking curve scans around the BFO 002 Bragg reflection intensity as a function of the X-ray incident angle θ. Time-resolved photoinduced lattice expansion was measured at two different delay times; 0.4 ns before (black) and 0.17 ns after (red) the optical excitation. The Bragg angle associated with the maximum intensity of the 002 BFO Bragg reflection shifted from 18.27° to 18.25° following optical excitation. This corresponds to an out-of-plane lattice expansion of 0.11% $\left(-\frac{cos18.27}{sin18.27} \frac{(18.25-18.27)\pi}{180} \right)$, which is consistent with the previous photoinduced lattice expansion with the 1 mJ/cm^2 of an unfocused laser [4,5].
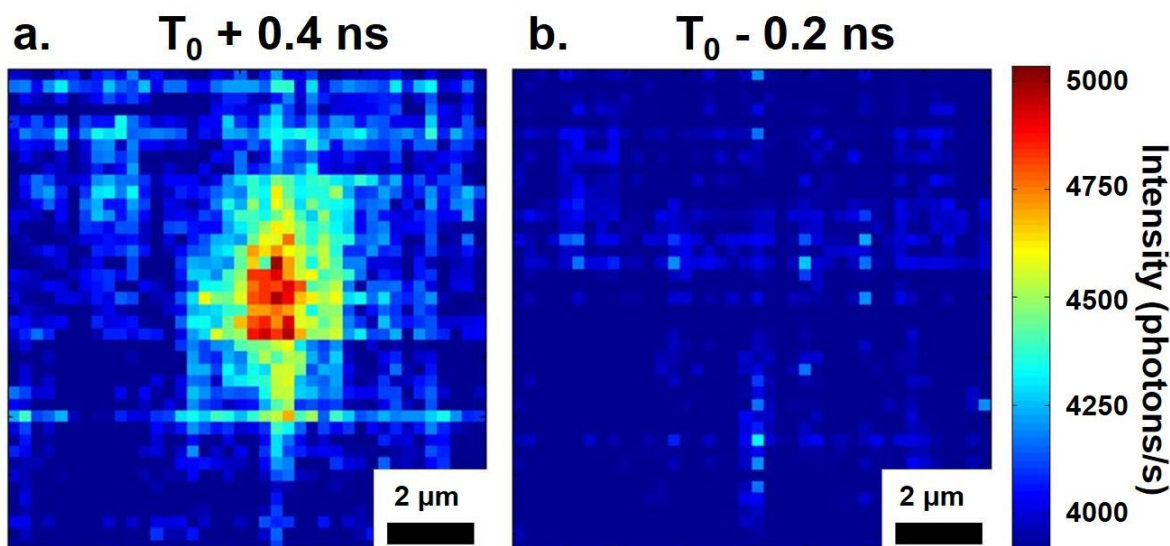
Figure 4-6: Two-dimensional maps at times after and before T_0 at an x-ray incident angle of $\theta = 18.20°$, below the Bragg angle of 18.27°. (a) At positive delay, $T_0+0.4$ ns, the optically induced expansion leads to increased intensity in the central region of the map in which the optical pulse was focused. (b) At negative delay, $T_0-0.2$ ns, where photoinduced expansion is not apparent.

A micrometer-scale spatial variation in the photoinduced structural distortion that matched the shape and size of the focused laser in two-dimensional space was measured to verify the thermal stability of the instrument. Scanning the focused X-ray around the area on the sample in which the focused laser distorts the lattices provides a map of the spatial variation of the lattice distortion. To map a region of interest, the incident angle of the focused X-ray was fixed, and its focal spot on the sample is rastered by translating the sample stage in y-z plane (See Figure 4-1). The incident angle of the focused laser was kept normal to the sample surface, and its focal spot on the sample was fixed during mapping process. As shown in Figure 4-6, the map tests the thermal stability and spatial resolution of the instrument. The incident X-ray angle was fixed at $\theta = 18.20°$ during the spatial map, lower than the steady-state BFO 002 Bragg angle at $\theta = 18.27°$. Regions in which the lattice expanded have the Bragg condition shifted to a lower angle and thus appear as bright intensity in the map. The optically induced lattice expansion appears as a localized area of brighter intensity. The maximum intensity in the optically excited region at $t = 0.4$ ns in Figure

4- (a) was a factor of 1.2 larger than in the unilluminated regions. The corresponding measurement at t = -0.2 ns in Figure 4- (b) represents the case where the X-ray pulse arrives before the optical excitation and exhibits no optically induced distortion. The photoinduced effect thus nominally recovers within the 18.5 µs interval between optical pulses.

The stability of the instrument was also tested by tracking the motion of features of higher or lower steady-state diffracted intensity in Figure 4-6. Tracking the motions of the features allowed estimation of the velocity at which the sample was moving relative to the focused X-ray spot. Isolated regions producing higher or lower diffracted intensity can arise, for example, from structural artifacts due to epitaxial growth, as commonly observed in BFO thin films [25]. Local intensity variation was tracked between the two scans of in Figure 4- (a) and (b) to estimate the
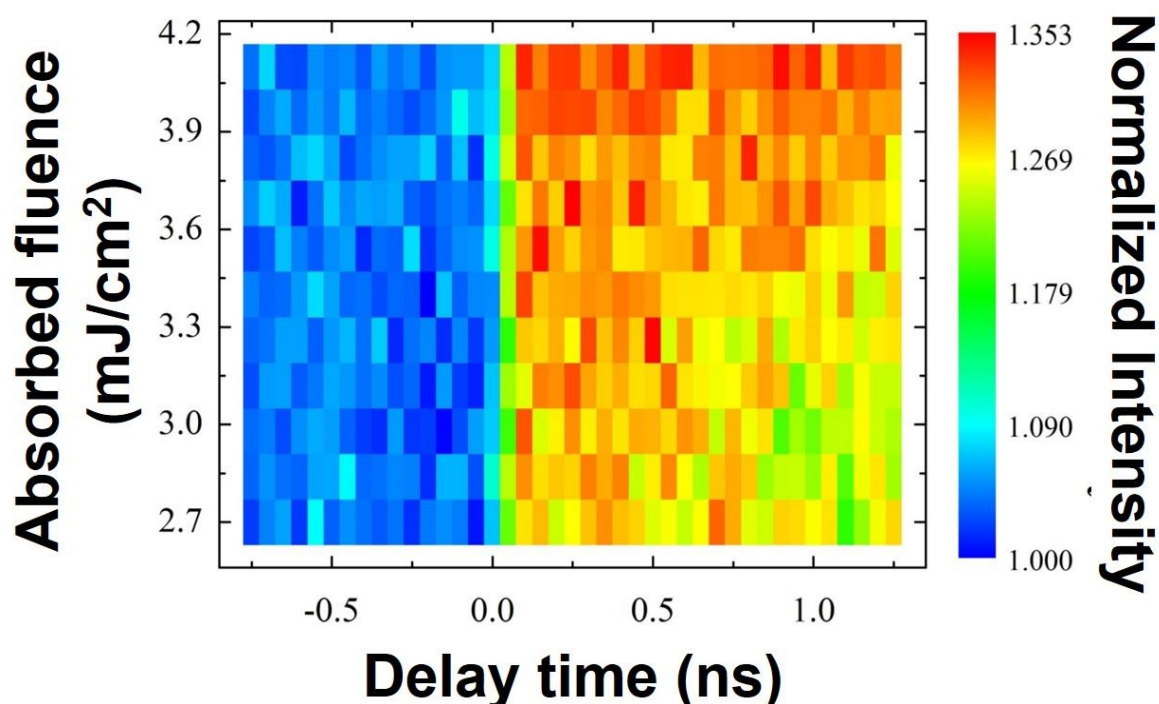
Figure 4-7: Change in diffracted x-ray intensity during a time-resolved experiment with various fluences. The incident x-ray angle is fixed slightly lower than the Bragg angle so the measured intensity becomes brighter due to the lattice expansion after T_0.

drift of the X-ray spot. The observed total shift was 0.5 µm during the 1.1 h interval between the scans, corresponding to a drift of 0.45 µm/h.

The change in magnitude of lattice expansion at different fluences was measured as a function of the optical pulse delay, as shown in Figure 4-. A different X-ray incident angle was used at which the intensity change is less sensitive to structural distortion than the results discussed above. The change in intensity apparently begins at T_0, and the normalized intensity becomes brighter as the fluence increases, demonstrating that the photoinduced lattice expansion is a function of the optical fluence.

The photoinduced lattice distortion recovers back to the undistorted state within a time scale of a few nanoseconds to several tens of nanoseconds, through a combination of a carrier recombination and a thermal relaxation processes [5]. A study of the recovery dynamics of the photoinduced lattice distortion in BFO thin film was conducted at different regions of the sample. The laser with an absorbed fluence of 1 mJ/cm^2 was spatially overlapped with the position of the focused X-ray spot and delayed from -1 to 16 ns. To measure the change in intensity as the Bragg peak shifts due to the optical illumination, the incident X-ray angle was fixed at 0.06° below the steady-state Bragg angle of the BFO 002 reflection. Because of the photoinduced lattice expansion, the intensity increased by a factor of 1.3 immediately following optical excitation, as shown in Figure 4-. This is due to the incident X-ray angle being slightly lower than the Bragg condition before lattice expansion, and the intensity increases as the Bragg reflection shifts to the lower angle direction in reciprocal space. This perturbation decays over a period of several nanoseconds with complex time dependence, initially falling by a factor of 2 within the first 4 ns, but persisting at a smaller level until at least 16 ns after excitation, as illustrated in Figure 4- (b). The initial rapid decay is associated with electronic phenomena in which the photoexcited charged carriers are

recombined, followed by a slower decay until the end of the scan, which is associated with the slow relaxation of the thermal expansion of the film. To characterize the spatial variation of the dynamics of photoinduced lattice distortion under laser illuminated regions, the relative position of the X-ray spot was scanned across a 25 μm wide at delay times from 0.15 to 16 ns. The dynamics of the change in intensity agrees within the timescale observed at a local position, as shown in Figure 4- (a). A key feature of the relaxation shown in Figure 4- (b) is that the lateral extent of the distorted region does not expand in the time following optical excitation, which is consistent with the relatively large lateral scale (microns) in comparison with the smaller 35 nm thickness of the film. The longitudinal sound velocity in BFO is 3.5 nm/ps, and thus the propagation of the initial acoustic impulse through the thickness of the BFO layer is too fast to be captured with the time-resolution of this measurement [5]. The range of the scan in the lateral direction was sufficiently large to capture the acoustic transient, but no acoustic distortion is apparent in Figure 4- (b). Thus, it is suspected that the insufficient distortion arising from the propagation of the acoustic impulse in the lateral direction cannot be distinguished from the structural variation of the BFO layer.
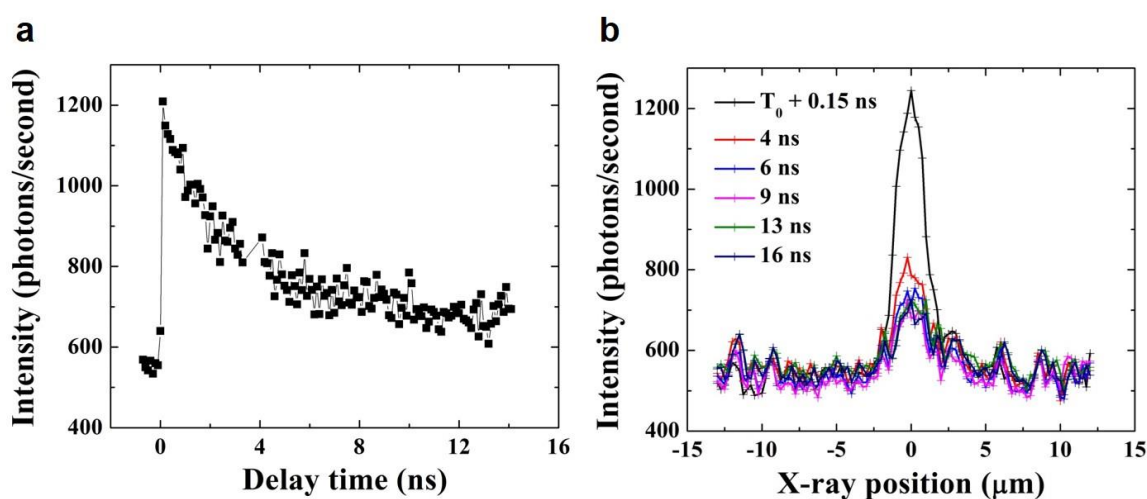
Figure 4-8: (a) Delay scan acquired in the region of spatial overlap of the focused laser and x-ray pulses. (b) Spatial relaxation of the photoinduced lattice dynamics at various delay times from 0.15 ns to 16 ns.

4.5   Conclusion

Combining ultrafast optical excitation with X-ray nanobeam diffraction enables the study of picosecond photoinduced structural dynamics in micron-scale excited regions. A micron-scale focused optical beam requires far less power than an unfocused optical excitation and thus thermal stability is sufficient for synchrotron X-ray nanobeam experiments. Experiments with focused optical excitation show that the photoinduced dynamics in isolated regions of a BFO thin film are consistent with previous area-averaged measurements. Generally, the low optical power required to reach high fluences allows experiments to be conducted without heating large areas of the sample. The combination of a tightly focused optical pump with X-ray nanobeam diffraction has potential future applications in the characterization of optical excitation of isolated regions within lithographically patterned structures and heterogeneous electronic materials.

4.6   References for chapter 4

[1]   B. Kundys, Appl. Phys. Rev. **2**, 011301 (2015).

[2]   B. Kundys, M. Viret, D. Colson, and D. O. Kundys, Nat. Mater. **9**, 803 (2010).

[3]   M. Chergui and A. H. Zewail, ChemPhysChem **10**, 28 (2009).

[4]   D. Schick, M. Herzog, H. Wen, P. Chen, C. Adamo, P. Gaal, D. G. Schlom, P. G. Evans, Y. Li, and M. Bargheer, Phys. Rev. Lett. **112**, 097602 (2014).

[5]   H. Wen, P. Chen, M. P. Cosgriff, D. A. Walko, J. H. Lee, C. Adamo, R. D. Schaller, J. F. Ihlefeld, E. M. Dufresne, D. G. Schlom, P. G. Evans, J. W. Freeland, and Y. Li, Phys. Rev. Lett. **110**, 037601 (2013).

[6]   D. Daranciang, M. J. Highland, H. Wen, S. M. Young, N. C. Brandt, H. Y. Hwang, M. Vattilana, M. Nicoul, F. Quirin, J. Goodfellow, T. Qi, I. Grinberg, D. M. Fritz, M. Cammarata, D. Zhu, H. T. Lemke, D. A. Walko, E. M. Dufresne, Y. Li, J. Larsson, D. A. Reis, K. S. Tinten,

K. A. Nelson, A. M. Rappe, P. H. Fuoss, G. B. Stephenson, and A. M. Lindenberg, Phys. Rev. Lett. **108**, 087601 (2012).

[7]   P. Ruello, T. Pezeril, S. Avanesyan, G. Vaudel, V. Gusev, I. C. Infante, and B. Dkhil, Appl. Phys. Lett. **100**, 212906 (2012).

[8]   G. Sha, A. Cerezo, and G. D. W. Smith, Appl. Phys. Lett. **92**, 043503 (2008).

[9]   E. G. Gamaly, N. R. Madsen, M. Duering, A. V. Rode, V. Z. Kolev, and B. Luther-Davies, Phys. Rev. B **71**, 174405 (2005).

[10]   A. K. Sharma and R. K. Thareja, J. Appl. Phys. **98**, 033304 (2005).

[11]   S. Tao, R. L. Jacobsen, and B. X. Wu, Appl. Phys. Lett. **97**, 033304 (2010).

[12]   G. Heise, D. Trappendreher, F. Ilchmann, R. S. Weiss, B. Wolf, and H. Huber, J. Appl. Phys. **112**, 013110 (2012).

[13]   G. Catalan and J. F. Scott, Adv. Mater. **21**, 2463 (2009).

[14]   D. A. Walko, B. W. Adams, G. Doumy, E. M. Dufresne, Yuelin Li, A. M. March, A. R. Sandy, Jin Wang, Haidan Wen, and Yi Zhu, AIP Conf. Proc. **1741**, 030048 (2015).

[15]   F. Pfeiffer, C. David, J. F. van der Veen, and C. Bergemann, Phys. Rev. B **73**, 245331 (2006).

[16]   C. G. Schroer, Phys. Rev. B **74**, 033405 (2006).

[17]   H. Mimura, H. Yumoto, S. Matsuyama, Y. Sano, K. Yamamura, Y. Mori, M. Yabashi, Y. Nishino, K. Tamasaku, T. Ishikawa, and K. Yamauchi, Appl. Phys. Lett. **90**, 051903 (2007).

[18]   J. Park, Q. Zhang, P. Chen), M. P. Cosgriff, J. A. Tilka, C. Adamo, D. G. Schlom, H. Wen, Y. Zhu, and P. G. Evans, Rev. Sci. Instrum. **86**, 083904 (2015).

[19]   A. M. March, A. Stickrath, G. Doumy, E. P. Kanter, B. Krässig, S. H. Southworth, K. Attenkofer, C. A. Kurtz, L. X. Chen, and L. Young, Rev. Sci. Instrum. **82**, 073110 (2011).

[20]   T. Ejdrup, H. T. Lemke, K. Haldrup, T. N. Nielsen, D. A. Arms, D. A. Walko, A. Miceli, E. C. Landahl, E. M. Dufresne, and M. M. Nielsen, J. Synchrotron Rad. **16**, 387 (2009).

[21]   T. Graber, S. Anderson, H. Brewer, Y.-S. Chen, H. S. Cho, N. Dashdorj, R. W. Henning, I. Kosheleva, G. Macha, M. Meron, R. Pahl, Z. Ren, S. Ruan, F. Schotte, V. Srajer, P. J. Viccaro, F. Westferro, P. Anfinrud, and K. Moffat, J. Synchrotron Rad. **18**, 658 (2011).

[22]   F. Mitschke, *Fiber Optics: Physics and Technology* (Springer, Heidelberg, 2010), Springer.

[23]   Y. Zhao, H. Nakamura, and R. J. Gordon, Biomed. Opt. Exp. **1**, 1159 (2010).

[24]   A. Kumar, R. C. Rai, N. J. Podraza, S. Denev, M. Ramirez, Y. Chu, L. W. Martin, J. Ihlefeld, T. Heeg, J. Schubert, D. G. Schlom, J. Orenstein, R. Ramesh, R. W. Collins, J. L. Musfeldt, and V. Gopalan, Appl. Phys. Lett. **92**, 121915 (2008).

[25]   R. J. Sichel, A. Grigoriev, D. H. Do, S. H. Baek, H. W. Jang, C. M. Folkman, C. B. Eom, Z. H. Cai, and P. G. Evans, Appl. Phys. Lett. **96**, 051901 (2010).

Chapter 5: Dynamics of the photoinduced domain transformation in ferroelectric/dielectric superlattices

5.1 Introduction

The optical illumination of ferroelectrics and related polar materials provides a new way to probe fundamental phenomena related to their polarization and can eventually provide a new way to manipulate their properties. There have been several previous observations of the changes in the structure, domain pattern, and electronic properties of ferroelectric materials under optical illumination. The effects associated with optical excitation can, for example, lead to changes in the dielectric permittivity and to the emergence of new domain structures at the domain boundaries [1,2]. These optically excited domain effects are reversible when the ferroelectric is cycled between illuminated and dark conditions [1-3]. The domains can have complex ultrafast time dependence following ultrafast pulsed optical excitation [4].

The ferroelectric remnant polarization of $PbTiO_3$/$SrTiO_3$ (PTO/STO) ferroelectric/dielectric superlattice (SL) thin films spontaneously forms an intricate nanoscale polarization domain pattern with nanometer-scale periodicity [5,6]. In thin film SLs with few-nm repeating unit thicknesses the period of the striped nanodomains is on the order of 10 nm [7]. An optically-driven domain transformation has been observed in which the initial striped nanodomains transform to a uniform polarization state by a depolarization field screening effect [8]. The electrostatic energy of the thin film is increased by internal electric fields arising from spontaneous polarizations, which is called depolarization fields. As discussed in more detail in Chapter 3, polarization domains form to reduce the electrostatic energy to ultimately lower the total free energy.

When the film is illuminated by an above-bandgap optical beam, the charge carriers are excited. The depolarization field is screened by these additional charges. Then the uniform polarization state becomes energetically favorable than the nanodomains because forming domains also costs energy. After the end of illumination, the uniform polarization state again transform back to the striped nanodomains, which is called domain recovery in this chapter. In PTO/STO SLs, the recovery takes a period of seconds after the end of illumination at room temperature [8]. We hypothesized that the slow recovery dynamics arise from the trapping of optically excited charge carriers at defects and interfaces within the SLs [8]. But this hypothesis and its consequences for optically induced phenomena have not yet been tested.

In this chapter, we report a mechanism of photoinduced domain transformation in PTO/STO SLs based on a charge trapping model. Synchrotron x-ray nanodiffraction measurements show that the rates of domain transformation and recovery vary by orders of magnitude depending on the temperature and optical intensity. The charge trapping model predicts the domain transformation and recovery that depend on the accumulation of trapped charges, and the modeled results are consistent with the measured data. The transformation time from the striped nanodomains to the uniform polarization state is reduced, for example, by a factor of 5 when the optical intensity is increased from 58 mW cm^{-2} to 145 mW cm^{-2}. The recovery time after the end of the illumination depends on the temperature and is dramatically faster at elevated temperatures.

5.2   Experimental setup

X-ray nanodiffraction experiments were conducted at station 7-ID-C of the Advanced Photon Source of Argonne National Laboratory. The X-ray beams with a photon energy of 11 keV were focused to a spot with 500 nm full width at half maximum (FWHM) using a 160 µm-diameter
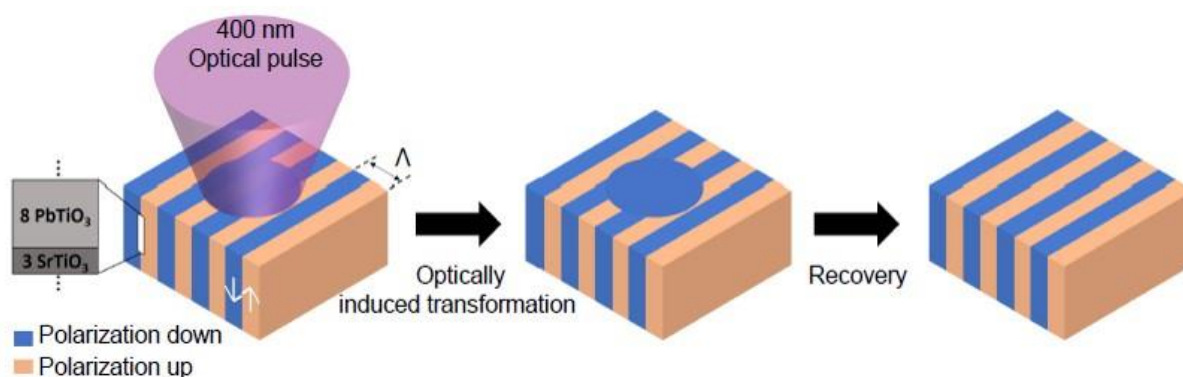
Figure 5-1: Schematic of domain transformation in PTO/STO SLs. The initial striped nanodomains contain up (beige) and down (blue) polarizations with its periodicity Λ. Optical illumination with a wavelength of 400 nm induce the domain transformation from the initial striped nanodomains to a uniform polarization state. After the end of illumination, the striped nanodomains is recovered.

Fresnel zone plate. The higher orders of the focused beams was attenuated by a 60 µm-diameter center stop. Unfocused beams also were attenuated by an order sorting aperture. A pixel array detector (Pilatus 100 K, Dectris, Ltd.) with 172 µm pixels was used to collect the diffraction patterns at a nominal *2θ* angle of 32.6° for a diffraction condition near the 0th order 002 PTO/STO SLs Bragg reflection. The Bragg angle θ_B is 16.3°. The X-ray beam was spatially overlapped on the sample surface with the optical beam. The wavelength and repetition rate were 400 nm (3.1 eV) and 1 kHz, respectively. The optical beam energy was higher than the theoretical optical band gaps of PTO and STO, 2.3 and 2.8 eV [9]. The spot size of the optical beam was 190 µm FWHM, and its incident angle was 90° with respect to the sample surface before rotating the sample to the Bragg angle. The PTO/STO SLs thin film consisting of 8 unit cells of PTO and 3 unit cells of STO was deposited using off-axis radio-frequency sputtering. The SL repeating unit was repeated 23 times, deposited on a $SrRuO_3$ (SRO) thin film on a (001)-oriented STO substrate.

5.3   Photoinduced nanodomain domain transformation

Figure 5-1 schematically illustrates the optically induced domain transformation in PTO/STO SLs from the initial striped nanodomains to a uniform polarization state. The initial

striped nanodomain structure contains the up and down polarizations in the SLs. The average SL lattice constant a_{SL} is 4.016 Å, and the domain period Λ is 8.7 nm. The photoinduced domain transformation is induced by 400 nm optical illumination. The polarization in the uniform polarization state is expected to be a down polarization. The direction of polarization by the extra charges can be determined by an extra internal electric field resulting from the trapped charge distributions at interfaces or domain walls [10-12]. After the end of illumination, the transformed region reversibly undergoes the recovery..

The structural changes in SLs lattices, domain orientation, and domain period appear in reciprocal space as shown in Figure 5-2. The photoinduced domain transformation is accompanied by a lattice expansion [13,14] and domain intensity disappearance. Before the optical illumination, the 002 SL Bragg reflection locates at $Q_z = 3.13$ Å^{-1}, and the domain diffuse scattering intensity appears in a ring shape on the Q_x-Q_y plane around the SL Bragg reflection with the radius ΔQ of 0.072 Å^{-1}. The domain ring intensity arises from the repetition of up and down polarizations formed in the striped nanodomains. Two key phenomena can be observed after the optically
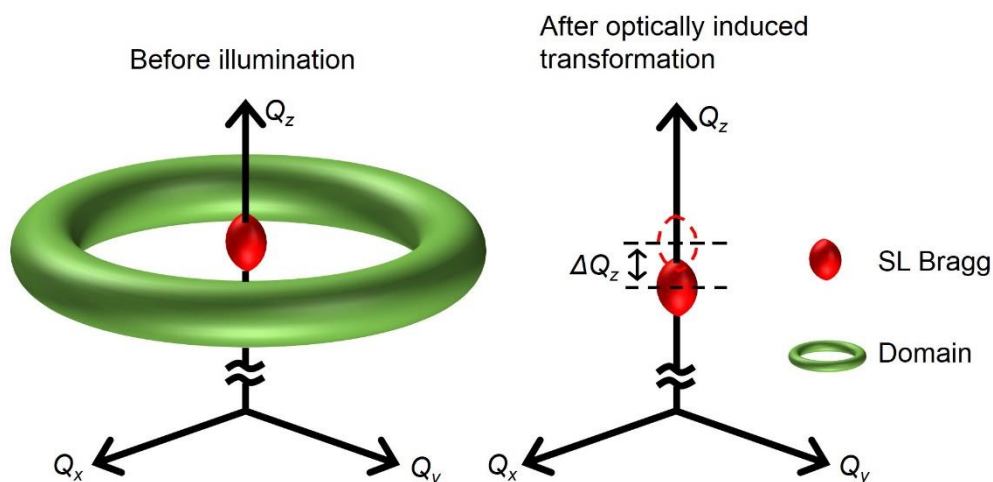
Figure 5-2: SL Bragg reflection (red) and domain diffuse scattering intensity (green) in reciprocal space. After the transformation, the SL Bragg reflection shift to a lower value of Q_z by ΔQ_z, and the domain intensity disappears.

induced transformation. The domain diffuse scattering disappears because the striped nanodomains transform to the uniform polarization configuration. The disappearance of the nanodomain pattern leads to an increase in the polarization and a shift of the structural Bragg reflection shifts to lower Q_z by wavevector ΔQ_z. The recovery of the nanodomain pattern after the end of illumination leads to a reappearance of the domain pattern and a return of the lattice parameter to its initial value.

5.3.1 Photoinduced lattice expansion
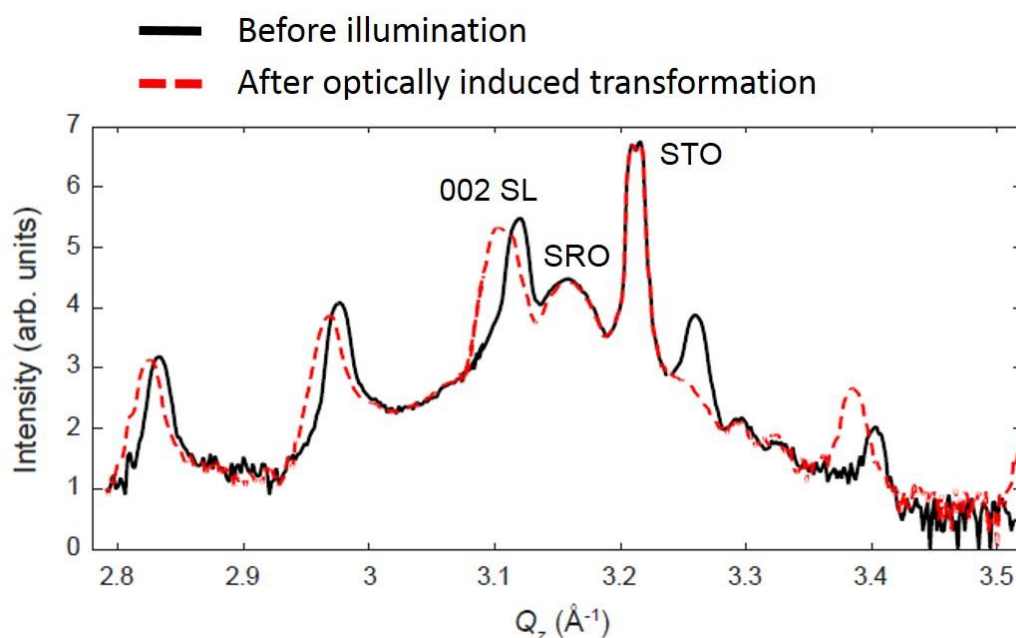
Figure 5-3: 002 Bragg reflection as a function of Q_z before optical illumination (solid) and after optically induced domain transformation (dashed). The Bragg STO and SRO reflections do not move but the SL Bragg reflections shift to a lower value of Q_z because of the photoinduced lattice expansion.

X-ray diffraction experiments were conducted to measure the Bragg reflections from SLs, SRO, and STO layers. Figure 5-3 shows Bragg intensities around the 002 SL reflection as a function of Q_z ranging from 2.8 Å^{-1} to 3.5 Å^{-1} before optical illumination and after optically induced domain transformation. When the domain transformation is completed after optical

illumination, the SL Bragg reflections shift to lower values of Q_z because of the photoinduced

lattice expansion but the STO and SRO reflections do not shift.
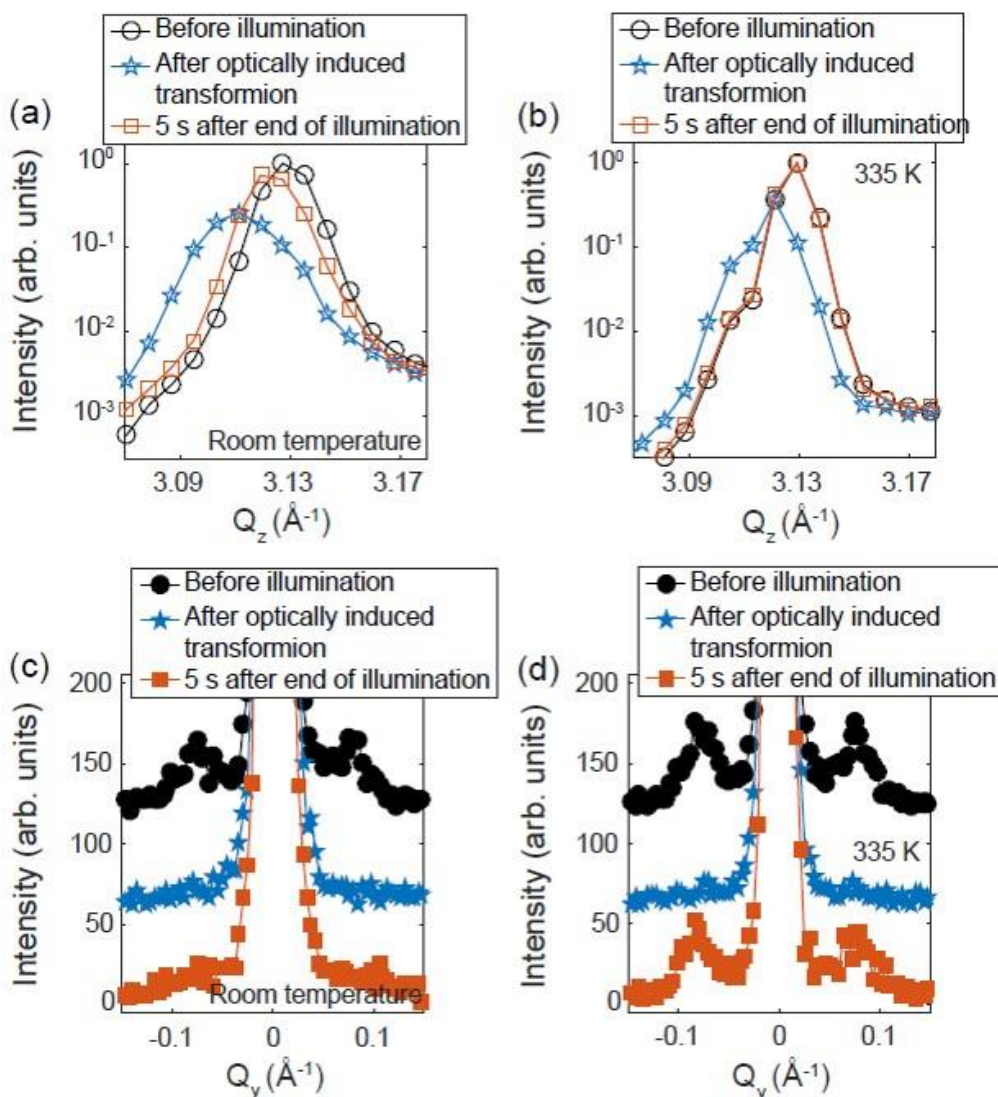
Figure 5-4: (a and b) Scattered x-ray intensities for SL Bragg reflections measured at room temperature and 335 K are plotted as a function of Q_z. Between the three cases, ΔQ_z indicates that the recovery is completed only at 335 K within 5 s after the end of illumination. (c and d) Domain intensities measured at room temperature and 335 K are plotted as a function of Q_y. Domain intensity disappears after the transformation and the recovery is completed only at 335 K within 5 s after the end of illumination.

A comparison of the dynamics for the structures at two temperatures with a single

illumination intensity (58 mW cm^{-2}) is shown in Figures 5-4. X-ray diffraction patterns were

collected for the 002 SL Bragg reflections to study the temperature dependence of the structural

changes. The diffraction patterns were acquired at the nominal Bragg angle for three different

cases: (i) before illumination, (ii) after optically induced transformation, and (iii) 5 s after the end of illumination. Figure 5-4(a) shows the Bragg reflections of these cases measured at room temperature as a function of Q_z ranging from 3.07 Å^{-1} to 3.18 Å^{-1}. The intensities were normalized by the peak intensity of the before illumination case. The Bragg reflection appears at $Q_z = 3.13$ Å^{-1} before illumination, which shifts to a lower value of Q_z by $\varDelta Q_z = 0.02$ Å^{-1} after transformation. This shift corresponds to a 0.6% lattice expansion. More detailed discussion regarding the lattice strain is provided in Section 5.6.1. The integrated intensity of the Bragg reflection deceases by a factor of 2, and the width is broadened by a factor of 1.5 after transformation. The broadened width may originate from a photoinduced inhomogeneous strain profile along thickness direction [13,15]. The Bragg reflections were again measured 5 s after the end of illumination. They shift back to a higher value of Q_z only by 67%, which indicates that it is still during the recovery.

The same sets of experiments were repeated at 335 K as shown in Figure 5-4(b). In comparison with the room temperature data, a 0.06% contraction was observed before illumination in which the position of 002 SL Bragg reflection appears 0.001 Å^{-1} higher in Q_z. This value is similar to a thermal contraction of 0.09%, which has been previously measured at 335 K [8,16,17]. After transformation, the Bragg reflection shifts to a lower value of Q_z by $\varDelta Q_z = 0.01$ Å^{-1}. The integrated intensity still deceases by a factor of 2, and the width is broadened by a factor of 1.5. Unlike room temperature, 5 s after the end of illumination, the Bragg reflection shifts completely back to the initial Q_z, indicating that the recovery is completed within 5 s after the end of illumination.

5.3.2 Disappearance of domain diffuse scattering

While acquiring the diffraction patterns for the Bragg reflections, the domain intensities were also measured at the same time. The domain intensities can be plotted as a function of Q_y ranging from -0.15 Å^{-1} to 0.15 Å^{-1} as shown in Figures 5-4(c) and 5-4(d). The cropped intensity at zero-Q_y is from the SL Bragg reflection intensity. The domain intensities are plotted with an offset (60 arb. units) to clearly see the differences. The domain intensity appears on top of the tail of the SL Bragg reflection at $Q_y = \pm0.072$ Å^{-1} before illumination. After transformation, the domain intensity completely disappears. Domain intensity measured 5 s after the end of illumination shows that 28% of domain intensity is recovered. This is much slower than the lattice relaxation. The same sets of X-ray diffraction experiments were repeated at 335 K to measure the domain intensity. After transformation, the domain intensity still disappears as shown in Figure 5-4(d), but it recovers back to the initial intensity 5 s after the end of illumination. This fast recovery time at higher temperature indicates that the recovery is thermally accelerated.

5.4 Optical intensity dependence of domain transformation

X-ray diffraction experiments with different optical intensities were conducted to study the optical intensity dependence of domain transformation. During the experiments, changes in Bragg reflection position and domain intensity were measured. Figure 5-5(a) shows changes in ΔQ_z as a function of time after the end of illumination. 46 mW cm^{-2}, 58 mW cm^{-2}, and 145 mW cm^{-2} optical intensities were used. The data in the first three panels was acquired at room temperature. The shaded region is placed in the negative time for 25 s representing the light was on. During the illumination at room temperature, ΔQ_z increases due to the photoinduced lattice expansion. The lattice relaxes for a period of seconds after the end of illumination. The change in ΔQ_z at 46 mW
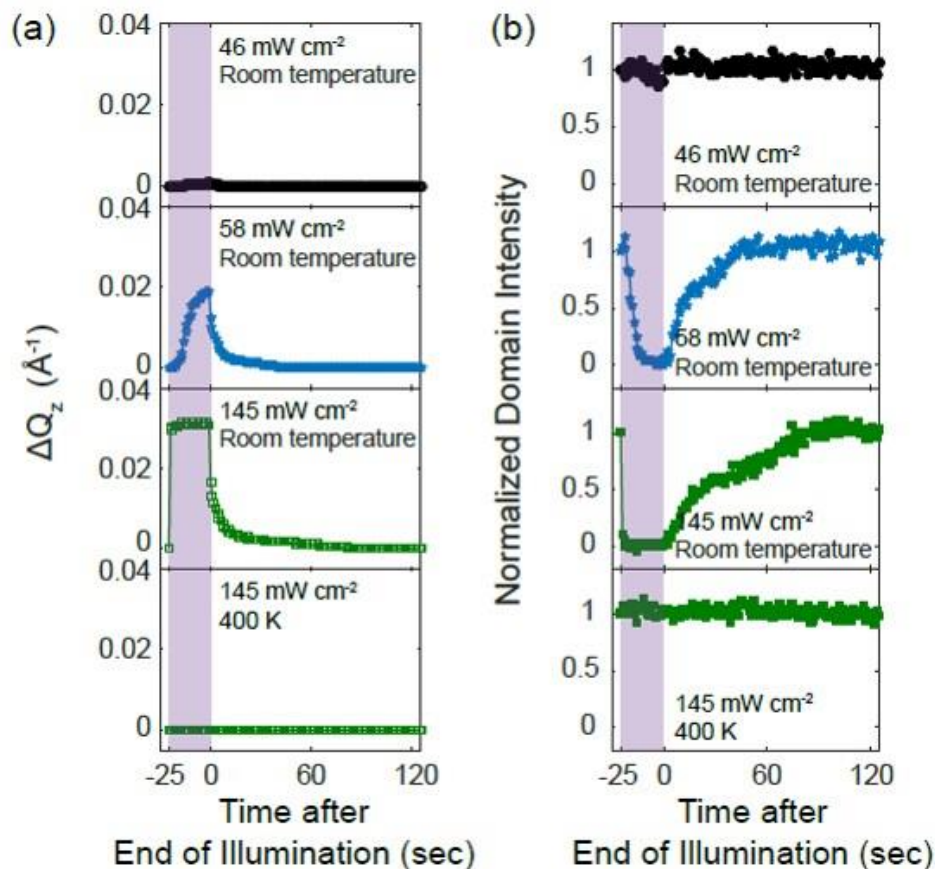
Figure 5-5: Changes in (a) ΔQ_z and (b) domain intensities as a function of time after the end of illumination, showing an optical intensity dependence of domain transformation. The data in first three panels and last panel was obtained at room temperature and 400 K. Optical intensities were 46 mW cm^{-2}, 58 mW cm^{-2}, and 145 mW cm^{-2}. The shaded region represents 25 s of optical illumination.

cm^{-2} for 25 s of illumination is negligibly small. The ΔQ_z at 58 mW cm^{-2} gradually increases for

25 s until it reaches 0.02 Å^{-1} after transformation. The ΔQ_z at 145 mW cm^{-2} increases up to 0.03

Å^{-1} within a few seconds of illumination and saturates at the same value for the rest of illumination.

The same experiment was performed at 400 K and 145 mW cm^{-2} optical intensity as shown in the

last panel but the change is not as apparent as the room temperature data.

For the optical intensity dependence experiments, the domain intensities were also measured

at the same time while acquiring the Bragg reflections. Figure 5-5(b) shows changes in normalized

domain intensity as a function of time after the end of illumination. The data in the first three

panels were acquired at room temperature. During the illumination, the domain intensity decreases

due to the domain transformation. For 25 s of illumination, the decrease in domain intensity at 46 mW cm^{-2} is 12.5 %, while 90% of domain transformation takes 11.5 s at 58 mW cm^{-2}, which becomes faster down to 2 s at 145 mW cm^{-2}. The recovery takes for a period of seconds after the end of illumination. The same experiment was performed at 400 K as shown in the last panel but the change is not as apparent as the room temperature data even at 145 mW cm^{-2} optical intensity.
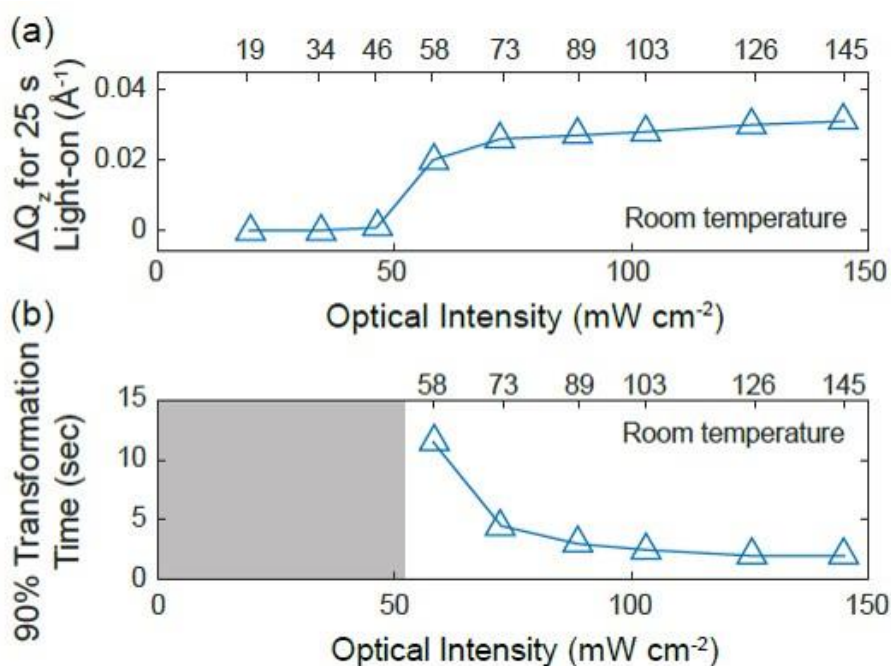
Figure 5-6: (a) Maximum ΔQ_z obtained for 25 s of illumination (light-on) as a function of optical intensity ranging from 19 mW cm^{-2} to 145 mW cm^{-2}. The slight change of ΔQ_z starts to show up from 46 mW cm^{-2} and it saturates at 145 mW cm^{-2}. (b) 90% transformation time as a function of optical intensity ranging from 19 mW cm^{-2} to 145 mW cm^{-2}. The transformation time was not observed with optical intensity lower than 58 mW cm^{-2}.

The maximum ΔQ_z achieved for 25 s of illumination at room temperature is plotted as a function of the optical intensity in Figure 5-6(a). The optical intensity ranges from 19 mW cm^{-2} to 145 mW cm^{-2} mW. No change in ΔQ_z was observed after 25 s of illumination with laser intensities lower than 34 mW cm^{-2}. The change in ΔQ_z appears from 46 mW cm^{-2}, and it saturates to 0.03 Å^{-1} at 145 mW cm^{-2}. From the data shown in Figure 5-5(a) and 5-5(b), the domain intensity decreases down to zero when ΔQ_z reaches to 0.02 Å^{-1}.

An additional key feature of Figure 5-5(a) is that ΔQ_z keeps increasing until it saturates to 0.03 Å^{-1}. This indicates that there is a threshold number of trapped charges that induces the domain transformation, which is not sufficient for the full depolarization field screening. Here, ΔQ_z for the threshold to induce the domain transformation is 0.02 Å^{-1}. The charges can be trapped more until the depolarization is fully screened in which the ΔQ_z reaches its saturation at 0.03 Å^{-1}. The threshold ΔQ_z is 66% of the saturated ΔQ_z, which is consistent with the LGD calculation showing the increase in polarizations as a function of screening efficiency. More detail discussion is proved in Section 5.6.2. In the calculation, the down polarization keeps increasing as the screening efficiency increases even after the up polarization disappears at the threshold. The 90% of domain transformation time measured at room temperature is plotted as a function of the optical intensity ranging from 19 mW cm^{-2} to 145 mW cm^{-2} in Figure 5-6(b). The transformation time was observed for the laser intensities lower than 58 mW cm^{-2} because the transformation did not occur. The experiment measuring changes in domain intensity as a function of time after the end of illumination at 400 K is shown in the last panel of Figure 5-6(b). Although the optical intensity 145 mW cm^{-2} was used but the domain intensity does not change.

5.5 Temperature dependence of domain recovery

For a systematic evaluation of the recovery of the SL Bragg reflection wavevector and the domain diffuse scattering intensity, x-ray diffraction experiments were conducted to study a real-time recovery dynamics by measuring changes in positions of SL Bragg reflection and the domain intensity at room temperature, 310, and 335 K. Before measuring these changes, the sample was optically illuminated at 58 mW cm^{-2} until the domain transformation was completed. The completion of domain transformation was verified by the zero-domain-intensity. Figure 5-7(a) shows changes in ΔQ_z at each temperature as a function of time after the end of illumination for

120 s. The shift in the wavevector of the Bragg reflection was measured by fitting the diffraction patterns with a Gaussian peak to measure ΔQ_z. The shift of Bragg reflection ΔQ_z is 0.02 Å^{-1} at room temperature, and its extent becomes smaller at higher temperatures, for example, ΔQ_z at 335 K is 0.008 Å^{-1}. The relaxation of ΔQ_z also depends on the temperature, which becomes faster at higher temperatures. These observations are assumed to be related to the total number of trapped charges depending on temperature. At higher temperatures, the de-trap processes are accelerated and the total number of trapped charges becomes less than lower temperatures. Thus, the saturated ΔQ_z becomes small and the recovery is accelerated at higher temperatures.
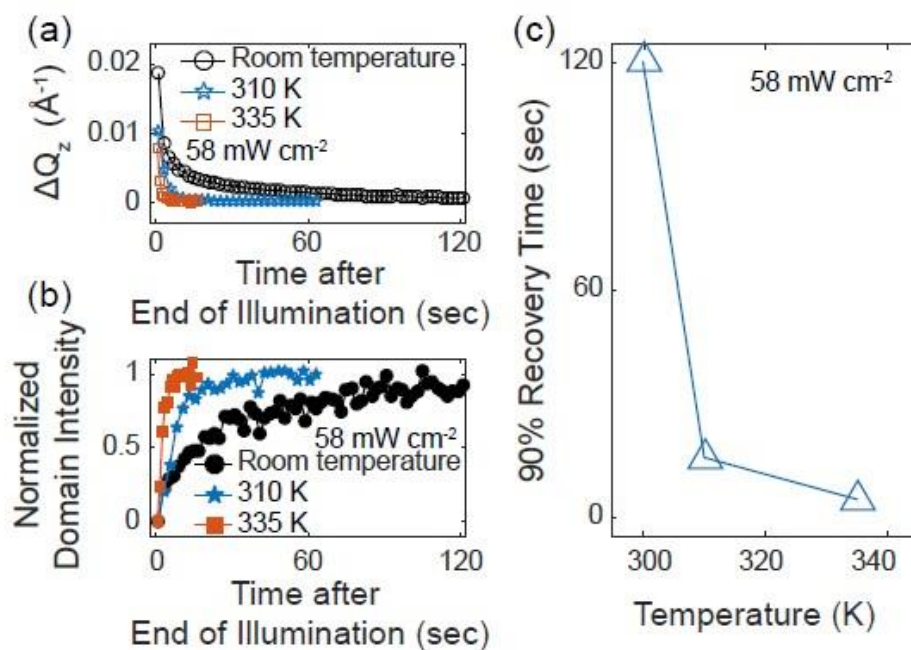
Figure 5-7: ΔQ_z and domain intensity during recovery were measured. Before the measurement, the sample was optically illuminated at 58 mW cm^{-2} until the domain intensity disappeared. (a and b) ΔQ_z and domain intensities measured at room temperature (circle), 310 (star), and 335 K (square) are plotted as a function of time after the end of illumination. The domain intensities are normalized by their initial intensity. (c) 90% recovery time is plotted as a function of temperature showing that the recovery time becomes faster at higher temperatures.

Figure 5-7(b) shows the domain recovery intensity as a function of time after the end of illumination. The domain intensities are normalized by their initial domain intensities measured at each temperature. At high temperatures, the recovery is thermally accelerated and becomes faster than room temperature, which might contribute to the enhanced photocurrent [18,19]. The domain

intensity recovery times are plotted in Figure 5-7(c) as a function of temperature. The 90% of the domain intensity recovery time is 120 s at room temperature and it deceases down to 5 s at 335 K. Over 340 K, it was impossible to measure the recovery time because the recovery was completed much faster than the laser repetition time of 1 ms. The disappearance of domain intensity was not observed by the real-time x-ray diffraction experiment.

5.6   Charge trapping model

The charge trapping model together with a heterogeneous domain transformation model predicts changes in domain intensity during the domain transformation and recovery at various intensities and temperatures. This combination of models is a new means to describe the photoinduced domain transformation without considering the domain wall motion.

5.6.1   Microscopic heterogeneous domain transformation model

We propose a microscopic heterogeneous domain transformation model. It is assumed that the trap energies would not be uniform across the film. The moment of domain transformation spatially varies depending on trap energies. Thus, the above-bandgap optical illumination results in local domain transformations, which is spatially separated from the un-transformed regions. The entire optically illuminated region eventually reaches a homogenous uniform polarization state when the domain transformation for the entire illuminated region is completed. The key predictions of the model are (i) the lattice constant expands by the depolarization screening effect. The measured average lattice constant within the optically illuminated region therefore would gradually increase as the size of the transformed area increases. (ii) The domain transformation time would become faster when using higher optical intensities because the number of trapped

charges by one optical pulse becomes greater with higher intensities. (iii) At higher temperatures, the de-trapping rate becomes faster than the optical pulse repetition time of 1 ms.
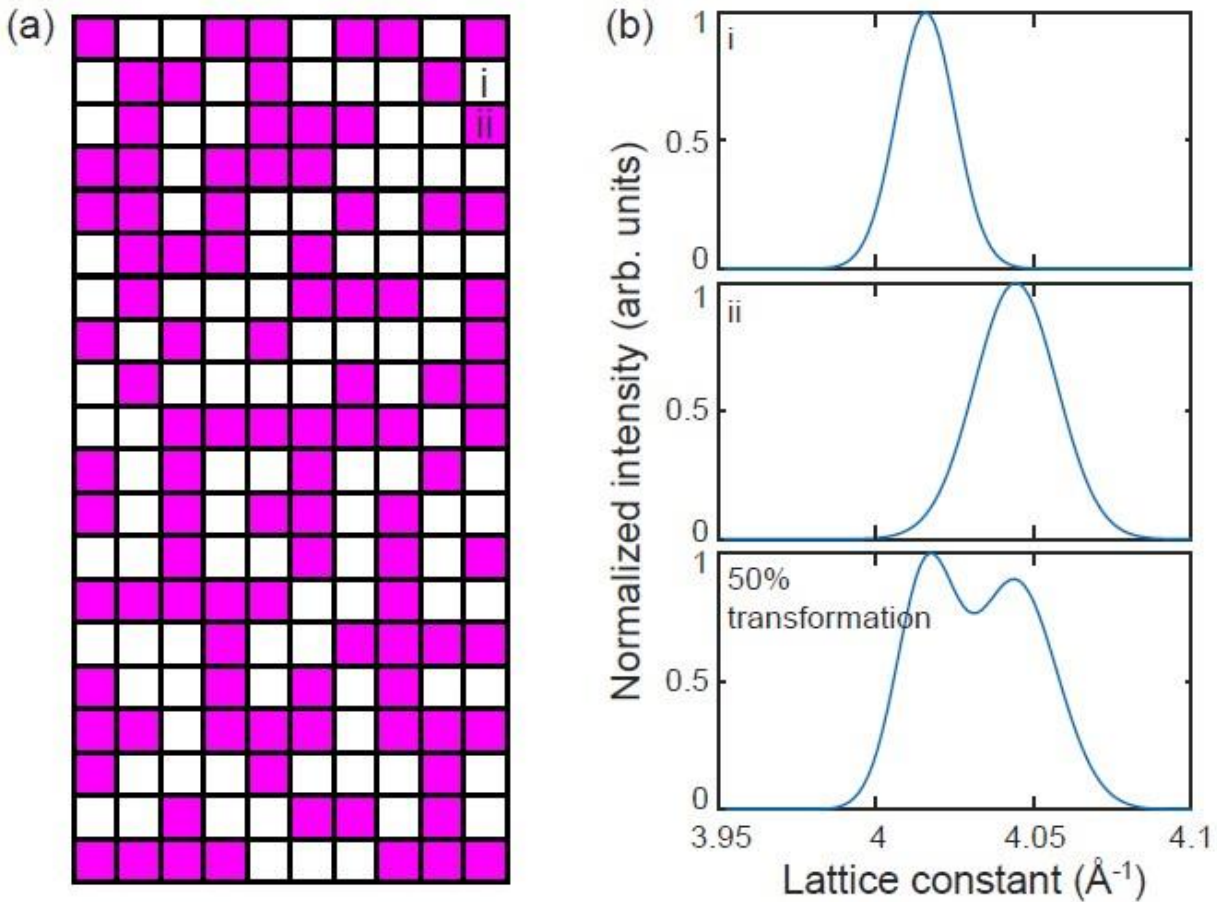
Figure 5-8: (a) Schematic of microscopic heterogeneous domain transformation model. 10 × 20 matrices are assumed to be the optically illuminated area consisting both (i) untransformed (white) and (ii) transformed (magenta) sites. Particularly, it exhibits a case when 50% of the area is transformed. (b) Simulated distributions of SL lattice constants based on the model. Simulated parameters are such that, (i) in the untransformed region, the SL lattice constant is 4.016 Å with its variation of 0.023 Å (W_Q = 0.017 Å^{-1}) (ii) in the untransformed region, the lattice is set to be 4.044 Å (0.7% strain) with its variation of 0.033 Å. The last panel shows the averaged lattice constant from the entire area.

Shift of the position of SL Bragg reflection to lower value of Q_z indicates the film is strained. The tensile strain can be calculated using a relationship $\varepsilon = \dfrac{\lambda \cot(\theta_B)\, \Delta Q z}{4\,\pi}$, where λ is the x-ray wavelength and θ_B is the Bragg angle. As shown in Figure 5-5(a), ΔQ_z of 0.02 Å^{-1} corresponds to the expansion of 0.6% at 58 mW cm^{-2} optical intensity. The corresponding initial and final lattice constants are 4.016 Å and 4.044 Å. The Bragg peak width also increase while the lattice expands.

To understand the change of the Bragg peak poistion (lattice strain), the microscopic heterostructure domain transformation model is simulated. 200 optically illuminated sites are assumed to exist with different trap energies. The moments of domain transformation are, therefore, different site by site. Figure 5-8(a) shows a 10×20 site matrix consisting of the (i) 100 untransformed and (ii) 100 transformed sites. Figure 5-8(b) shows the simulation results regarding distributions of lattice constant at one site of (i) untransformed, (ii) transformed in the first two panels. The value of strain in the transformed regions is 0.7%. The lattice constants of the untransformed and transformed regions were assumed to be 4.016 Å and 4.044 Å, respectively. The last panel shows the total distribution of lattice constant from the 200 sites for which the domain transformation is completed 50%.
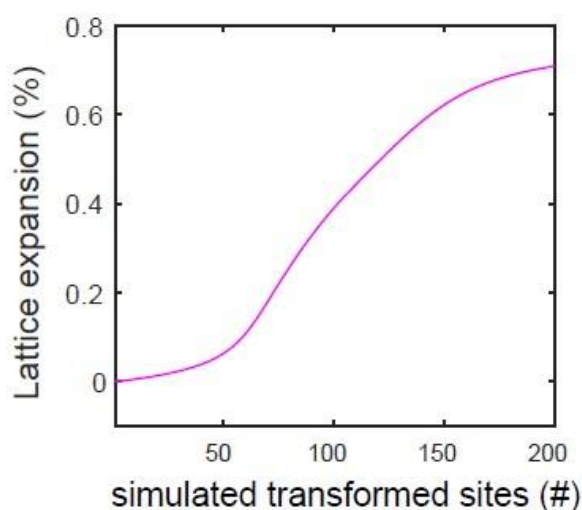
Figure 5-9: Simulation results of change in SL lattice expansion showing that the lattice gradually increases as the lattice constant is set to be 0.7% greater than its initial when the transformation is completed.

Figure 5-9 shows the simulation results of the SL lattice expansion as a function of the number of transformed sites. The Bragg peak width also gradually increases as both distributions of lattice constant for untransformed and transformed sites coexist (data not shown). It is inappropriate to compare these results to the data in Figure 5-5(a) because it is hard to directly

convert the simulated number of transformed sites to the laser exposure time. Therefore, the simulated number of transformed sites are manually selected for the proper comparison as plotted in Figure 5-10.
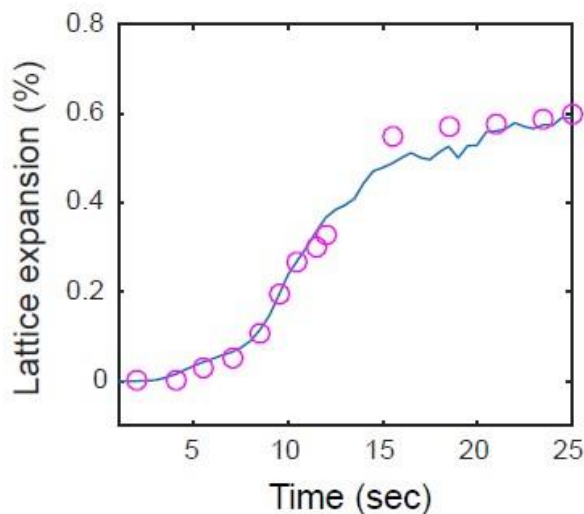
Figure 5-10: Comparison between the measured data (blue curves) and selected simulation results (magenta circles) of change in SL lattice expansion. The measurements are under optical illumination for 25 seconds, and the number of transformed sites are chosen and plotted in the circles. The measured data and the selected simulation results agree well that the lattice gradually increases.

Figure 5-10 shows the comparison between the measured data and selected simulation results of lattice expansion at 58 mW cm^{-2}. The measured data is plotted as a function of illumination time. The number of transformed sites are manually selected and plotted in circles. The selected number of transformed sites are 1, 7, 35, 47, 60, 72, 81, 86, 90, 132, 136, 138, 140, and 144 with the corresponding time of 2, 4, 5.5, 7, 8.5, 9.5, 10.5, 11.5, 12, 15.5, 18.5, 21, 23.5, and 25 seconds. Overall, the selected simulation results agree well with the measured data.

5.6.2 Landau-Ginsburg-Devonshire calculation

We have hypothesized that the domain transformation is linked to the screening of the depolarization field by effects of the above-bandgap illumination. A Landau-Ginsburg-Devonshire (LGD) model was used to evaluate the total free energy density as a function of screening

efficiency. In the calculation, ferroelectric/dielectric SLs consisting of 8-unit-cell PTO, and 3-unit-

cell SrTiO$_3$ (STO) as an SL repeating unit is considered. The lattice constant of PTO, ζ_{PTO} is 3.9%

larger than that of STO (3.905 Å). The thickness of each layer is t_{PTO} = 8 ζ_{PTO} and t_{STO} = 3ζ_{STO}.

The average lattice constant ζ_{SL} of SL is therefore $\frac{t_{PTO}+t_{STO}}{8+3}$ = 4.016 Å, and the volume fraction

of each layer α_l is $\alpha_l = \frac{t_l}{t_{PTO}+t_{STO}}$. The free energy density is calculated considering the

ferroelectric polarization in each layer as the order parameter. The total free energy density

contributions consist of bulk, depolarization field, and external electric field. In the model, the

depolarization field screening effect is considered in which the depolarization field vanishes as

screening efficiency increases. The screening efficiency ranges from 0 to 1, and the depolarization

field is considered to be fully screened when the screening efficiency is 1 as discussed in the

supplemental materials of ref. [8]. Similar depolarization screening effects have previously been

studied using thermodynamic models considering extra-charge-carriers-induced electric field

[20,21]. The total free energy density F is written as Eq. 5-1 [20].

$$F = \sum_{l}^{n} \alpha_l f_l - \frac{1}{2}\sum_{l}^{n} \alpha_l (1-\theta)E_l^{Dep}P_l - \sum_{l}^{n} \alpha_l \theta E_l^{ext}P_l$$

Equation 5-1

where f_l is the free energy density of each layer l, with the free-energy density of the polarization-

free high-temperature paraelectric phase f_0, and θ is the screening efficiency.

$$f_l = f_{0,l} + \frac{1}{2}a_l'P_l^2 + \frac{1}{4}b_l'P_l^4 + \frac{1}{6}c_l'P_l^6 + \frac{x_l^2}{s_{11,l} + s_{12,l}}$$

Equation 5-2

Here, P is the polarization, a', b' and c' are the parameters derived from the unconstrained bulk

dielectric stiffness coefficients of a, b, and c, x is the misfit strain, s is the elastic compliance, and

Q is the electrostrictive coefficient as written as Eq. 5-3.

$$a_l' = a_l - x_l \frac{4Q_{12,l}}{s_{11,l}+s_{12,l}}, \text{ and } b_l' = b_l - \frac{4Q_{12,l}}{s_{11,l}+s_{12,l}}, \text{ where } \frac{1}{s_{11,l}+s_{12,l}} = c_{11,l} + c_{12,l} - \frac{2c_{12,l}^2}{c_{11,l}}$$

Equation 5-3

The depolarization field E^{Dep} arises from the polarization discontinuity between the layers

as written as Eq. 5-4 [8], where ε_0 is the permittivity of free space of 8.8542×10^{-12} F/m. The

relative permittivity $\varepsilon_{r,l}$ are tabulated in Table 5-1.

$$E_l^{Dep} = \frac{\alpha_{l+1}(P_{l+1} - P_l)}{\varepsilon_0 \varepsilon_{r,l}}$$

Equation 5-4

The external electric field E^{ext} of -215 MV imitates the situation in which the polarization

direction is determined by the extra electric field when the depolarization field is screened [15].

	PTO	STO
Tc (°C)	479	-253
C (°C)	1.5×10^5	0.8×10^5
a (N m^6/C^4)	$\frac{T - T_{C,PTO}}{\varepsilon_0 C_{PTO}}$	$\frac{T - T_{C,STO}}{\varepsilon_0 C_{STO}}$
b (N m^6/C^4)	-2.92×10^8	8.4×10^9
c (N m^{10}/C^6)	1.56×10^9	
c_{11} (N/m^2)	1.75×10^{11}	3.181×10^{11}
c_{12} (N/m^2)	7.94×10^{10}	1.025×10^{11}
Q_{12} (m^4/C^2)	-0.026	-0.013
ε_r	200	320
ζ (Å)	4.057	3.905
x	$\frac{\zeta_{STO} - \zeta_{PTO}}{\zeta_{STO}}$	0

Table 5-1

Values of the paramters used in the simulation is tabulated in Table 1. T_C and C are the

Curie temperature and constant, respectively. The magnitude of polarization in each layer is

determined by solving $\frac{\partial F}{\partial P_{PTO}} = \frac{\partial F}{\partial P_{STO}} = 0$. The calculated average polarization is $\langle P \rangle = \sum_l^n \alpha_l P_l$.

The magnitude of polarization is also modified by θ as shown in Figure 5-11.
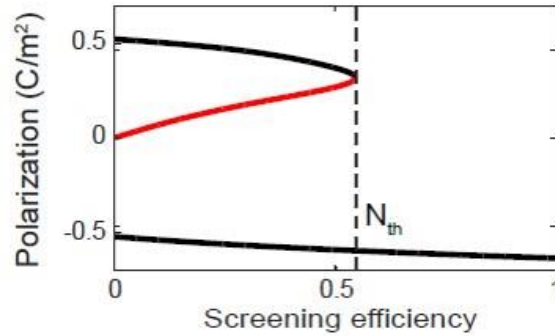
Figure 5-11: Magnitude of the energetically stable polarizations as a function of screening efficiency computed using a Landau-Ginsburg-Devonshire calculation. The initial magnitudes are ±0.52 C/m² representing the initial nanodomains. The zero-polarization is a solution of the calculation but for an unstable polarization state. When the screening efficiency reaches a threshold (N_{th}) the up polarization disappears, which corresponds to the moment of domain transformation.

Figure 5-11 shows the result of calculation plotting the magnitudes of energetically stable

polarization as a function of screening efficiency of θ ranging from 0 to 1, The depolarization field

is screened as θ increases. The up and down polarization states exist when θ is small. As θ increase,

the magnitude of up polarization decreases while that of down polarization increases due to the

existence of E^{ext}. The initial polarization is ±0.52 C/m² at the zero screening efficiency representing

the initial striped nanodomains. The zero-polarization component (red) is a solution of the

calculation but for an unstable polarization state. As the screening efficiency increases, the

magnitude of down polarization increases while the up polarization decreases. Once the screening

efficiency reaches 0.55, the up polarization disappears. The down polarization at this point is -0.56

C/m². This occurs when the amount of charge reaches its threshold (N_{th}), representing a moment

of domain transformation. The down polarization increases until the screening efficiency becomes

unity, and the final magnitude is -0.68 C/m². The tetragonality of the unit cell is defined as the ratio of out-of-plane c to in-plane lattice constants a. The relationship between the tetragonality and the polarization P is $\left(\frac{c}{a} - 1\right) \propto P^2$ [22-24]. In the model, the magnitudes of down polarization for screening efficiencies of 0 and 1, P_0 and P_1 are -0.56 C/m² and -0.68 C/m². The increase in the magnitude of polarization represnets that the c increaes as the depolarization field is screened. In addition, the magnitude of down polarization at threshold P_{th} is -0.64 C/m². Assuming that ε_1 and ε_{th} are the simulated out-of-plane strains for screening efficiencies of 1 and threshold, their ratio $\frac{\varepsilon_{th}}{\varepsilon_1} = \frac{P_{th}^2 - P_0^2}{P_1^2 - P_0^2} = 0.64$ indicates that the lattice expansion at thresold is 64% of the maximum strain with the fully screened depolarization field.

5.6.3 Domain intensity calculation

Based on the results of the LGD calculation, we propose a photoinduced charge trapping model for the domain transformation. The charge carriers are excited by the above-bandgap optical pulses every 1 ms. The charge carriers recombine with recombination time constants on the order of several hundreds of microseconds in ferroelectric thin films [25,26]. A significant population of carriers, however, can be trapped at defects before recombination [27]. Once the number of accumulated charge carriers (N_{accum}) exceeds N_{th}, the domain transformation occurs. Between the optical pulses, the trapped charge carriers are thermally de-trapped. After the end of illumination, the de-trapping process solely occurs and the recovery process begins.

The gradual recovery of the transformation suggests that there is not a single value of the trap energy that applies to the entire PTO/STO thin film. The rate of charge accumulation can vary if the trap energies are not uniform across the film. In this case, transformed regions and untransformed regions coexist in spatially separated regions during the gradual initial

transformation and recovery. We consider the case in which there are a set of different de-trapping times. The moment of domain transformation in a microscopic perspective therefore vary depending on the de-trapping times.

Charge trapping model is based on the existence of deep-level charge traps in the bandgap. The photoexcited charge carriers are trapped in these traps under the above-bandgap optical illumination, and thermally de-trapped after the end of illumination. In this model, it is necessary to estimate the charge emission rate resulting from the de-trapping process. Depending on the trap energy relative to the Fermi energy level, the emission rate of one carrier type among electron and hole dominates while the other can be neglected [28]. The electron emission is considered in the model. The trapping and de-trapping processes of electron are defined as (i) $n\, c_n\, p_T$ for electron trap and (ii) $e_n\, n_T$ for electron emission, respectivley, where n is the electron density in the conduction band, c_n is the electron capture coefficient, p_T is the hole trap density, e_n is the electron emission rate, n_T is the electron trap density, and the total trap density $N_T = n_T + p_T$. At the thermal equilibrium, the charge trap and emission rates are the same ($e_n\, n_T = c_n\, p_T\, n$). Here, e_n can be re-written using the definitions of $n = N_c \exp\frac{E_F - E_C}{k_B T}$ and $n_T = \frac{N_T}{1+\exp\frac{E_t - E_F}{k_B T}}$, where N_c is the density of state in the conduction band of $2\left(\frac{2\,\pi\, m_{eff} k_B\, T}{h^2}\right)^{1.5}$ m^{-3}, E_F is the Fermi energy level, E_C is the conduction band, k_B is Boltzmann's constant of 8.617×10^{-5} eV/K, and T is the temperature. Therefore, $e_n = c_n N_c \exp\left(\frac{E_t - E_C}{k_B T}\right) = \sigma v_{th} N_c \exp\left(\frac{-E_t}{k_B T}\right)$, where σ is the charge capture cross-section on the order of 10^{-24} m^2 [29,30], v_{th} is the electron thermal velocity of $\sqrt{\frac{3 k_B\, T}{m_{eff}}}$ m/s, m_e is the electron mass of 9.11×10^{-31} kg, m_{eff} is its effective mass of 5.78 m_e kg estimated in PbTiO$_3$

(PTO) [31], and h is Plank's constant of 6.626×10^{-34} m^2 kg/s. The rate constant discussed in Figure 5-12 is $\sigma\, v_{th}\, N_c$ s^{-1} [32].
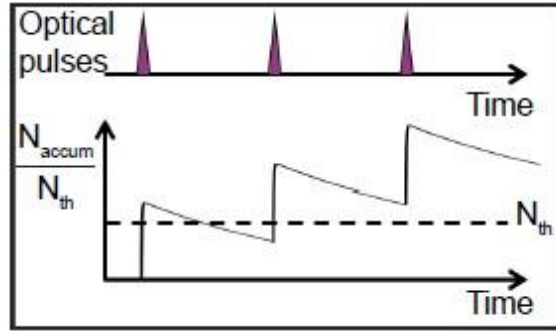

Figure 5-12: Schematic of charge trapping model showing the number of trapped charges normalized by the threshold (N_{accum}/N_{th}) as a function of illumination time. The photoinduced charges are trapped every 1 ms of optical pulses. The trapped charges are thermally de-trapped between the optical pulses. When the number of charge trapping is greater than the loss, the total accumulation increase.

The charge accumulation process is illustrated in Figure 5-12 showing N_{accum} normalized by N_{th} as a function of illumination time. The key description is that there are the charge gain and loss by the trapping and de-trapping processes. We define the gain as N_{trap} as the amount of trapped charges every optical pulse, and the loss as $N_{detrap,i} = exp(-\frac{t_r}{\tau_i(T)})$, where t_r is 1 ms, and τ_i is a thermal de-trap time constant at each i local site. The de-trap time constant is determined by the local trap energy $E_{t,i}$ [28]:

$$\tau_i(T) = \frac{1}{C\, \exp\left(-\frac{E_{t,i}}{k_B T}\right)}$$

Equation 5-5

where C is the rate constant, and T is the temperature. For the simulation results, 21 trap energies ranging from 820 meV to 900 meV were used. The total number of trapped charges at each i local site $N_{accum,i}$ is, therefore, written as a geometric series:

$$N_{accum,i}(t_e, T) = N_{trap} N_{detrap,i} \left[\frac{N_{detrap,i}^{(\frac{t_e}{t_r})+1} - 1}{N_{detrap,i} - 1} \right]$$

Equation 5-6

Here N_{trap} $N_{detrap,i}$ is the first term of the series, $N_{detrap,i}$ is the common ratio, and t_e is the total optical illumination time. Thus, t_e/t_r is the total number of optical pulses exposed to the sample, which is equal to the total number of terms of the series.

The domain intensity from n number of sites can be estimated using a sum of error functions. This fitting imitates the moment of domain transformation, which occurs when $N_{accum,i}$ exceeds N_{th}:

$$I(t_e) = \frac{I_0}{n} \sum_{i=1}^{n} \frac{1 - \text{erf}[N_{accum,i}(t_e, T) - N_{th}]}{2}$$

Equation 5-7

where I_0 is the initial domain intensity.

The charge trapping model provides an estimation of optical intensity dependence of domain transformation. N_{accum} was calculated using the model, and the results of the model for two optilcal intensities of 58 mW cm^{-2} and 145 mW cm^{-2} are shown in Figure 5-13. The N_{accum} normalized by N_{th} is plotted as a function of time after the end of illumination. The black dashed line is for the threshold N_{th} level. In this calculation, a trap energy of 860 meV was only considered. During the illumination, N_{accum}/N_{th} exceeds the unity value at 8 s and 2 s at 58 mW cm^{-2} and 145 mW cm^{-2}, respectively. N_{accum}/N_{th} then increaes up to 2 and 9 before the end of illumination. After the end of illumination, N_{accum}/N_{th} decreases and passes the unity value at 13 s and 37 s for 58 mW cm^{-2} and

145 mW cm^{-2}, respectively. This indicates that the domain transformation occurs faster with higher intensities but the recovery may take longer due to total nuber of trapped charges.
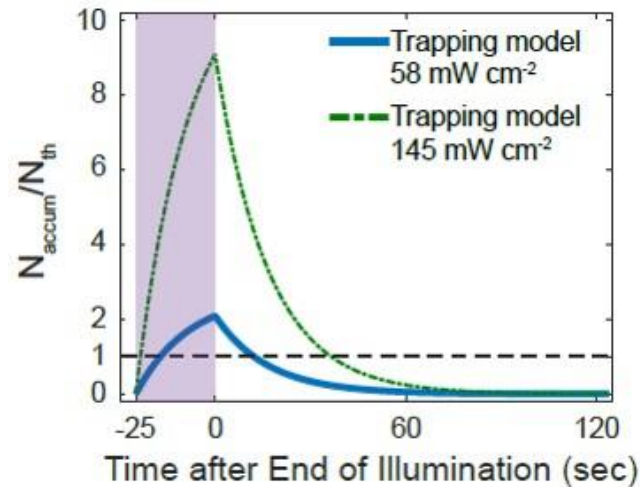

Figure 5-13: Results of optical intensity dependence of domain recovery based on the charge trapping model showing the changes in N_{accum}/N_{th} as a function of time after the end of illumination. The shaded region represents 25 s of optical illumination. Two optical intensity of 58 mW cm^{-2} (solid) and 145 mW cm^{-2} (dash-single dotted) are used.

The charge trapping model also predicts the temperature dependce of domain intensity recovery. The results of simulated domain intensities for two temperatures of room temperature and 335 K are plotted as a function of time after the end of illumination in Figure 5-14. In the model, 21 trap energies within a range of 820 meV to 900 meV are considered. The step-like intensity increase arises from the different trap energy distribution in which the moment of recovery varies by the trap energy. The simulated domain intensity shows that the recovery becomes faster at the higher temperature. The results are compared to the normalized domain recovery intensities measured at room temperature and 335 K extracted from Figure 5-7(b), which shows a good agreement with the model.
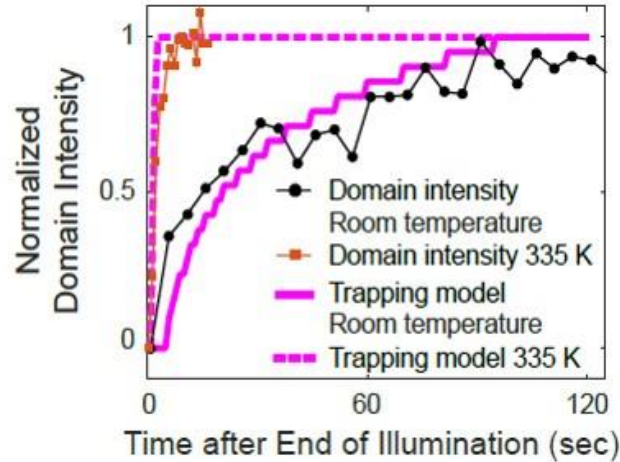
Figure 5-14: Results of temperature dependence of domain recovery based on the charge trapping model showing the changes in domain intensity as a function of time after the end of illumination. Domain intensities are normalized by their initial intensities. Two domain intensities measured at room temperature (circle) and 335(square) are extracted from Figure 7 (b), which are compared to the intensities simulated at room temperature (solid) and 335(dashed).

Based on the results in Figure 5-13, the changes in domain intensity is simulated using the charge trapping model to study the optical intensity dependence of domain transformation. In the simulation, the optical intensities of 46 mW cm^{-2}, 58 mW cm^{-2}, and 145 mW cm^{-2} were considered. Two temperatures of room temperature and 400 K were also considered. The simulated results are plotted as a function of time after the end of illumination in Figure 5-15 by overlapping them with the measured data extracted from Figure 5-5(b). In the simulation, the optically illuminated region consists of 21 trap energies ranging from 820 meV to 900 meV. The first three panels are for room temperature, and the last one is for 400 K in the simulation. The simulation results show that the domain transformation is completed faster at higher optical intensity, and the recovery is not measurable at higher temperature because the recovery is completed much faster than 1 ms. These are in good agreements with the measured data.

As discussed previously, the final N_{accum} depends on the optical intensity and trap energy. By assuming different trap energies are distributed in the illuminated area, N_{accum} can be averaged over this area. The normalized domain intensities for the three intensities measured extracted from

Figure 5-5(b) are plotted as a function of simulated area-averaged N_{accum}/N_{th} in Figure 5-16. In the simulation, 21 trap energies ranging from 820 meV to 900 meV were considered. Figure 5-16 shows that the moments of domain intensity drop for different intensities merge at a certain point of area-averaged N_{accum}/N_{th}. This reflects the validity of the charge trap model calculating the number of trapped charges to estimate the moment of domain transformation and changes in domain intensity.
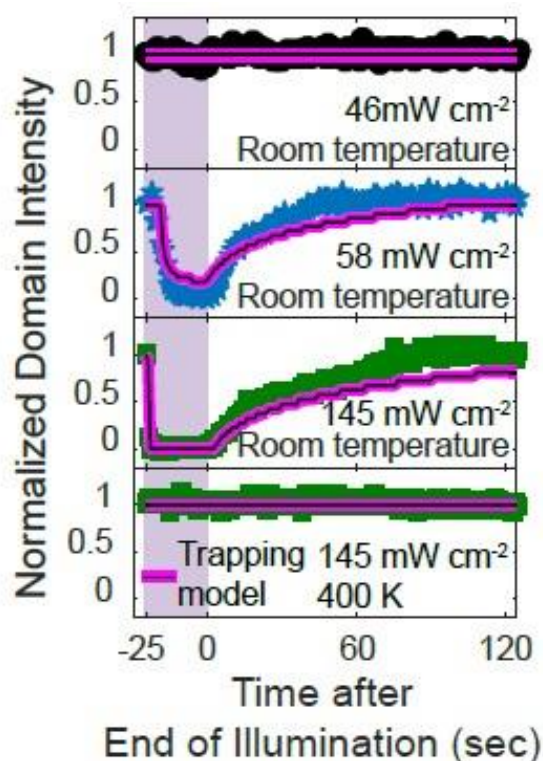

Figure 5-15: Changes in normalized domain intensity as a function of time after the end of illumination compared with the simulated domain intensity from charge trapping model. The shaded region represents 25 s of optical illumination. The measured data is extracted from Figure 5-5 (b).

To investigate the effect of thermally accelerated recovery domain transformation, the change in domain intensity was measured with increasing temperature. The sample was optically illuminated and heated up to 400 K simultaneously during the measurement. The change of normalized domain is shown in Figure 5-17(a). Each data point shows the diffracted x-ray intensity measured for 1 s. The shaded region indicates that the laser is on and the temperature is ramping

up with a ramp-rate of 0.1 K/sec. Within the first few seconds, the domain intensity disappears. It remains at zero-intensity up to 330 K. As the temperature increases further, the domain intensity starts to recover back to the initial intensity. Over 345 K, the recovery domain transformation is thermally accelerated much faster than 1 ms, and the measured intensity stays at the initial intensity.
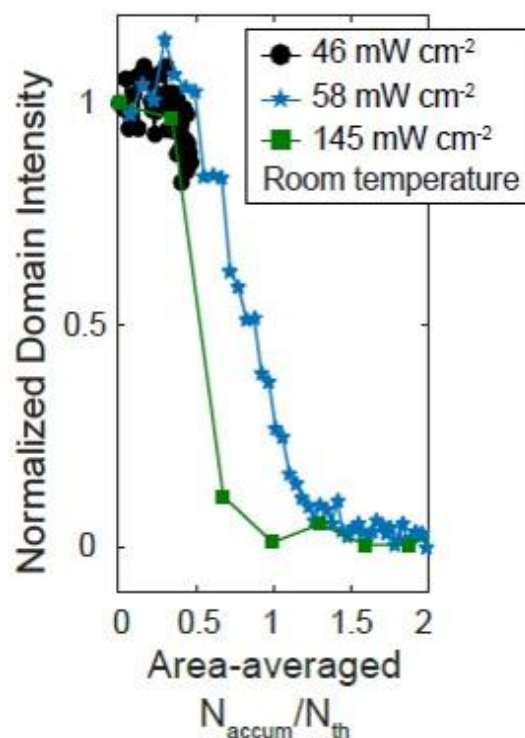

Figure 5-16: Changes in normalized domain intensity as a function of area-averaged N_{accum}/N_{th}. The moments of domain intensity drops using different intensities merge at a certain point.

In Figure 5-17(b), the simulated domain intensity is plotted as a function of increasing temperature. In the simulation, 21 trap energies ranging from 890 meV to 970 meV were considered. The simulated domain intensity decreases to zero within the first few seconds and stays the same until the temperature increases up to 330 K. Above this temperature, the thermal energy becomes high enough to overcome the trap energy and the simulated domain intensity starts to recover back to the initial intensity until the temperature incerases up to 345 K. The step-like

intensity increase arises from the energy variations in which the moment of transformation varies depending on the trap energy. Above this temperature, the simulated domain intensity stays the same which agrees well with the observed results in Figure 5-17(a).
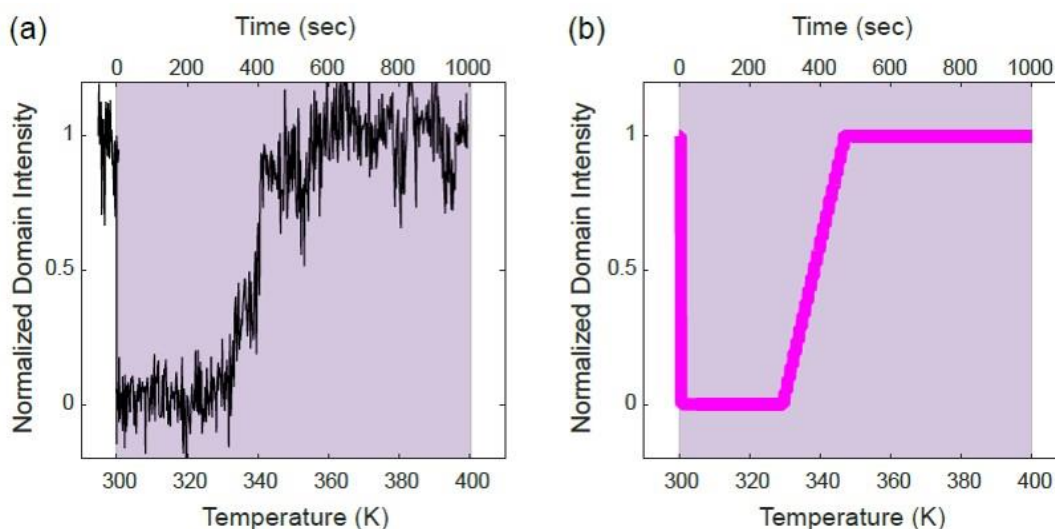

Figure 5-17: (a) Plot of change in normalized domain intensity as a function of temperature with the laser on. The shaded region indicates when the laser is on, and the temperature is ramping up. The temperature ramp rate was 0.1 K/s. (b) Simulated normalized domain intensity as a function of increasing temperature. The Shaded region is where the laser is on, and temperature is ramping up in the simulation.

5.7   Conclusion

In conclusion, we show that the trapped photoinduced charge carriers induce the domain transformation in PTO/STOSLs thin film. The transformation time is accelerated by using higher optical intensity. The slow recovery after the end of illumination at room temperature can also be accelerated at higher temperature faster than a millisecond. The optical intensity and temperature dependence of the domain transformation and recovery are studied by x-ray diffraction experiments. A LGD calculation predicts the domain transformation based on the depolarization field screening effect. A charge trapping model together with the heterogeneous domain transformation model calculates the number of trapped charges. The change in domain intensity during the processes of domain transformation and recovery is simulated. The results are in good

agreements with the measured data. Based on these results, an optimization of optical intensity and the temperature can facilitate the ultrafast reversible optical control of the nanodomains in SLs.

5.8 References

[1]   D. Paez-Margarit, F. Rubio-Marcos, D. A. Ochoa, A. Del Campo, J. F. Fernandez, and J. E. Garcia, ACS Appl. Mater. Interfaces **10**, 21804 (2018).

[2]   F. Rubio-Marcos, D. A. Ochoa, A. Del Campo, M. A. Garcia, G. R. Castro, J. F. Fernandez, and J. E. Garcia, Nat. Photonics **12**, 29 (2018).

[3]   M. M. Yang and M. Alexe, Adv. Mater. **30**, 1704908 (2018).

[4]   H. Akamatsu, Y. Yuan, V. A. Stoica, G. Stone, T. Yang, Z. Hong, S. Lei, Y. Zhu, R. C. Haislmaier, J. W. Freeland, L.-Q. Chen, H. Wen, and V. Gopalan, Phys. Rev. Lett. **120**, 096101 (2018).

[5]   J. Y. Jo, P. Chen, R. J. Sichel, S. J. Callori, J. Sinsheimer, E. M. Dufresne, M. Dawber, and P. G. Evans, Phys. Rev. Lett. **107**, 055501 (2011).

[6]   P. Chen, M. P. Cosgriff, Q. T. Zhang, S. J. Callori, B. W. Adams, E. M. Dufresne, M. Dawber, and P. G. Evans, Phys. Rev. Lett. **110**, 047601 (2013).

[7]   V. A. Stephanovich, I. A. Luk'yanchuk, and M. G. Karkut, Phys. Rev. Lett. **94**, 047601, (2005).

[8]   Y. Ahn, J. Park, A. Pateras, M. B. Rich, Q. Zhang, P. Chen, M. H. Yusuf, H. Wen, M. Dawber, and P. G. Evans, Phys. Rev. Lett. **119**, 057601 (2017).

[9]   S. Piskunov, E. Heifets, R. I. Eglitis, and G. Borstel, Comput. Mater. Sci. **29**, 165 (2004).

[10]   A. Gruverman, B. J. Rodriguez, R. J. Nemanich, and A. I. Kingon, J. Appl. Phys. **92**, 2734 (2002).

[11]   W. L. Warren, D. Dimos, B. A. Tuttle, R. D. Nasby, and G. E. Pike, Appl. Phys. Lett. **65**, 1018 (1994).

[12]   D. Dimos, W. L. Warren, M. B. Sinclair, B. A. Tuttle, and R. W. Schwartz, J. Appl. Phys. **76**, 4305 (1994).

[13]   D. Schick, M. Herzog, H. Wen, P. Chen, C. Adamo, P. Gaal, D. G. Schlom, P. G. Evans, Y. Li, and M. Bargheer, Phys. Rev. Lett. **112**, 097602 (2014).

[14]   H. Wen, P. Chen, M. P. Cosgriff, D. A. Walko, J. H. Lee, C. Adamo, R. D. Schaller, J. F. Ihlefeld, E. M. Dufresne, D. G. Schlom, P. G. Evans, J. W. Freeland, and Y. Li, Phys. Rev. Lett. **110**, 037601 (2013).

[15]   . Li, C. Adamo, P. Chen, P. G. Evans, S. M. Nakhmanson, W. Parker, C. E. Rowland, R. D. Schaller, D. G. Schlom, D. A. Walko, H. Wen, and Q. Zhang, Sci. Rep. **5**, 16650 (2015).

[16]   G. Shirane and S. Hoshino, J. Phys. Soc. Jpn. **6**, 265 (1951).

[17]   A. Bartasyte, B. Dkhil, J. Kreisel, J. Chevreul, O. Chaix-Pluchery, L. Rapenne-Homand, C. Jimenez, A. Abrutis, and F. Weiss, Appl. Phys. Lett. **93**, 242907 (2008).

[18]   J. Qi, N. Ma, X. C. Ma, R. Adelung, and Y. Yang, ACS Appl. Mater. Interfaces **10**, 13712 (2018).

[19]   Y. X. Yang, W. T. Xu, X. J. Xu, Y. J. Wang, G. L. Yuan, Y. P. Wang, and Z. G. Liu, J. Appl. Phys. **119**, 044102 (2016).

[20]   M. B. Okatan, I. B. Misirlioglu, and S. P. Alpay, Phys. Rev. B **82**, 094115 (2010).

[21]   K. G. Lim, K. H. Chew, D. Y. Wang, L. H. Ong, and M. Iwata, EPL **108**, 67011 (2014).

[22]   M. Dawber, C. Lichtensteiger, M. Cantoni, M. Veithen, P. Ghosez, K. Johnston, K. M. Rabe, and J. M. Triscone, Phys. Rev. Lett. **95**, 177601 (2005).

[23]   M. Dawber, N. Stucki, C. Lichtensteiger, S. Gariglio, P. Ghosez, and J. M. Triscone, Adv. Mater. **19**, 4153 (2007).

[24]   T. T. Qi, I. Grinberg, and A. M. Rappe, Phys. Rev. B **82**, 134113 (2010).

[25]   Y. B. Yuan, Z. G. Xiao, B. Yang, and J. S. Huang, J. Mater. Chem. A **2**, 6027 (2014).

[26]   M. R. Morris, S. R. Pendlebury, J. Hong, S. Dunn, and J. R. Durrant, Adv. Mater. **28**, 7123 (2016).

[27]   S. J. Clark and J. Robertson, Appl. Phys. Lett. **94**, 022902 (2009).

[28]   D. K. Schroder, *Semiconductor material and device characterization* (John Wiley & Sons, Inc., Hoboken, New Jersey, 2006), p. 261.

[29]   H. M. Chen and J. Y. M. Lee, Appl. Phys. Lett. **73**, 309 (1998).

[30]   P. Victor and S. B. Krupanidhi, Semicond. Sci. Technol. **20**, 250 (2005).

[31]   J. H. Zhang, C. R. Yang, S. Wu, Y. Liu, M. Zhang, H. W. Chen, W. L. Zhang, and Y. R. Li, Semicond. Sci. Technol. **25**, 035011 (2010).

[32]   L. Pintilie, I. Vrejoiu, D. Hesse, G. LeRhun, and M. Alexe, Phys. Rev. B **75**, 104103 (2007).